



Universität Hamburg
DER FORSCHUNG | DER LEHRE | DER BILDUNG

**The Growth Mechanism of Semiconductor CdSe Nanoplatelets:
Their Connection to Magic-Size Clusters and a Synthesis Pathway
Enabling Future Applications**

Dissertation

an der Universität Hamburg eingereichte Dissertation

Fakultät für Mathematik, Informatik und
Naturwissenschaften – Fachbereich Chemie

vorgelegt von

Julia Irmhild Marie Funk

Hamburg 2024

Erstgutachter: Prof. Dr. Horst Weller

Zweitgutachter: Prof. Dr. Alf Mews

Dissertation

Titel (deutsch):
Eingereicht von: Julia Irmhild Marie Funk
Matrikelnummer: 6608993
E-Mail Adresse: Julia.funk@live.de
Arbeitsgruppe: Prof. Dr. Horst Weller
Institut: Institut für Physikalische Chemie
Universität: Universität Hamburg
Erstgutachter: Prof. Dr. Horst Weller
Zweitgutachter: Prof. Dr. Alf Mews
Prüfungskommission: Prof. Dr. Horst Weller
Prof. Dr. Gabriel Bester
Priv. Doz. Dr. Christoph Wutz
Datum der Disputation: 31.01.2025

Die vorliegende Arbeit wurde in der Zeit von Oktober 2020 bis Dezember 2024
in der Arbeitsgruppe von Prof. Dr. Horst Weller am Institut für Physikalische
Chemie der Universität Hamburg angefertigt.

List of Publications

- Funk, J. I. M.; Sochor, B.; Koyiloth Vayalil, S.; Weller, H. Insights into the Formation of CdSe Nanoplatelets using a Flow Reactor. *Nanoscale* **2024**. DOI: 10.1039/D4NR03804E.

Table of contents

I.	List of abbreviations.....	V
1	Zusammenfassung.....	1
2	Abstract.....	3
3	Introduction.....	5
4	Theoretical principles.....	6
4.1	Semiconductor nanoparticle characteristics.....	6
4.1.1	Properties of semiconductor nanoplatelets.....	11
4.2	Synthesis of semiconductor nanoplatelets.....	14
4.2.1	Growth and nucleation model of semiconductor nanoparticles.....	14
4.2.2	Magic-size clusters.....	22
4.2.3	Flow reactor.....	22
4.2.4	Polymer encapsulation of semiconductor nanoplatelets.....	25
4.3	Characterization of semiconductor nanoplatelets.....	27
4.3.1	Optical spectroscopy.....	27
4.3.1.1	Absorption spectroscopy.....	27
4.3.1.2	Fluorescence spectroscopy.....	27
4.3.2	X-ray scattering.....	32
5	Motivation and Goal.....	34
6	Results and discussion.....	36
6.1	Finding a flow reactor suitable CdSe NPL synthesis.....	36
6.2	Flow reactor synthesis of CdSe NPL.....	44
6.2.1	The correlation between MSCs and NPL.....	48
6.3	Adding a shell to CdSe NPL.....	71
6.3.1	Encapsulation of CdSe NPL in polystyrene – PI-b-PEO shell.....	71
6.3.2	CdSe/CdS core-shell NPL.....	74
7	Outlook.....	76
8	Materials and methods.....	77

8.1	Applied devices and materials	77
8.2	Applied chemicals	79
8.3	Experimental section	80
8.3.1	Synthesis Methods.....	80
8.3.1.1	Synthesis of Se-ODE solution	80
8.3.1.2	Synthesis of CdSe NPL with Cd(OAc) ₂ and without methyl acetate	80
8.3.1.3	Synthesis of CdSe NPL with Cd(OAc) ₂ and with methyl acetate	80
8.3.1.4	Synthesis of CdSe NPL with Cd(OAc) ₂ and with acetic anhydride	81
8.3.1.5	Synthesis of CdSe NPL without Cd(OAc) ₂ and using AcOH	81
8.3.1.6	Reactor precursor synthesis	81
8.3.1.7	Flow reactor setup.....	82
8.3.1.8	Synthesis of CdSe NPL in a flow reactor	83
8.3.1.9	Cleaning of the flow reactor after the CdSe NPL synthesis	84
8.3.1.10	Purification of the raw CdSe NPL product	84
8.3.1.11	Cd(oleate) ₂ -ODE-solution for CdSe/CdS core-shell NPL synthesis	85
8.3.1.12	1-Octanthiol-ODE-solution for CdSe/CdS core-shell NPL synthesis	85
8.3.1.13	CdSe/CdS core-shell NPL synthesis.....	85
8.3.1.14	Purification of the raw CdSe/CdS core-shell NPL product.	85
8.3.1.15	Encapsulation method of CdSe NPL in polystyrene – PI-b-PEO shell	85
8.3.2	Characterization	87
8.3.2.1	<i>In situ</i> absorbance spectroscopy.....	87
8.3.2.2	<i>Ex situ</i> UV/Vis spectroscopy	87
8.3.2.3	Fluorescence lifetime	88
8.3.2.4	TEM.....	89
8.3.2.5	SAXS measurements	89
8.3.2.6	Powder XRD measurements	89
8.3.2.7	Residence time experiments in the flow reactor	90
9	List of references	91

10	Appendix	105
10.1	Safety	105
10.2	SAXS Fit Information.....	109
11	Acknowledgment	116
12	Eidesstattliche Versicherung	118

I. List of abbreviations

AcOH	Acetic acid
AIBN	Azobis(isobutyronitrile)
AO	Atomic Orbitals
BV	Blank value
c-ALD	Colloidal atomic layer deposition
Cd(OAc) ₂	Cadmium acetate
Cd(myristate) ₂	Cadmium tetradecanoate, also called cadmium myristate
CdO	Cadmium oxide
CdSe	Cadmium selenide
CdS	Cadmium sulfide
CdTe	Cadmium teluride
CSTR	Continuous flow stirred tank reactor
DOS	Density of states
DVB	Divinylbenzene
EtOH	Ethanol
FLT	Fluorescence lifetime
FRET	Förster resonance energy transfer
FWHM	Full width at half maximum
h	Hour
HOMO	Highest occupied molecular orbital
LCAO	Linear combination of atomic orbitals
LED	Light-emitting diodes
LUMO	Lowest unoccupied molecular orbital
MeOH	Methanol

min	Minute/ minutes
ML	Monolayer
MO	Molecular orbital
MSCs	Magic-size clusters
MWCO	Molecular weight cut-off
NPLs	Nanoplatelets
OA	Oleic acid
ODE	1-Octadecene
PEEK	Polyether ether ketone
PEG	Poly(ethylene glycol)
PEO	Poly(ethylene oxide)
PI-b-PEO	Polyisoprene-block-poly(ethylene oxide) diblock-copolymer
PLE	Photoluminescence excitation
QDs	Quantum dots
QLED	Quantum dots light-emitting diodes
QY	Quantum yield
RT	Room temperature
SAED	Selected area for electron diffraction
SAXS	Small angle X-ray scattering
Se	Selenium
sec	Second/ seconds
TEM	Transmission electron microscopy
TOP	Trioctylphosphine
UV/Vis	Ultraviolet/ visible
VA-044	2,2'-Azobis[2-(2-imidazoline-2-yl)propane] dihydrochloride

XRD X-ray diffraction

ZB Zinc blende

1 Zusammenfassung

Die CdSe Halbleiter-Nanoplättchen besitzen außergewöhnliche optische Eigenschaften. Aus der Nanoplättchendicke resultiert eine starke Einschränkung des Exzitons, sodass schmale Absorptionsmaxima von einem leichten und einem schweren Loch, sowie eine ebenso schmale Emission entstehen. Infolgedessen sind CdSe Nanoplättchen für bestimmte Anwendungen, wie beispielsweise LED-Bildschirme, geeigneter mit diesen optischen Eigenschaften. Um die sphärischen CdSe Quantenpunkte zu ersetzen, bedarf es einer CdSe-Nanoplättchen-Synthese, die für große Produktionsmengen auf industrielles Niveau skaliert werden kann. Denn aktuell gibt es keinen Syntheseansatz für CdSe Nanoplättchen in Flussreaktoren. Für die Produktion und Anwendung von CdSe Nanoplättchen ist ein tiefgreifendes Verständnis über ihren Wachstumsmechanismus essentiell. Darüber hinaus sind Modifikationen der Nanoplättchen teilweise notwendig, um bestimmte Anwendungen zu ermöglichen.

In dieser Arbeit wurde eine Flussreaktorsynthese von CdSe Nanoplättchen entwickelt. Hierbei entstehen hauptsächlich 3 Monolagen dicke CdSe Nanoplättchen. Diese besitzen schmale Absorptionsmaxima von 435 nm und 462 nm mit einer Halbwertsbreite von 13 nm für das leichte Loch und 9 nm für die Absorption des schweren Lochs. Die Emission der 3 Monolagen CdSe Nanoplättchen bei 463 nm besitzt eine genauso schmale Halbwertsbreite von 8 nm. Neben 3 Monolagen CdSe Nanoplättchen entstehen auch 4 Monolagen CdSe Nanoplättchen. Hierbei entstehen Absorptionsmaxima bei 481 nm und 513 nm, sowie eine entsprechende Emission bei 514 nm. Als Resultat dieser Synthese, bei denen der Cadmium-Vorläufer und Selen-Vorläufer nicht getrennt werden, besitzen diese Flussreaktor-Nanoplättchen große und nicht-uniforme laterale Flächen von ungefähr 1000 nm^2 . Entsprechend liegen ihre Fluoreszenzquantenausbeuten bei unter 1 Prozent. Darüber hinaus konnte eine Nukleationstemperatur von $180 \text{ }^\circ\text{C}$ festgestellt werden für die CdSe Nanoplättchen im laminaren Strömungsprofil des Flussreaktors.

Wiederum konnten dank der vereinten Vorläufer-Lösungen die frühesten Stadien der CdSe-Nanoplättchensynthese hergestellt und mittels UV/Vis-Spektroskopie, Transmissionselektronenmikroskopie und Kleinwinkelröntgenstreuung untersucht werden. Dabei wurden CdSe-360 und CdSe-405 Magic-Size Cluster beobachtet, die wichtige Bausteine bei der Synthese von CdSe Nanoplättchen darstellen. Diese Magic-Size Cluster agglomerieren und durchlaufen einen Größenfokussierungsprozess, um Intermediatstrukturen zu bilden. Insbesondere durch die Blauverschiebungen in den Anregungsspektren und durch Größenfokussierungen in den Kleinwinkelstreuungsmustern konnten diese Intermediate festgestellt werden. Anhand dieser

Ergebnisse wurde ein Wachstumsmodell entwickelt, welches zeigt, wie die CdSe Magic-Size Cluster mit ihrem großen Durchmesser dank des Intermediates zu den schmalen CdSe Nanoplättchen heranwachsen. Mit Hilfe der Röntgendiffraktometrie wurde für die CdSe Nanoplättchen eine Zinkblende-Struktur bestimmt. Für genau diese Zinkblende-CdSe-Nanoplättchen ist der Wachstumsmechanismus noch nicht vollständig aufgeklärt. Somit liefern die vorliegenden Ergebnisse wichtige und neue Informationen, um das Wachstum der CdSe-Nanoplättchen in Zukunft vollständig zu verstehen.

Mit einer CdS-Schale oder einer Polystyrol-PI-b-PEO Hülle konnten die CdSe Nanoplättchen erfolgreich modifiziert werden. Die Polystyrol-Hülle erlaubt den CdSe Nanoplättchen in wässrigen Medien stabil vorzuliegen. Wiederum erlaubt die CdS-Schale die optischen Eigenschaften der CdSe Nanoplättchen anzupassen. Dank der Flussreaktorsynthese und diesen Modifizierungen ist ein Fundament geschaffen, um CdSe Nanoplättchen in Zukunft in diversen Anwendungen einsetzen zu können.

2 Abstract

Anisotropic semiconductor nanoplatelets possess exceptional optical properties. They result from the strong confinement of the exciton through the thickness of the nanoplatelets so that narrow light-hole and heavy-hole absorption peaks, as well as narrow emission peaks, emerge. Due to their optical properties, CdSe nanoplatelets would be more suitable candidates for applications like LED screens to replace spherical quantum dots in the long term. However, it is relevant here that the synthesis of CdSe nanoplatelets can be scaled to produce large quantities on an industrial level. Currently there is no known synthesis method for CdSe nanoplatelets in a flow reactor. Ideally, further insights into the growth mechanism of the CdSe nanoplatelets should also be found, and additional modifications should be made to these nanoplatelets, depending on the application.

In this work, a synthesis of CdSe nanoplatelets was developed for a flow reactor. With this combined precursor method, mainly 3 monolayer thick CdSe nanoplatelets resulted with their typical absorption peaks at 435 nm and 462 nm and a narrow full width at half maximum of 13 nm for the light-hole and 9 nm for the heavy-hole. The emission of the 3 monolayer CdSe nanoplatelets at 463 nm is also narrow, with a full width at a maximum of 8 nm. In addition to 3 monolayer CdSe nanoplatelets, 4 monolayer CdSe nanoplatelets are also synthesized with absorption peaks at 481 nm and 513 nm, including the respective emission at 514 nm. As a result of combining the cadmium precursor and selenium precursor, these CdSe nanoplatelets produced from the flow reactor have large and non-uniform lateral areas of approximately 1000 nm². Accordingly, their quantum yield is below 1 percent. In the laminar flow profile of the flow reactor, the nucleation temperature of the CdSe nanoplatelets was determined to be at 180 °C.

Thanks to the combined precursor solutions, the earliest synthesis stages of the CdSe nanoplatelets could be reached and analyzed using UV/Vis spectroscopy, transmission electron microscopy, and small-angle X-ray scattering. CdSe-360 and CdSe-405 magic-size clusters were observed and, thus, were discovered as important building blocks in the CdSe nanoplatelet synthesis as part of this work. These magic-size clusters agglomerate and undergo a size-focusing process in order to form intermediate structures. In particular, these intermediates were detected by the blue shift in the photoluminescence excitation spectra and the size focussing visible in the small-angle X-ray patterns. Based on these results, a growth model was developed that shows how the magic-size clusters can grow through the intermediate stage to the CdSe nanoplatelets. Based on the X-ray diffraction, the CdSe nanoplatelets have a zinc blende structure.

The mechanism for precisely these zinc blende CdSe nanoplatelets is not yet fully understood. Therefore, the obtained results provide important and new information to fully understand the growth mechanism of CdSe nanoplatelets in the future.

The CdSe nanoplatelets were successfully modified with a CdS-shell or a polystyrene-PI-b-PEO shell. A water-stability could be obtained with the addition of the polystyrene-encapsulation. The CdS-shell allowed to change the optical properties of the CdSe nanoplatelets. Thanks to the flow reactor synthesis and the modifications, a foundation has been created to use the CdSe nanoplatelets for various applications in the future.

3 Introduction

Nowadays, we cannot imagine daily life without nanoparticles. The prefix “nano” from the word “nanoparticle” originates from the Greek language. It translates to “dwarf” and describes a fraction of a billionth.^{1,2} One significant aspect of nanoparticles are their unique properties compared to their bulk-material counterparts, which are induced by a phenomenon called *quantum confinement*.³ Nanoparticles have a much higher surface-to-volume ratio and can have various shapes. Some of these shapes are not just spherical but, for example, rod shaped or nanoplatelets. Their material can also vary between organic and inorganic materials, thus enabling various applications.¹ Furthermore, nanoparticles are already being utilized in fields like microelectronics or the biomedical field.² One example from the microelectronics field is found in some of our living rooms with quantum dots light-emitting diodes (QLED) screens for our televisions.⁴ Another example can be found during the COVID-19 pandemic when people worldwide relied on the SARS-CoV rapid tests to check for an infection. In these rapid tests, gold nanoparticles, together with proteins, are used as antibody labels for the SARS-CoV virus.⁵

These two examples showcase how close and essential nanoparticles are in our daily lives. To keep using more and new nanoparticles for new and different applications, they need to be accessed in large quantities. This access is also bound to two essential requirements. The first requirement is to understand the growth mechanism and its fundamental principles.⁶ This knowledge is necessary to precisely control the nanoparticle's shape and size. The second requirement is a controllable, low-cost synthesis scaled to industrial levels.⁷ Some of these synthesis approaches include the usage of batch and flow reactors.^{7,8}

Mass production is established for spherical semiconductor quantum dots, and their synthesis pathways have been researched for years.⁶ However, mass production is rarely established for anisotropic semiconductor nanoparticles. Exemplary anisotropic nanoparticles are the semiconducting cadmium selenide (CdSe) nanoplatelets (NPLs). In their case, the growth mechanism still needs to be fully understood and discussed.^{9–11} Knowledge about the growth mechanism is crucial to developing a reliable scale-up synthesis method for future applications of these anisotropic semiconductor nanoparticles.

In this work, possible answers are provided to the challenge of mass-producing anisotropic semiconductor CdSe NPLs. This work presents new information on their growth mechanism and showcases a pathway for accessing CdSe NPLs through a scale-up synthesis technique. Furthermore, two techniques are presented for modifying these CdSe NPLs to enable new future applications.

4 Theoretical principles

4.1 Semiconductor nanoparticle characteristics

A distinction between metals, semiconductors, and insulators is typically made based on their electrical conductivity. The metal's electrical conductivity decreases with increasing temperature, while the opposite applies to semiconductors. Insulators, as the name suggests, do not show electrical conductivity at all. Understanding how electrons move within these systems is important to further explain this behavior and outline the difference between bulk materials and nanoparticles.¹²

Fundamental quantum mechanics describe electrons with a wave-particle duality. As a result of this description, atomic orbitals are used to describe the probability of an electron located in an atom as a wave function.¹² To describe nanoparticles and their bulk material counterparts, multiple atoms are needed. One way to describe the electron wavefunction in a system with multiple atoms is through the linear combination of atomic orbitals, also known as LCAO-method. This method allows for an approximation of the electron wavefunction through combination of atomic orbitals to molecular orbitals. For example, consider two atomic orbitals, which would be the case for a hydrogen molecule. The combination of these two 1s atomic orbitals lead to the formation of one bonding and one anti-bonding molecular orbital. The bonding molecular orbital, called σ molecular orbital, has a lower energy than the individual atomic orbitals. As a result, this molecular orbital is occupied with the two electrons arising from the previous two atomic orbitals to minimize the potential energy of this molecule. This highest occupied molecular orbital is also called HOMO. The anti-bonding molecular orbital, called σ^* molecular orbital in this case, has a higher energy compared to the atomic orbitals. This molecular orbital remains unoccupied and is also referred to as the lowest unoccupied molecular orbital, short LUMO. Based on this example, it is also possible to combine multiple atomic orbitals to obtain multiple molecular orbitals. Through this combination, most molecular orbitals have an intermediate energy value instead of very high or very low energy values.^{12,13} Consequently, many MOs are being formed, creating a quasi-continuum and an energy band. The upper, unoccupied energy band is referred to as the conduction band, and the lower occupied energy band is called the valence band. Figure 1 shows a schematic representation of the LCAO method.^{12,13}

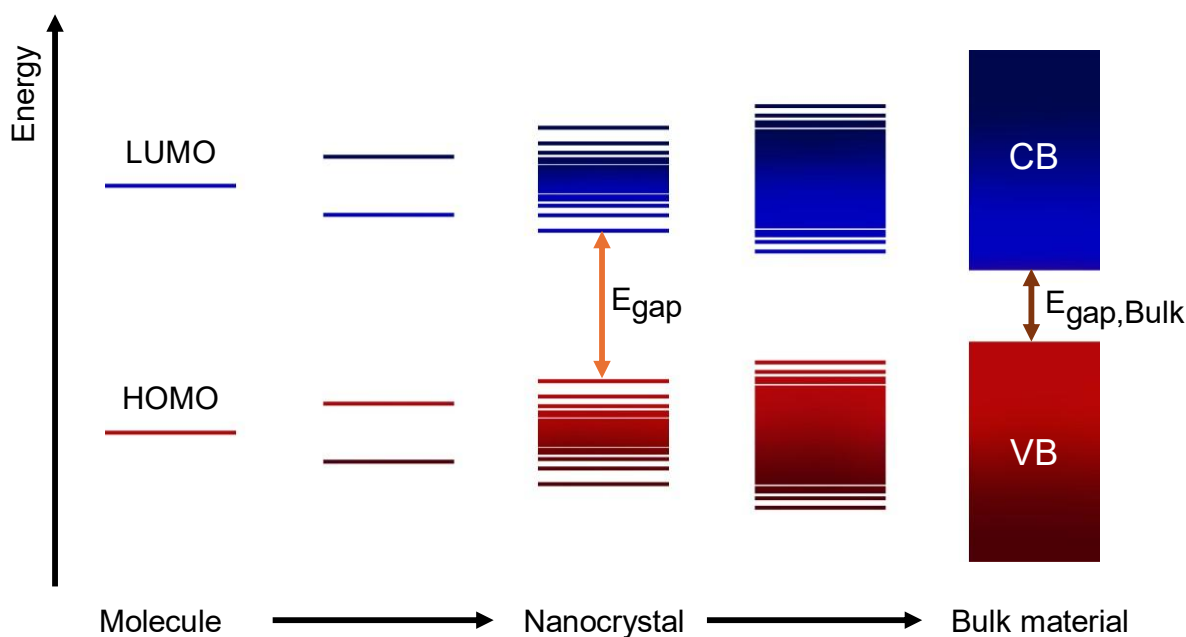


Figure 1: Schematic presentation of the LCAO method based on a semiconductor material. The more MOs are formed through the combination of AOs, the smaller the band gap becomes. Through thousands of MOs, a quasi-continuum is obtained in the form of a valence and a conduction band. The image shows that the band gap of a nanocrystal E_{gap} is larger compared to the bulk material $E_{\text{gap,Bulk}}$. The image is recreated from the literature.^{12,13}

Based on the LCAO method shown in Figure 1, the band gap size difference between the nanocrystals and their bulk material counterpart becomes apparent. The more MOs are being formed, the more near-band-edge level MOs are being produced. Therefore, smaller nanocrystals have a larger band gap than bigger nanocrystals.^{12,13} This observation is referred to as the quantum size effect.¹⁴

Semiconductors have an occupied valence band and an unoccupied conduction band. Between these energy bands lies the band gap. For an electron to move up to the conduction band, it must gain energy equal to or higher than the band gap. This energy gain can come, for example, in the form of absorbing a photon. With this energy, an electron can move to the conduction band. During this process, a quasi-particle called a *hole* is formed in the valence band. Compared to the negatively charged electron, the hole has a positive charge. Both the electron and hole are charge carriers. This bound pair together as a quasi-particle is called an *exciton*. As both charge carriers move within a crystal lattice, they are described through an effective mass. Taking their opposite charges into account, both the electron and hole interact with each other through Coulomb interactions. Thus, the minimum energy to create an exciton requires the energy of

the band gap E_{gap} and the kinetic energies of the electron $E_{\text{kin,e}}$ and the hole $E_{\text{kin,h}}$, subtracted by the Coulomb energy E_{coulomb} . This exciton energy E_{exc} can be described in Equation 1:^{12,13}

$$E_{\text{exc}} = E_{\text{gap}} + E_{\text{kin,e}} + E_{\text{kin,h}} - E_{\text{coulomb}} \quad (1)$$

With the interaction between the charge carriers, the exciton itself also occupies a radial space.^{13,15} This radial space of the exciton can be described through the exciton Bohr radius a_0 in Equation 2

$$a_0 = \frac{4\pi \hbar^2 \epsilon_d}{e^2} \left(\frac{1}{m_e^*} + \frac{1}{m_h^*} \right) \quad (2)$$

where \hbar is the reduced Planck constant, ϵ_d is the semiconductor dielectric constant at optical frequencies, e is the electron charge, and finally, m_e^* and m_h^* the effective masses of the electron and hole, respectively.^{13,15,16} One more difference is demonstrated between nanomaterials and bulk materials with the exciton: The exciton Bohr radius has less space in a nanocrystal than in the bulk material; thus, nanomaterials are in the quantum confinement regime.^{13,15} Quantum confinement can be further differed between strong and weak confinement. If the nanocrystal is smaller than the exciton Bohr radius, then there is a stronger confinement, and the kinetic energy between the charge carriers is larger than their Coulomb interaction. The charge carriers can be treated independently. However, the resulting confinement is weak if the nanocrystal is larger than the exciton Bohr radius. Comparing both confinements, the difference in the energy levels and, therefore, in the band gap is much bigger in the strong confinement than in the weak confinement.¹³

The shape of the nanocrystals strongly impacts the confinement of the exciton, as well. In spherical nanocrystals, often called quantum dots, the exciton is confined in all three dimensions. These particles with fully confined excitons are called 0-D nanomaterials. For 1-D nanomaterials, the exciton is only confined to two dimensions. These 1-D nanomaterials are, for example, nanowires or nanorods, meaning a delocalization of the charge carriers is still possible in one dimension. Nanoplatelets and nanowells are 2-D nanomaterials in which the excitons are confined in only one dimension, the thickness of the material. For bulk 3-D materials larger than the exciton Bohr radius, a delocalization of the charge carriers in all three dimensions is possible.^{13,17} The density of states (DOS), which describes the amount of electrons within an energy range, also depends on the dimensions of the nanomaterials.¹⁷ In Figure 2, the nanomaterial shape's effect on the density of states is portrayed.^{13,17}

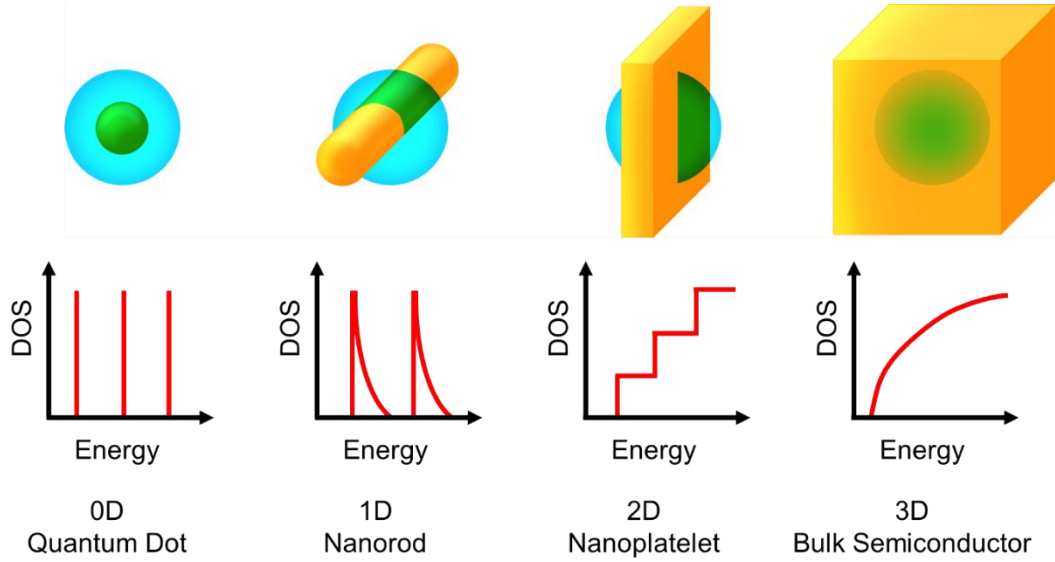


Figure 2: Schematic representation of the density of states (DOS) depending on the dimensionality of the nanomaterials. The exciton Bohr radius is depicted in blue, showing the confinement within the yellow semiconductor nanomaterials. The image is recreated from the literature.^{13,17}

Taking the Coloumb interaction of the charge carriers into account, the band gap energy of a spherical nanoparticle $E_{\text{gap,nano}}$ can be described as

$$E_{\text{gap,nano}} = E_{\text{gap}} + \frac{\hbar^2 \pi^2}{2r^2} \left(\frac{1}{m_e^*} + \frac{1}{m_h^*} \right) + E_{e,h} + E_e^{\text{pol}} + E_h^{\text{pol}} - 0.248 E_{\text{Ry}} \quad (3)$$

in Equation 3.¹³ In this Equation, r is the nanocrystal radius, $E_{e,h}$ is the Coulomb interaction between the electron and the hole and E_e^{pol} E_h^{pol} are the self-polarization energies of the electron and hole. The last term contains the Rydberg energy E_{Ry} . Here, the effective Coulomb interaction can be also described in the following Equation 4:¹³

$$E_{e,h} = \frac{-1.786 e^2}{\epsilon_{\text{QD}} r} \quad (4)$$

In this Equation, the dielectric constant of the spherical nanocrystal ϵ_{QD} is present.¹³ As a simple approach, both Equations allow a description of the confinement in semiconductor quantum dots.^{13,18} However, neither Equation is sufficient to describe the strong confinement in one direction and weak confinement in the lateral direction of the exciton within the CdSe NPLs.¹⁸ One problem is that the confinement energy is not properly described by these Equations when the nanocrystals are very small.¹⁸⁻²⁰ Another problem is the splitting of the valence band into subbands in semiconductor materials, like CdSe, which are not considered in the simple effective mass approximation.^{19,20} Consequently, other methods based on the Schrödinger Equation are used to describe the band gap in CdSe NPLs.^{19,20}

As discussed above, semiconductors have a valence band, a conduction band, and, in between these energy bands, a band gap. Electrons can overcome the band gap through the absorption of energy. Thermal energy is sufficient enough to excite the electrons, and that conduction occurs in the bulk material. In contrast, metallic conductors also have a valence band and a partially occupied conduction band with no band gap in between. Hence, in metals, the electrons can easily move through the conduction band. Higher temperatures decrease the conductivity of metals because the electrons collide more often with the atom's crystal lattice. Insulators often have a band gap so large that electrons can not cross the band gap to reach the conduction band.^{12,17}

Semiconductor nanoparticles of any shape can also consist of more than one material. These heteronanostructures impact the delocalization of the charge carriers because as shown in Equation 4, the band gap, and thus the energy offset between the HOMO and the LUMO, depends on the material of the nanocrystal. Consequently, two materials create two band gaps within one nanocrystal if one of these two materials “coats” the other, creating a core/shell structure. Taking a core/shell quantum dot as an example, the energy offset between HOMO and LUMO can be differed into three types. Type-I quantum dots can have a core material with a narrower band gap compared to its shell material. Here, once an exciton forms, it is mainly confined in the core material. However, the opposite case can also be true if the band gap is narrower for the shell material, because then the exciton would be located in the shell. This exciton is also called direct exciton. Type-II quantum dots, the conduction band, and the valence band of the shell material are staggered compared to the ones from the core material. As a result, the exciton will be spatially separated; an indirect exciton will form. Because of the energy levels, the hole will remain in the core material, and electrons will remain in the shell materials. In the case of a very small offset between the conduction bands of the core and shell material compared to a big offset between their valence bands, these quantum dots are referred to as quasi-type-II quantum dots. However, these quasi-type II quantum dots are, per definition, still Type-I quantum dots. In these quasi-type II quantum dots, the electron can delocalize across the core and shell while the hole remains confined in the core. The delocalization of the charge carriers in the different types of heteronanocrystals is presented in Figure 3.^{13,21}

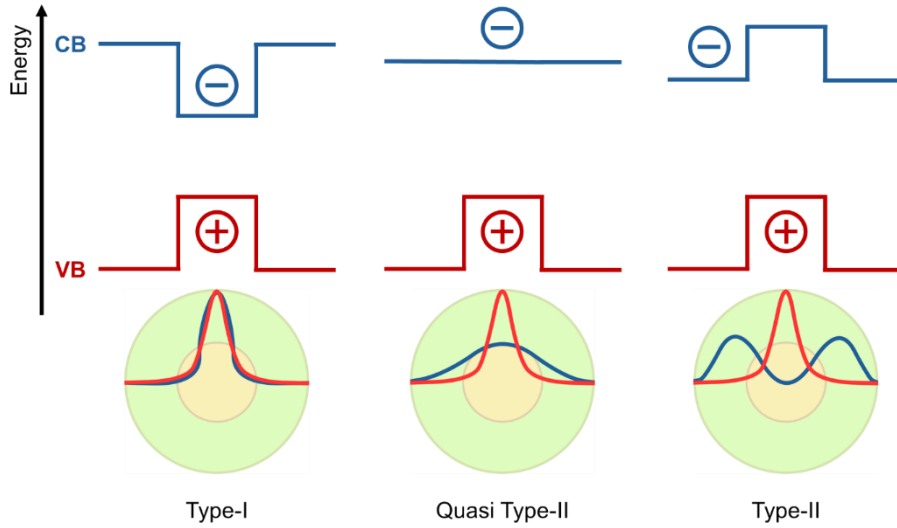


Figure 3: A schematic image of a type-I, quasi-type-II, and type-II nanocrystal. The wavefunctions of the charge carriers are depicted in blue for the conduction band and in red for the valence band. Here, the nanocrystal core is depicted in a pale-yellow color, and the shell material is pale-green. The image is recreated from the literature.^{13,21}

4.1.1 Properties of semiconductor nanoplatelets.

One interesting aspect of CdSe nanoplatelets is in their absorption spectrum because two peaks are visible, one for the electron and light-hole transition and another one for the electron and heavy-hole transition of the exciton.²² To further explain this observation, it is important to understand the electron movement within a crystal lattice. In the dispersion relation, an electron in a vacuum can be described as a plane wave with a continuum of energy levels (Figure 4, left). In a nanocrystal, the electron wavefunction with a value \mathbf{k} experiences a periodic potential a_c through the crystal lattice atoms. Taking this lattice constant into account, a Bloch function can be used to describe the movement of the electron in the CdSe crystal lattice. The electrons are now either slightly disturbed by the crystal lattice or are completely reflected by the lattice. This Bragg reflection creates two standing waves at the wave vectors $\mathbf{k} = \pi \cdot \mathbf{a}_c^{-1}$ and $\mathbf{k} = -\pi \cdot \mathbf{a}_c^{-1}$. Thus, both standing waves at the same electron wavefunction value k have different charge distributions and create an energy gap (Figure 4, middle). The periodic lattice means for the Bloch function that the values \mathbf{k} and $\mathbf{k} + 2\pi \cdot \mathbf{a}_c^{-1}$ have the exact same impact. Hence, the energy regime of the dispersion relationship can be restricted into an interval of $-\pi \cdot \mathbf{a}_c^{-1}$ up to $\pi \cdot \mathbf{a}_c^{-1}$, which is called the Brillouin zone (Figure 4, right). The dispersion relation for the electron in the different environments is shown in Figure 4.¹³

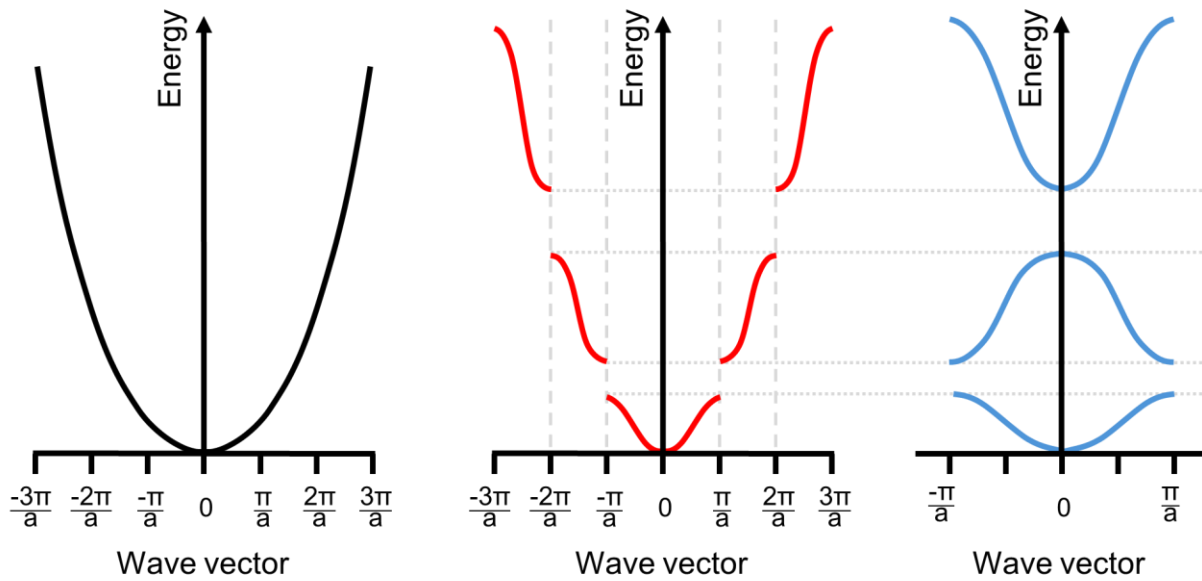


Figure 4: The dispersion relation of an electron in a vacuum (black, left), in a one-dimensional crystal (red, middle), and a restricted representation in a one-dimensional crystal (blue, right). The image is recreated from the literature.¹³

In Chapter 4.1, the band model was used to explain the formation of the valence band and conduction band. These bands can also be assumed to have a parabolic form, similar to the dispersion relation, as shown in Figure 5.²³ For semiconductor CdSe with a wurtzite or zinc blende structure, the conduction band is formed by 5s-orbitals of the cadmium. However, the 4p-orbitals of the selenium are now the foundation of the valence band. These orbitals are not only sixfold degenerated but split the valence band into a light-hole subband, a heavy-hole subband, and a split-off hole subband because of a strong split-orbit-coupling and the different angular moments. The splitting also depends on the crystal structure of the semiconductor. Wurtzite semiconductors have at every electron wavefunction value \mathbf{k} the splitting of the subbands. Diamond-like semiconductors only split into light-hole and heavy-hole subbands at values that are not $\mathbf{k} = 0$.²³ The difference in the curvature also indicates the different effective masses of the holes.²⁴

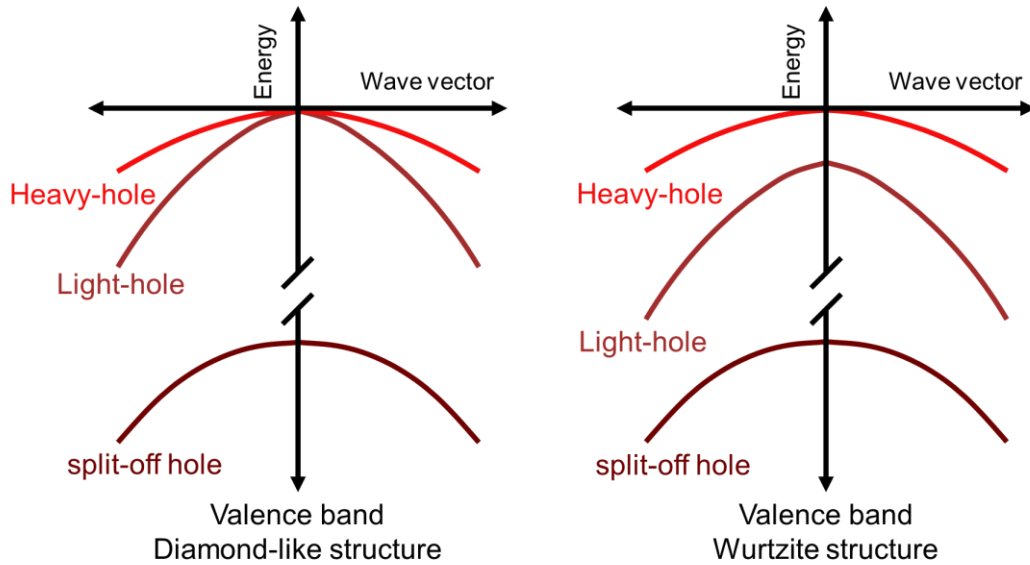


Figure 5: Valence band structure for a diamond-like and a wurtzite semiconductor. In both cases, the valence band shows a split-off band (brown). Depending on the crystal structure, at $k = 0$, there is another subband split visible into a heavy-hole (red) and a light-hole (dark red) band. This subband is not visible at $k = 0$ for a diamond-like structure but at other wave vector values. The image is recreated from the literature.²³

In nanoplatelets, the confinement through the thickness is so strong that the heavy-hole and light-hole subband drift further apart in energy at $\mathbf{k} = 0$.²⁵ The exciton Bohr radius of CdSe bulk material is 5.4 nm,²⁶ which also supports the strong confinement of CdSe NPLs because the thickness for three monolayers is known to be 0.9 nm.²⁷ As a consequence, both transitions are visible in the absorption spectra. Another interesting aspect of nanoplatelets is a minimal Stokes shift between the emission and the electron/heavy-hole transition peak in the absorption.²⁸ Furthermore, all peaks in the absorption and emission are very narrow, and the lateral size of the nanoplatelets barely affects these optical properties.²² The very high exciton-binding energy also shortens the fluorescence decay of CdSe NPL.²⁸ Furthermore, thin NPLs usually have a lower fluorescence quantum yield than thicker NPLs.²⁹ The quantum yield also strongly depends on the lateral size of the NPLs because laterally smaller NPLs have a higher quantum yield compared to laterally larger NPLs.³⁰

Like nanodots, NPLs can be modified through shell growth into a heteronanostructure. The shell growth method for NPLs can be performed through a high-temperature growth method by Riedinger et al. which leads to very thick cadmium sulfide (CdS) shells around the CdSe NPL core.³¹ Through this method, bright nanoplatelets with a high quantum yield are obtained, and the emission remains narrow.³¹ A different approach for shelling NPLs is the colloidal atomic layer deposition (c-ALD) method by Kovalenko et al.³² This room-temperature method allows

the growth of a shell layer-by-layer onto the CdSe NPL. However, this lower crystallinity in the shell from the room-temperature approach causes a lower quantum yield.³² In both cases, the CdS-shell leads to a quasi-type II CdSe/CdS NPL.^{13,21,32,33} Thus, the electron can delocalize into the NPL's shell and core structure, and a red shift in the optical properties is visible.^{31,32} In Figure 6, a schematic drawing of a core-shell NPL is shown.³²

Aside from shells, a so-called crown structure can be grown onto NPLs. The crown-structure refers to the lateral growth of the CdSe NPL with CdS, which is a unique growth method for anisotropic nanoplatelets. Analogous to the shell growth, the passivation of the CdSe NPLs sides through the lateral growth with CdS leads to improved quantum yields.³⁴ Figure 6 also shows a schematic drawing of a core-crown NPL.³⁴



Figure 6: A core-shell NPL (left) and a core-crown NPL (right), where the core material is depicted in yellow and the shell/crown in orange. The left image is recreated from literature,³² and the right image is also recreated from literature.³⁴

4.2 Synthesis of semiconductor nanoplatelets

4.2.1 Growth and nucleation model of semiconductor nanoparticles.

The synthesis of nanoparticles, in general, involves two essential steps: Nucleation and growth.^{6,13}

Nucleation involves the formation of nuclei, which act as the base for the crystal growth.⁶ This process can be further divided into two nucleation types. Homogeneous nucleation involves the formation of a nucleus within one uniform medium. The second nucleation type, heterogeneous nucleation, describes the formation of nuclei on different structural surfaces.^{6,13} In both cases, monomers are needed, which can then assemble into nuclei. The monomer concentration can change drastically by either injecting a precursor, changing the temperature, or a sudden change in solubility of one of the precursor components.¹³ To form a nucleus, a certain amount of free energy is required. This is best described in the Gibbs free energy ΔG_{total} in Equation 5.^{6,13}

$$\Delta G_{\text{total}} = 4\pi r^2 \gamma + \frac{4}{3} \pi r^3 \Delta G_v = \Delta G_s + \frac{4}{3} \pi r^3 \Delta G_v \quad (5)$$

In this Equation 5, r denotes the nanoparticle radius again. There is also the surface energy γ and the free energy of the bulk crystal ΔG_v . In this Equation, the first term can also be replaced with the free energy of the surface ΔG_s . The crystal-free energy can be further described in Equation 6: ^{6,13}

$$\Delta G_v = \frac{-k_B T \ln(S)}{v} \quad (6)$$

It becomes apparent that the crystal free energy in Equation 6 depends on the Boltzmann constant k_B , the temperature T , the supersaturation of the solution S , and volume of the atom within the molecule v .^{6,13} The surface energy described in the first term of Equation 5 always has a positive value because the bonds of the monomers at the surface are not saturated. The crystal-free energy in the second term, also referred to as volume-free energy, is negative because energy is needed to form chemical bonds in nuclei. Based on these free energies, a critical radius results so that the nuclei remain stable in the solution. Nuclei smaller than the critical radius redissolve and form monomers, while nuclei bigger than the critical radius grow into mature nanoparticles.¹³ The effect on the free energies and the critical radius can be visualized in the plot

Figure 7.^{6,13}

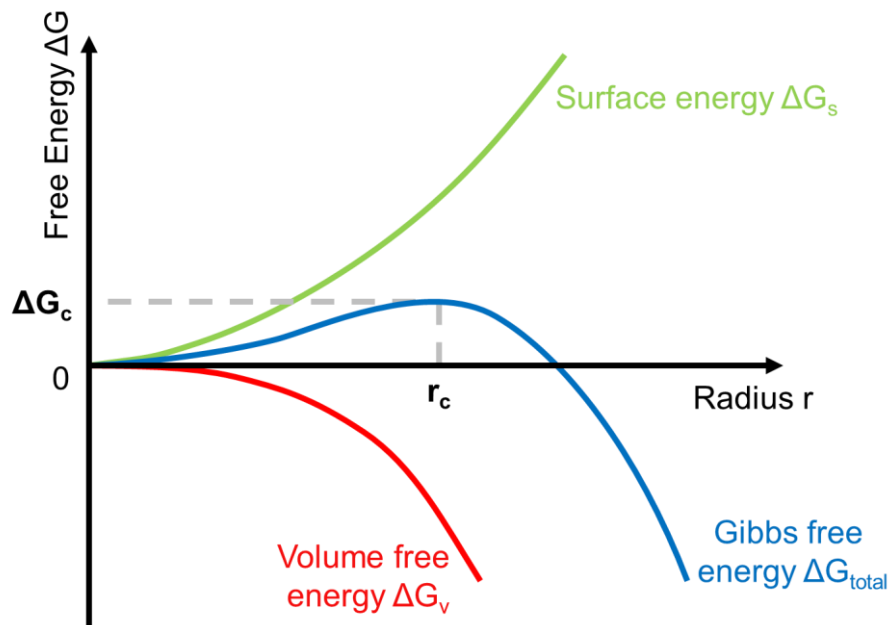


Figure 7: A Plot to showcase the change in free energy depending on the radius of a spherical nanocrystal nucleus (blue). The positive surface energy is marked in green, and the negative volume free energy is marked in red. At a critical radius r_c , the required activation nucleation barrier for nucleation is indicated at ΔG_c . The image is recreated from the literature.¹³

After nucleation, the next step is growth. The growth of nanoparticles depends especially on their surface reactions and the monomer diffusion. An increase in growth rate occurs with increased monomer concentration and temperature. Surfactants also play a key role in nanoparticle growth because they usually slow down the growth process as they need to be removed for monomer incorporation. Generally, the nanoparticle growth can occur in different ways. The first growth method is through monomer addition and another growth method is known as oriented attachment. In oriented attachment, small nanoparticle seeds attach to each other with a common crystallographic orientation. This method is often used to explain anisotropic nanocrystals such as nanorods or nanowires. Coalescence is yet another growth type, different from oriented attachment because, in coalescence, the seeds attach to each other without a crystallographic orientation.^{6,13}

The growth rate can be defined as a change of a nanoparticle radius r over time t . Together with the diffusion coefficient of the monomers D , the molar volume of the solid V_m , the activity of the monomer in the solution a_m , the activity of the monomer on the nanoparticle surface a_s , and the reaction constant K_S , Equation 7 is obtained to describe the growth rate:¹³

$$\frac{dr}{dt} = \frac{D V_m (a_m - a_s)}{r - (D/K_S)} \quad (7)$$

Based on Equation 7, the diffusion depends on the concentration gradient between the solution and the nanoparticle surface. This also demonstrates the impact of the rate-determining step on the overall process. In a reaction-controlled regime, the monomer incorporation and their reaction on the nanoparticle is the rate-determining step, thus making the reaction constant K_S and the nanoparticle radius r smaller compared to the monomer diffusion D . This is opposite to the diffusion-controlled regime, where the monomer diffusion is the rate-determining step and smaller compared to the nanoparticle radius and the reaction constant. Taking Equation 7 into account, the reaction-controlled regime can be simplified into Equation 8 and the diffusion-controlled regime can be described as Equation 9.^{6,13}

$$\frac{dr}{dt} = V_m K_S (a_m - a_s) \quad (8)$$

$$\frac{dr}{dt} = \frac{D V_m (a_m - a_s)}{r} \quad (9)$$

The monomer concentration is expected to be the highest at the beginning of the growth process. In that case, the diffusion rate of the monomers is the fastest step thus making it a reaction-controlled regime. During the growth process, more and more monomers are being incorporated into nanoparticles. Thus, the monomer concentration decreases over time. Consequently, the

monomer diffusion will become the rate-determining step. Furthermore, the dissolution of the nanoparticles also becomes relevant because of the now slowed down growth process.¹³ The dissolution process depends on the nanoparticle size which is best described by the Gibbs-Thomson relation in Equation 10:^{6,13}

$$a_s = a_e \exp\left(\frac{2\gamma V_m}{r k_B T}\right) \quad (10)$$

In Equation 10, a_e is the activity of the monomer in equilibrium in the solution, and γ is once again the surface energy, specifically the interfacial surface tension. The Gibbs-Thomson relation can be used to define a critical nanoparticle size r^* if the monomer activity in the solution is assumed to be in equilibrium ($a_m = a_s$). In that case, the growth rate of a nanoparticle can be described in the following Equation 11:^{6,13}

$$\frac{dr}{dt} = \frac{2\gamma D a_e V_m^2}{k_B T r} \left(\frac{1}{r^*} - \frac{1}{r}\right) \quad (11)$$

Consequently, the monomer activity determines the size distribution of the final nanoparticles based on Equation 11. It should be noted that monomer concentration can also be used instead of activity for systems with ideal behavior. A high monomer activity leads to a small critical nanoparticle size. Thus, many small nanoparticles start to grow. The growth process depends on the surface area. Hence, smaller nanoparticles grow much faster compared to bigger nanoparticles. Furthermore, bigger nanoparticles also need more material to grow compared to smaller nanoparticles. Due to the difference in growth speed between the bigger and smaller nanoparticles, a small size distribution is the result. Compared to the high monomer activity, the low monomer activity means the critical nanoparticle size is large. Small nanoparticles dissolve and disappear while the already bigger nanoparticles keep growing bigger. This process is called Ostwald ripening and leads to a broad size distribution. The main driving force behind the Ostwald ripening is reducing the surface free energy of the nanoparticles. The dependence of the monomer activity on the growth rate and the final size dispersion of the nanoparticles is shown in Figure 8.^{6,13}

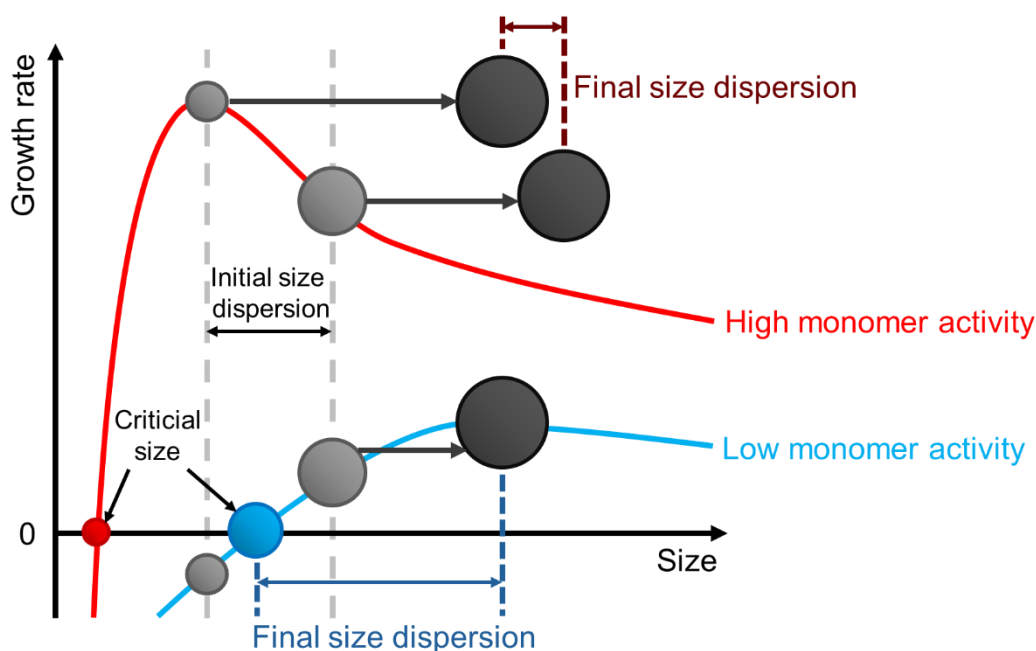


Figure 8: The growth rate for nanocrystals (grey) with a high monomer activity (red) and a low monomer activity (blue). Shown as a red and blue circle is the critical size, which indicates the minimum size needed for growth, for the different monomer activities. The size distribution narrows for a high monomer activity, while it broadens for a low one. The image is recreated from the literature.¹³

LaMer introduced a theoretical model to produce monodisperse nanoparticles, which is presented in Figure 9.^{6,13,15,35} In general, the nucleation and growth of monodisperse nanoparticles follow three main steps. At first, the necessary precursors are added to the solution so that the monomer concentration increases rapidly (Figure 9 I). Once the monomer concentration exceeds a critical concentration, the second step starts, which is the nucleation step (Figure 9 II).^{6,13,15,35} As discussed before, the monomer concentration is high, and the critical radius is small, so there are many nuclei at this stage.^{6,13} At one point, the consumption of the monomers to form nuclei is faster than the production of new monomers. As a result, the concentration is decreasing again until it is lower than the critical concentration. The growth stage starts, in which the already formed and stable nuclei begin to grow through monomer diffusion processes (Figure 9 III). In this final stage, no new nuclei are forming. This growth stage can last until an equilibrium of the monomer concentration is reached. However, reaching this equilibrium also results in a size broadening of the nanoparticles. As a result, reaching this equilibrium is not desired to achieve monodisperse particles.^{6,13,15,35}

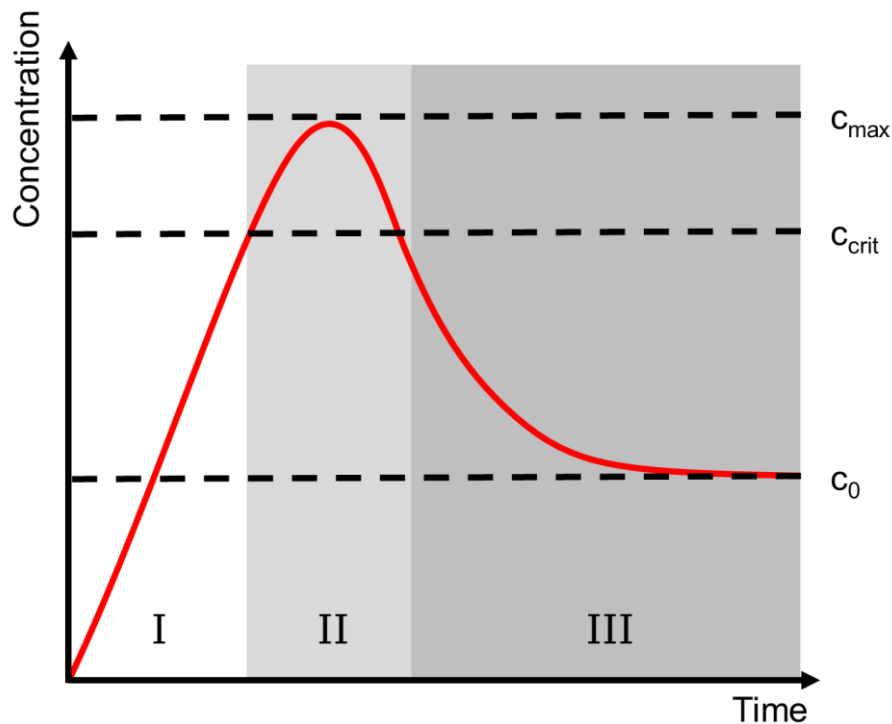


Figure 9: The LaMer Model and its three stages. In the first stage, the precursors are added, also known as the pre-nucleation step. The second stage represents the nucleation, and the final third stage is the growth process. At c_0 , the concentration of monomers is saturated. A supersaturation is reached at a level above c_{crit} . The image is recreated from the literature.¹³

A separation of nucleation and growth is key to obtaining monodisperse nanoparticles in theory. In 1993, Bawendi et al. developed a method to synthesize semiconductor CdSe, CdS, and CdTe quantum dots with a very narrow size distribution, which includes this separation.³⁶ Aside from the spherical quantum dots, anisotropic shapes were also investigated further. In the early 2000s, Alivisatos et al. discovered that the growth of CdSe nanorods along the c -axis of the wurtzite crystal structure depends on a kinetic overdrive of the reaction because wurtzite CdSe has a unique c -axis based on its crystal structure which allows to favor growth along this axis.³⁷ The nanorod synthesis also strongly depends on the selective binding of ligands onto the surfaces.³⁸ The two-dimensional CdSe NPLs, also called nanoribbons,³⁹ nanosheets,⁴⁰ and quantum belts,⁴¹ were first reported with a wurtzite structure in 2006,³⁹ then in 2008 with a zinc blende structure.²² While for CdSe quantum dots,³⁶ nanorods^{37,38} and wurtzite CdSe NPLs^{42,43} the growth mechanism is investigated, the growth mechanism for zinc blende CdSe NPLs is not fully discovered yet.

The wurtzite CdSe NPLs growth mechanism involves the formation of a lamellar mesophase out of the cadmium chloride and n -octylamine solvent. By adding selenourea, CdSe magic-size

clusters (MSCs) as $(\text{CdSe})_{13}$ clusters form as intermediates in this molecular template before they finally turn into the wurtzite CdSe NPLs.⁴¹

Riedinger et al. investigated the theory that molecular templates are involved in the formation of zinc blende CdSe NPLs.¹⁰ In their research, they found no involvement of a lamellar mesophase during the growth of zinc blende CdSe NPL.¹⁰ The absence of a lamellar mesophase is also confirmed by another group.⁴⁴ Instead, Riedinger's group proposes a zinc blende CdSe NPL growth mechanism based on kinetic instabilities.¹⁰ The regular protocol to synthesize zinc blende CdSe NPL involves a mixture of selenium powder and a non-coordinating solvent. Moreover, long and short-chain carboxylates are needed, where one of the carboxylates includes cadmium. This mixture is heated to 240 °C for 5 to 15 minutes.^{22,44,45}

Riedinger et al. performed a CdSe NPLs synthesis without using a solvent and used only the pure cadmium precursor and selenium precursor. The chain length of the longer cadmium carboxylate did not affect the CdSe NPLs formation. Moreover, they did not even need a mixture of two carboxylates with different chain lengths to obtain CdSe NPLs without a solvent. Next, they investigated how the solubility of the cadmium precursor determines whether CdSe quantum dots or CdSe NPLs are being produced. If the cadmium precursor is likely to dissolve in the solvent, CdSe quantum dots are likely to form. However, if the cadmium precursor is not soluble in the solvent, phase-separated droplets appear within the solvent, which favors the formation of CdSe NPLs in the concentrated droplets. Based on these experiments, they propose that a mixture of a short and a long cadmium carboxylate is not necessary for the synthesis of CdSe NPLs. Instead, they conclude that the cadmium carboxylate component simply needs to be insoluble in the solvent to promote the formation of CdSe NPL. Since CdSe NPLs can be synthesized without a solvent in concentrated melts, they theorize that the growth of the CdSe NPLs is not diffusion-limited but instead surface-nucleation-limited. The Riedinger group thus presented a growth model for CdSe NPLs which includes the kinetic instabilities. In general, the formation of new edges is energetically more expensive than the formation of a new surface area. On narrow facets, the highest energy barrier lies in the formation of a nucleation island that spans the facet width. No additional energy is needed to complete the layer once the island nucleus covers the narrow facet's width. Furthermore, the nucleation barrier on narrow facets is less expensive compared to the wide facets. For wide facets, the island nucleation is energetically favored in a corner. The different energy barriers between the narrow and wide facets also explain the observation of thicker CdSe NPLs forming by controlling temperature and

time. In Figure 10, the growth model is shown with the narrow and wide facets of a NPL and the difference between edges and surfaces.¹⁰

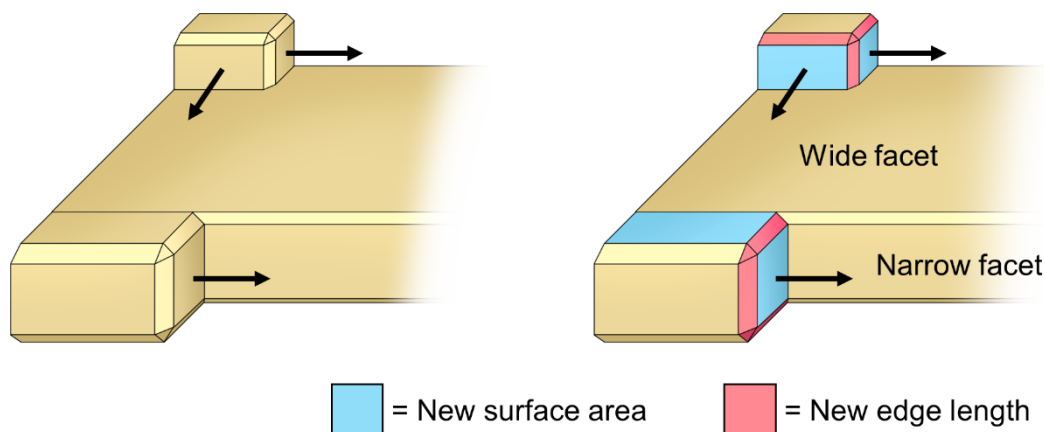


Figure 10: The CdSe NPL growth model by Riedinger.¹⁰ The model shows where the island nuclei are forming and how they expand the facet to minimize their energy. The image is recreated from the literature.¹⁰

In contrast to the growth model by Riedinger, Peng et al. propose a CdSe NPL growth model that involves oriented attachment and intraparticle ripening.¹¹ Their growth model is based on their synthesis in which spherical CdSe seeds with a size between 1.7 and 2.2 nm grew into CdSe nanoplatelets with a thickness of 1.5 nm. In the first step, the spherical CdSe seeds turn into single-dot intermediates through intraparticle ripening. This ripening process also involves a slight shrinkage to grow slightly in lateral dimensions. These single-dot intermediates now have two flat surfaces with a $\{100\}$ facet and $\{110\}$ side facets. The second step assumes that the $\{100\}$ facets are well passivated so that an oriented attachment of two single-dot intermediates on the $\{110\}$ side facets is the favorable process. Through this oriented attachment of the single-dot intermediates, a so-called 2D embryo is forming. Like before, the oriented attachment on the reactive $\{110\}$ facets is still favored. Next to the oriented attachment process, the intraparticle-ripening also occurs until these 2D embryos turn into NPLs and their $\{110\}$ side facets mature to $\{100\}$ facets.¹¹ This growth process is similar to the oriented attachment process of the PbS sheets found by Weller et al.⁴⁰ Peng et al. conclude that the long-chained carboxylates used in the synthesis stabilize the $\{100\}$ facet and channel the short-chained carboxylates to the reactive surfaces of the nanocrystals.¹¹

The growth of the semiconductor CdSe NPLs can also be influenced by the introduction of halides into the synthesis.⁴⁶⁻⁴⁸ Halides are generally known to enhance the growth rate on specific facets, allowing for nanoparticle shape and size control.⁴⁶ In the case of CdSe NPLs, the

addition of halides promotes the growth in thickness of the NPLs.⁴⁶⁻⁴⁸ Although the particles produced with halides are thicker, their optical properties, including the sharp absorption and emission peaks, are retained.⁴⁶ Furthermore, the quantum yield (QY) improved for these thick CdSe NPLs synthesized with halides. Chlorides and fluorides in particular work best for these CdSe NPLs, even allowing to control the lateral dimensions of these NPLs.⁴⁷ It was reported that not all surfaces of the CdSe NPLs need to be passivated by the chloride. Instead, a small amount of chloride is sufficient to promote the growth in thickness. Based on these reports, it was theorized that the chloride is temporarily reducing the nucleation barrier in the thickness direction by modifying the lateral surface energies of the CdSe NPLs.⁴⁶ Furthermore, the growth mechanism in the thickness direction was proposed to be similar to Ostwald ripening.⁴⁹

4.2.2 Magic-size clusters

As mentioned in Chapter 4.2.1, MSCs act as intermediates in semiconductor nanoparticle synthesis and have been known for many years.^{50,51} They usually describe clusters with a precise number of atoms and a size below 2 nm.⁵² Interestingly, only clusters of a specific size appear, which have a higher stability than bigger or smaller cluster arrangements. This appearance of certain cluster sizes is what the term “magic” describes in MSCs.⁵¹⁻⁵³ The MSCs have a discrete growth and “jump” from one cluster size to a bigger cluster size.^{51,53} Similar to MSCs, CdSe NPLs also have a discrete growth based on their growth in thickness. The bigger NPLs and MSCs can be controlled through reaction time and temperature. Although MSCs have been discovered a long time ago, their growth mechanism has not yet been fully discovered.⁵³ Known aspects are that the formation of CdSe MSCs strongly depends on ligands^{51,52} and that either fully reduced selenium or fully oxidized cadmium is needed to synthesize them.⁵³ The ligands may form lamellar mesophases during a synthesis, which promotes the formation of MSCs.⁵¹ Other proposed growth mechanisms of MSCs include layer-by-layer growth and a fusion mechanism in which smaller clusters fuse together to form larger clusters.⁵³ Furthermore, the formation of nonstoichiometric or stoichiometric MSCs also depends on the ligand type, where L-type ligands promote the growth of stoichiometric MSCs. Meanwhile, X- and Z-type ligands promote the growth of nonstoichiometric MSCs.⁵¹

4.2.3 Flow reactor

In the industry, many different reactor types are available for suitable synthesis methods for various products. The batch reactor is suited for longer reaction times.⁵⁴ In an ideal approximation, the batch reactor has a uniform mixing, meaning that the concentration changes over time.^{55,56} In a non-continuous operation, the batch reactor suits smaller product quantities. It

becomes more suitable for larger product volumes if the batch reactor is operated continuously (also called continuous flow stirred tank reactor, CSTR). Also, the time required for heating and cooling is reduced.^{54,56} Similar to a CSTR, a flow reactor is also a good choice for larger product quantities.⁵⁶ Compared to a batch reactor, fast and high-temperature syntheses are more suitable for a flow reactor.^{54,56,57}

The decision on the reactor type also depends on the scale-up of the synthesis. Relevant aspects include the heating and cooling of the synthesis, as well as pressure and volume changes during the synthesis. For flow reactors specifically, the viscosity of the fluid is relevant as it affects the axial mixing and the overall flow behavior.⁵⁴ The term viscosity can be further divided into dynamic and kinematic viscosity. Dynamic viscosity describes the proportionality between the shear strain needed to move a viscose fluid with a certain thickness and area size between two surfaces so that a certain velocity gradient forms within the fluid. Compared to dynamic viscosity, kinematic viscosity describes the ratio between the dynamic viscosity and the density of the liquid.⁵⁸

Dimensionless numbers can be used to compare the physical attributes of reactors with one another.^{55,59} The Reynolds number Re is used to describe the flow behavior in flow reactors. This dimensionless number depends on the velocity of the fluid u , the density of the fluid ρ , the characteristic reactor length L_R , and the dynamic viscosity of the fluid η , as shown in Equation 12.^{54,55,60}

$$Re = \frac{u \rho L_R}{\eta} \quad (12)$$

The characteristic length of a flow reactor with cylindrical tubes depends on the inner diameter of the tube.⁵⁴ If the Reynolds number has a value above 2300, the fluid in the reactor is in the turbulent flow regime. Below that value, the fluid is in the laminar flow regime. As the Equation suggests, the flow behavior depends on the fluid's dynamic viscosity.^{54,55,60} Hence, a laminar flow cannot be avoided for very viscose fluids.⁶¹ Additionally, the laminar flow regime is defined as a Reynolds number below 500 for microstructures.⁶⁰ Aside from calculating the Reynolds number, tracer experiments can also determine the flow regime in a flow reactor.^{56,57,61,62} For this experiment, a tracer-substance with a constant concentration is added to the flow reactor. In an ideal plug flow reactor, the tracer molecules all have the same residence time.^{56,57,62} A residence time describes the interval one molecule needs to enter and pass the reactor.⁶² There is no gradient of velocities in the reactor and no concentration gradient as there is an ideal

mixing in the axial direction.^{61,62} The response function of the ideal plug flow reactor is thus an ideal step-response.^{54,61,62} This response function for the plug flow reactor, as well as for the laminar flow reactor, is shown in Figure 11.^{54,61} For non-ideal turbulent flow, there are some velocity differences. However, the overall velocity profile is flat and is comparable to an ideal plug flow reactor.⁵⁴ In a laminar flow profile, the tracer molecules have a distributed residence time because a velocity gradient is present in the flow reactor.^{54,61} The molecules in the middle have a halved average residence time compared to the particles near the reactor walls, which move with reduced velocity.⁶¹ Figure 11 shows these individual flow profiles within a tube, as well.^{54,61}

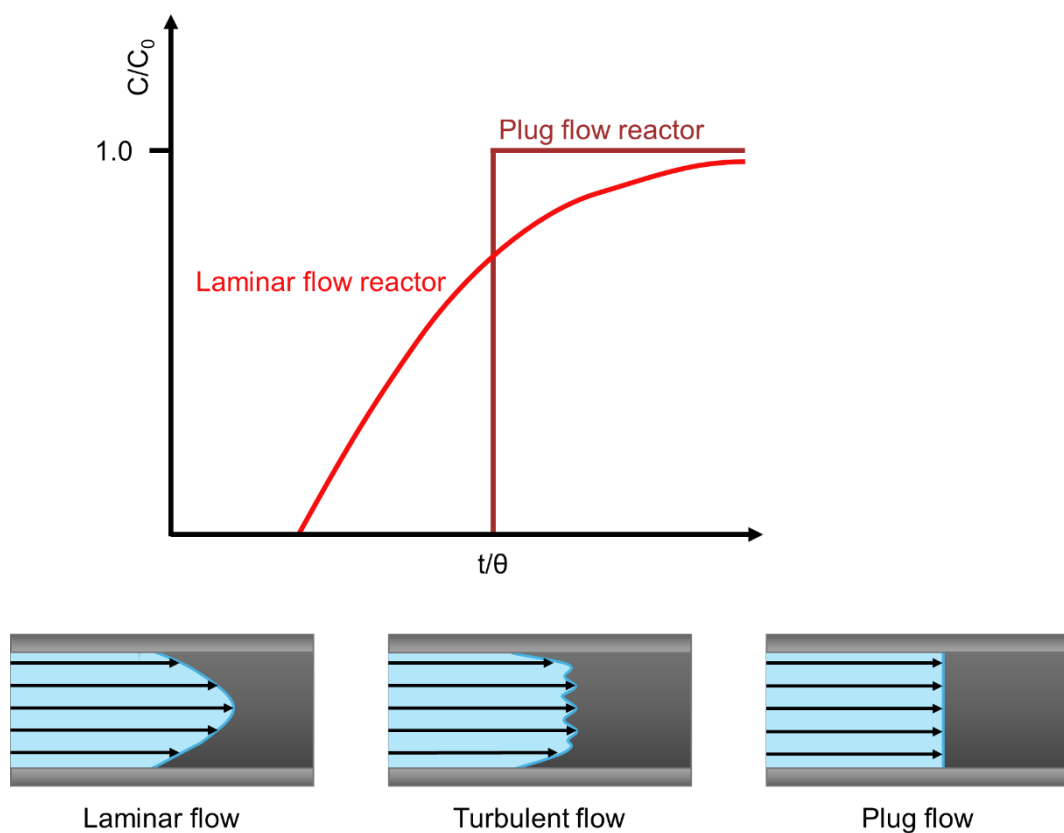


Figure 11: The graph shows the residence time distribution for a plug flow reactor (dark red) and a laminar flow reactor (red). The individual flow profiles for a laminar, turbulent, and plug flow reactor are schematically drawn in a tube. In the schematic drawings, the back arrows indicate the velocity of the fluid. The image is recreated from the literature.^{54,61}

The mean residence time θ in Equation 13 also describes the ratio between reactor volume V_R to the volumetric flow u .⁶¹

$$\theta = \frac{V_R}{u} \quad (13)$$

Similar to the dimensionless Reynolds number, the mean residence time θ and time t are replaced with the dimensionless time variable τ in Equation 14.⁵⁴

$$\tau = \frac{t}{\theta} \quad (14)$$

For flow reactors, the scale-up process is realized using different techniques. One method to scale up a flow reactor is to increase the tube's length. A higher flow rate can be applied if the heating and cooling zones of the tube are also increased in size. Consequently, a higher product capacity is achieved with this method. Another scale-up method is simply expanding the reactor tube's diameter and length to maintain similar geometrics. The final scale-up method is the number-up method.⁵⁶ This method can be further divided into an external or internal number-up. The external method is the most expensive technique as it describes the operation of multiple units in parallel. Compared to this method, the internal method relies on two bigger tubes that are combined in a mixing zone, and the mixed fluids are further divided into built-in microchannels.⁵⁶

4.2.4 Polymer encapsulation of semiconductor nanoplatelets

Nanoparticles are usually synthesized with hydrophilic ligands in an organic solvent like 1-octadecene. These ligands, like oleic acid and oleylamine, hinder biocompatible applications as the particles need to be soluble in water. A method to make these hydrophilic nanocrystals biocompatible and water-soluble is through amphiphilic diblock-copolymers and encapsulation of these nanoparticles in a polymer shell.⁶³ Especially the usage of poly(ethylene oxide) (PEO) and poly(ethylene glycol) (PEG) are favored as parts for diblock-copolymers as they show a good degree of resistance against unspecific protein adsorption.⁶⁴ Furthermore, nanoparticles of any shape, size, and material can be encapsulated like anisotropic semiconductor CdSe NPLs.⁶³

The seeded emulsion polymerization contains three essential steps to make hydrophilic nanoparticles biocompatible.⁶³⁻⁶⁵ These steps are shown as arrows in Figure 12.⁶³ At first, the hydrophilic CdSe NPLs (Figure 12, 1) are transferred into the water phase through the formation of micelles (Figure 12, 2).⁶³⁻⁶⁵ In order to perform the water transfer, a surfactant is needed.⁶³ These surfactants can be different amphiphilic molecules like polysorbate-80 or polyisoprene-block-poly(ethylene oxide) diblock-copolymer (PI-b-PEO).^{63,66} The original hydrophilic ligands, in the case of CdSe NPLs oleic acid, remain on the surface of the NPLs during this process.⁶⁴ During the water transfer, the surface surfactants on the CdSe NPLs support the form of a micelle around the CdSe NPLs.⁶⁷ These newly formed and filled micelles are also called

“seeds”.⁶³ In this step, the amount of CdSe NPLs per seed can be tuned. A high amount of surfactant enables the formation of many micelles, hence allowing for single CdSe NPLs to be encapsulated. In comparison, a low amount of surfactant creates fewer micelles, so clusters of CdSe NPLs are expected within the micelles.^{63,66}

As a next step, polymerizable monomers are added and accumulate in the hydrophobic bilayer part of the micelles (Figure 12, 3). They ensure a good cross-linking with ligands to form a tight copolymer-polymer-shell around the NPLs, improving their stability in the water phase.⁶³ Typical functional groups for this type of polymerization are C-C double bonds; typically used monomers are styrene and divinylbenzene.⁶⁵

Finally, the polymerization is initiated through a thermally activated radical starter (Figure 12, 4). For the seeded emulsion polymerization, the typically used radical starters are 2,2'-Azobis[2-(2-imidazoline-2-yl)propane] dihydrochloride, also known as VA-044, and azobis(isobutyronitrile), which is also known as AIBN.^{63,67}

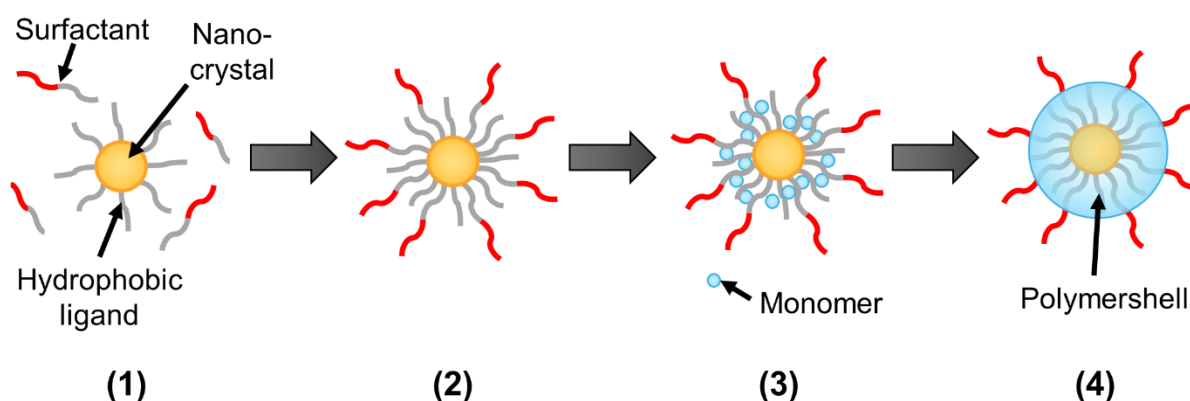


Figure 12: The seeded emulsion polymerization in four stages. (1) shows the nanoparticle in an organic solvent. In (2), the nanocrystal is in water with the surfactants on its surface. (3) shows the swelling of the nanocrystal with monomers and (4) shows the nanocrystal in a finished polymer shell. The image is recreated from the literature.⁶³

After polymerization, the polymer micelles are not only filled with nanoparticles, but some remain empty. To separate them, a density centrifugation is performed.⁶⁴ This density centrifugation can be either performed with a sucrose gradient or with a glucose gradient.^{64,68}

4.3 Characterization of semiconductor nanoplatelets

4.3.1 Optical spectroscopy

4.3.1.1 Absorption spectroscopy

In semiconductor nanocrystals, an exciton is created through the absorption of a photon (Chapter 4.1). As the band gap of these nanocrystals is size-dependent, a higher energy photon is needed for the absorption process in smaller nanocrystals compared to bigger nanocrystals.^{12,13} This demonstrates that absorption spectroscopy makes it possible to obtain information on the optical transitions of the electron from the valence into the conduction band.¹³ In this absorption spectroscopy method, monochromatic light passes through a sample with a range of wavelengths. The light intensity at the beginning attenuates after passing the sample. This observation is based on the Lambert-Beer law, which is expressed in Equation 15. In Equation 15, the absorbance is presented as A , the initial intensity of the light as I_0 , the intensity of the transmitted light I , the molar absorption coefficient as ε , the concentration of the analyte as c , and the length of the sample as L_c .^{12,69}

$$A = \log \frac{I_0}{I} = \varepsilon c L_c \quad (15)$$

The correlation between the absorbance and the transmittance T_T can be defined in Equation 16.¹²

$$A = -\log T_T \quad (16)$$

In an absorption spectrum, the amount of absorbance strongly depends on the wavelength of the light source, which is in the ultraviolet-visible range (UV-Vis). Other physical processes can take place during the measurement, influencing the absorbance. Such processes include light scattering processes, like elastic Rayleigh scattering, inelastic scattering, and reflection.⁶⁹

4.3.1.2 Fluorescence spectroscopy

Together with absorption spectroscopy, fluorescence spectroscopy also enables to obtain information about the energy levels in semiconductor nanocrystals. During the formation of the exciton, a photon of higher energy may be absorbed, causing the exciton to occupy higher states than the ground state of the valence and conduction band. In such cases, the charge carriers undergo a non-radiative relaxation to reach the ground state of the valence and conduction band again. These non-radiative relaxations can be lattice vibrations or Auger scattering. The latter describes the energy transfer from one charge carrier to another charge carrier. Once the

electron-hole pair reaches their ground states, the exciton's recombination occurs in either a radiative or non-radiative manner.¹³

In the first case, the radiative manner, the recombination of the exciton emits a photon to release its energy.¹³ Very often, the wavelength of this emitted photon is higher, so smaller in energy compared to the smaller, higher energetic wavelength needed for the absorption. As mentioned before, the as-formed exciton loses energy through non-radiative processes. This energy difference in the absorption and emission of a nanocrystal is called Stokes shift.⁶⁹

The second pathway, the non-radiative recombination of the exciton, occurs due to trap states. These trap states result from surface defects due to many unsatisfied bonds on the surface or as defects within the crystal lattice.¹³ With a high surface-to-volume ratio, nanocrystals are especially affected by surface defects.^{1,13} The trap state, as the name suggests, strongly localizes a charge carrier, which hinders recombination with its counterpart as the electron-hole-wavefunction overlap decreases.¹³ In another scenario, the exciton recombination can transfer its energy to another charge carrier. This other charge carrier releases its excess energy non-radiatively through lattice vibration, making this whole process also known as Auger recombination.⁷⁰ Sometimes, the recombination occurs radiatively by emitting a photon. However, the photon emitted has a lower energy than other emitted photons, as more energy was lost in the trap state, leading to a broadening of the emission band. To reduce the amount of surface defects, the nanocrystals need to be passivated. This passivation can occur through ligands or the growth of a shell.¹³ In Figure 13, the different recombination pathways of the exciton are depicted.⁷¹

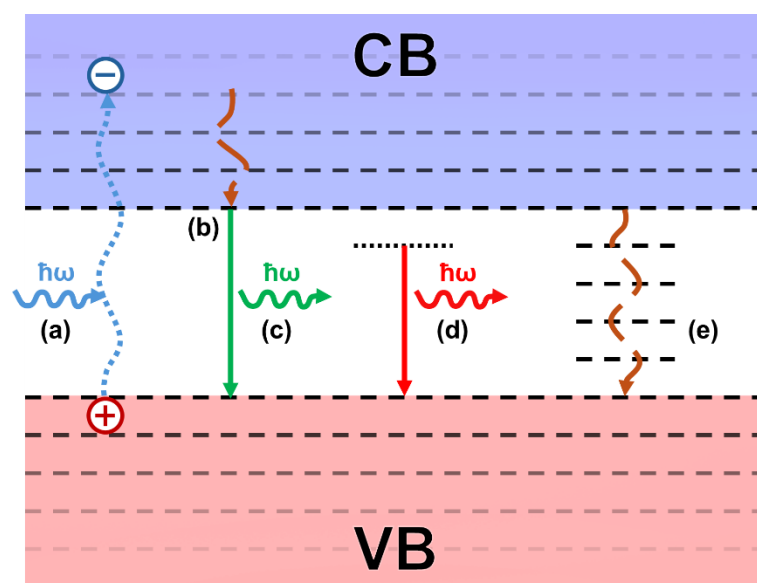


Figure 13: Schematic presentation of the absorption and the multiple emission processes. At first, a photon is absorbed, which leads to the formation of the exciton (a). After lattice vibrations (b), the electron-hole pair can recombine radiatively through the emission of a photon (c). In (d), the emission through a trap state is depicted, and in (e), the non-radiative recombinations through lattice vibrations. The image is recreated from the literature.⁷¹

A third pathway for recombining an exciton is the fluorescence resonance energy transfer, also called Förster resonance energy transfer (FRET).⁷² For this energy transfer to happen, a few conditions must be met.^{12,13,72} One condition is that the acceptor and donor molecule need to be close to one another, in a range of one to ten nanometers. The second condition is that the absorption of the acceptor must spectrally overlap with the emission of the donor. Despite this second condition suggesting this energy transfer could be radiative, the energy transfer is indeed non-radiative and occurs through dipole-dipole interactions between the acceptor and donor.^{13,72} In the case of CdSe NPLs, a so-called HOMO-FRET is observed.⁷³ The FRET conditions are also shown in Figure 14.⁷⁴

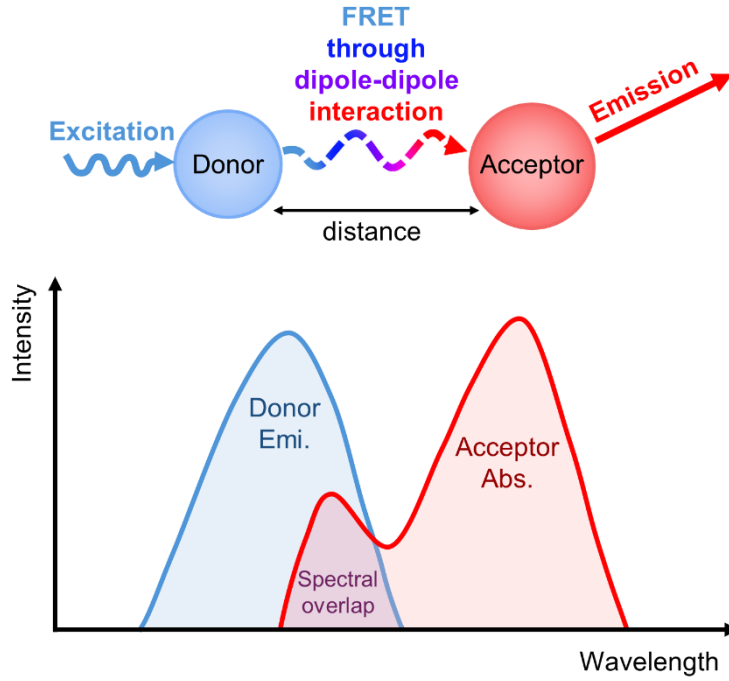


Figure 14: The FRET process and its conditions are shown. The excited donor and non-excited acceptor need to be close to one another for the dipole-dipole interaction to happen. After the energy transfer, the acceptor can undergo an emission process. Another condition is that the donor's emission must overlap with the acceptor's absorption spectrally. The image is recreated from the literature.⁷⁴

The transfer rate of FRET Γ_{FRET} can also be calculated in Equation 17. Based on the FRET conditions described above, the normalized emission spectrum of the donor $E_D(\lambda)$, as well as the normalized acceptor spectrum of the acceptor $A_A(\lambda)$, need to be known. Furthermore, the dipole moment of the donor μ_D and the acceptor μ_A are required, as well as the average orientation of both dipoles κ^2 . Finally, the distance between donor and acceptor $r_{D,A}$, the refraction index of the medium n_r , and once again, the reduced Planck constant \hbar is also needed to determine the FRET transfer rate.^{13,75}

$$\Gamma_{\text{FRET}} = \frac{2\pi \mu_D^2 \mu_A^2 \kappa^2}{\hbar r_{D,A}^6 n_r^4} \int E_D(\lambda) \cdot A_A(\lambda) d\lambda \quad (17)$$

It becomes apparent that not every exciton recombines through the emission of a photon. A method to evaluate the efficiency of the emission is through the quantum yield QY . It describes the ratio between the emitted ϕ_E and the absorbed photons ϕ_A , as shown in Equation 18.^{13,69}

$$QY = \frac{\phi_E}{\phi_A} \quad (18)$$

In practice, the indirect quantum yield is a frequently used method. This method uses a reference sample with a known quantum yield within a specific medium. One prominent reference

is Rhodamine 6G, with a quantum yield of 95 % in ethanol.⁷⁶ In the case of CdSe NPLs, coumarin 153 is a better-suited reference with a reported quantum yield of 54 % in ethanol.⁷⁷ Coumarin 153 has a better optical overlap with CdSe NPLs than Rhodamine 6G.^{77,78} With the integrated fluorescence intensity F , the absorbance at a certain excitation wavelength A_E , the known quantum yield of the reference QY_{Ref} , and the refraction index of the medium n_r , the indirect quantum yield can be determined in Equation 19. In this Equation, the subscript ‘‘Ref’’ stands for reference and ‘‘S’’ for sample.⁷⁶

$$QY_S = QY_{\text{Ref}} \frac{F_S}{F_{\text{Ref}}} \frac{A_{E,\text{Ref}}}{A_{E,S}} \frac{n_{r,S}^2}{n_{r,\text{Ref}}^2} \quad (19)$$

Another method to evaluate the emission is through the fluorescence lifetime. After the excitation of a nanocrystal at a certain wavelength, the emission’s total amplitude Y_{em} decays exponentially over time t_{em} . Assuming a nanocrystal has only a radiative recombination of its exciton, the fluorescence decay F_{em} can be described with a single exponential decay in Equation 20.⁶⁹

$$F_{\text{em}}(t_{\text{em}}) = Y_{\text{em}}(t_{0,\text{em}}) e^{-\frac{t_{\text{em}} - t_{0,\text{em}}}{\tau_{\text{em}}}} \quad (20)$$

The Equation shows that this single decay has its own time constant τ_{em} .⁶⁹ As nanocrystals exhibit multiple radiative exciton recombinations, the fluorescence decay shows a multiexponential behavior, as shown in Equation 21.^{13,79}

$$F_{\text{em}}(t_{\text{em}}) = Y_{\text{em}}(t_{0,\text{em}}) \sum_{i=1}^p y_i e^{-\frac{t_{\text{em}}}{\tau_{\text{em},i}}}, \text{ with } \sum_{i=1}^p y_i = 1 \quad (21)$$

Above, the amplitude fractions y_i and fluorescence lifetimes $\tau_{\text{em},i}$ are also described for the number of lifetime components p .⁸⁰ Overall, the fluorescence lifetime describes different excited-state populations, which show different fluorescence decay behaviors. One way to determine the average fluorescence lifetime is to use the intensity-weighted one. Every lifetime population is then weighted by its contribution to the total fluorescence intensity. This intensity-weighted fluorescence lifetime FLT is reported in Equation 22.⁷⁹

$$FLT = \frac{\sum y_i \tau_{\text{em},i}^2}{\sum y_i \tau_{\text{em},i}} \quad (22)$$

4.3.2 X-ray scattering

When working with nanocrystals, obtaining information on the nanoparticle's shape, interparticle distances, size distribution, and arrangements is essential. One method to obtain this information is through X-ray beams.^{12,81} The X-ray beams, with their wavelengths of around 0.1 nm, can diffract when passing through a sample, as their size is similar to the spacing between the crystal lattice planes.¹² Therefore, obtaining information on nanoscale systems starting at 0.5 nm up to 100 nm is possible. These X-ray beams can scatter or diffract on the sample. Some of the X-ray beams can be absorbed, in which the excess energy is removed through heat or emitting a photon.⁸¹

In a nanocrystal's crystal lattice, the periodically ordered atoms within a plane have a specific distance d_C to one another and between the crystal planes. The incoming X-ray beams have various angles, which leads to scattering. However, it is possible that constructive interference, similar to a reflection, occurs. This X-ray diffraction is based on the fact that the path length within a crystal plane is not uniform for X-ray beams. Thus, the X-ray beams must align with the path difference, which equals one whole wavelength λ . In this case, the incident X-ray angle δ on one atom of a plane is the same as the scattering X-ray angle on a second atom of a different plane. The X-ray diffraction has been put into the so-called Bragg law, in which n_p refers to the different path lengths, hence the different diffraction orders. In Equation 23, the Bragg law is demonstrated.^{12,82}

$$n_p \lambda = 2d_C \sin\delta \quad (23)$$

In Figure 15, the mechanism behind the X-ray diffraction, according to the Bragg law, is also shown.^{12,82}

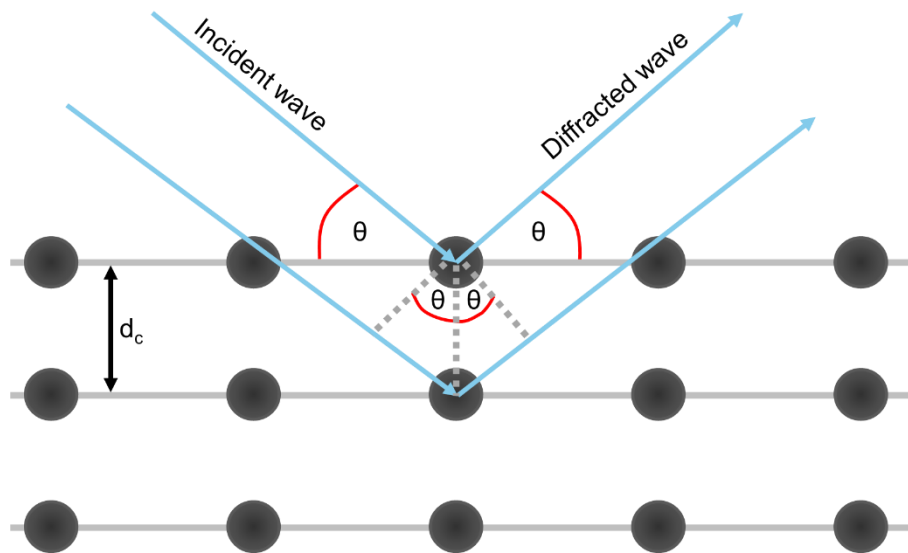


Figure 15: The Bragg reflection conditions. On each plane, the X-ray beam can be diffracted, which depends on the angle δ and the path length difference between the planes d_c . The image is recreated from the literature.^{12,82}

One method of using X-ray beams is through the powder diffraction technique. A rotating detector detects the different diffraction intensities of a solid sample, making it possible to obtain information on the sample's crystal structure.¹² Another method is to use the small-angle X-ray scattering (SAXS) technique. Here, the scattered X-rays are recorded on a two-dimensional detector.⁸¹

5 Motivation and Goal

The anisotropic semiconductor CdSe NPLs exhibit exciting and unique properties like their thickness-dependent and narrow absorption and emission peaks. Synthesis settings such as temperature, reaction time, or the addition of halides make it possible to control the thickness with monolayer precision and, thus, their optical properties. Compared to nanodots, this is a great advantage, where very monodisperse quantum dots are needed to get narrow absorption and emission peaks. Nanoplatelets only need the desired thickness, while their lateral size can vary without impacting the broadness of the absorption and emission. However, a slight lateral size of nanoplatelets is still desired for a high quantum yield. The larger the nanoplatelets, the smaller is their quantum yield.

The growth mechanism needs to be understood to utilize these excellent properties of CdSe NPLs. Based on the current literature, long and short carboxylate chains are favored for a solvent-based synthesis. Another goal is to find a synthesis that is useable for a flow reactor for multiple reasons. The first reason is that a suitable flow reactor synthesis allows access to mass-produce CdSe NPLs commercially. Next, the flow reactor provides for an exact control of the reaction time and temperature. Flask-synthesis approaches are easy to conduct but flawed since the cool-down process of such synthesis approaches is challenging for reproduction purposes. Another issue is that the heat-up rates of flask-synthesis approaches can vary and takes up time, which also impacts the synthesis a lot. The third and most important reason is that the flow reactor can be connected to characterization devices like online UV/Vis spectrometers. This allows the synthesis of CdSe NPLs to be monitored *in situ* and data to be obtained before the CdSe NPLs form. Therefore, getting more information about the formation of CdSe NPLs, which is even reproducible, could be accessed with a flow reactor synthesis method.

Semiconductor nanoparticles can be used for many applications, including medical diagnostics if they are water-soluble. Making semiconductor NPLs water soluble is challenging because their optical properties need to be preserved to prevent quenching from the water. One possible solution to this problem is encapsulating the semiconductor nanoplatelets in a polystyrene-copolymer shell. This not only allows the transfer of these NPLs into NPL but these shells protect the NPLs from proteins and other substances which could affect their properties. Furthermore, the polystyrene-copolymer shell can be modified to enable medical diagnostic purposes.

In this work, a flow reactor synthesis method for CdSe NPLs is presented. The flow reactor is connected to an absorption spectrometer so that *in situ* measurements of the earliest stages of the synthesis are possible. Furthermore, a potential connection between CdSe NPLs and CdSe

MSCs is highlighted. Thus, this work presents a growth mechanism model for forming the CdSe NPLs. Then, experiments are showcased where a CdS shell and polystyrene - PI-b-PEO shell were added to the CdSe NPL. These experiments act as proof of principle concepts. Thus, the CdSe NPLs can not only be modified like their spherical counterparts, but both experiments open a possible pathway for using these platelets for medical imaging applications. All of these methods combined should act as a stepping stone to use CdSe NPLs more often in the future.

6 Results and discussion

6.1 Finding a flow reactor suitable CdSe NPL synthesis

The first task is to find a CdSe NPL synthesis which is suitable for a flow reactor. To accomplish this, all precursors need to be in a liquid state at room temperature. Only with completely liquid precursors any clogging in a flow reactor can be avoided.

In order to synthesis CdSe NPLs with completely liquid precursors, we thus need a cadmium source, a selenium source and a suitable solvent. The solvent of choice, for the synthesis of CdSe NPLs, is 1-octadecene (ODE) and is used by many groups.^{10,11,28,49,83–88} For the selenium source, pure selenium powder is often added to the synthesis.^{10,83–85} Sometimes, the selenium is dissolved in trioctylphosphine, which the group of Huang et al. used for their synthesis approach.⁸⁹ As most groups relied on pure selenium powder for synthesizing CdSe NPL,^{10,83–85} it also became a convenient choice to dissolve the selenium directly in ODE.⁹⁰ The selenium dissolved in ODE avoids the addition of another ligand into the system, thus rendering it a good fit for a liquid CdSe NPL synthesis.

With the selenium source found, the next step is finding a liquid cadmium source for the flow reactor. The challenge is even more obvious when reviewing other CdSe synthesis approaches in the literature: All syntheses methods from literature rely on at least one completely solid cadmium precursor and are thus unsuited for the flow reactor.^{10,11,28,49,86–88,91,92} One approach, for example by Riedinger et al.¹⁰ and Bigall et al.,⁸⁷ use cadmium acetate and cadmium myristate $\text{Cd}(\text{myr})_2$ for their CdSe NPL synthesis.^{28,86,92} This specific CdSe NPL synthesis approach also works when the $\text{Cd}(\text{myr})_2$ is replaced by cadmium stearate.¹¹ In a different second approach, only cadmium acetate $\text{Cd}(\text{OAc})_2$ is used without the usage of a long-chained cadmium carboxylate.^{88,91} Compared to the first approach, the second approach for synthesizing CdSe NPL takes hours instead of merely ten minutes. A third approach starts off with $\text{Cd}(\text{OAc})_2$ and combines it with pentanoic acid to produce cadmium pentanoate.⁴⁹

All three cadmium sources are unsuitable for the flow reactor because short-chained cadmium carboxylates are not soluble in the solvent ODE. Cadmium oleate can be synthesized from cadmium oxide, making it one cadmium source for the CdSe NPLs.⁹² However, as discussed thoroughly in Chapter 4.2.1, an additional short-chain carboxylate is needed for the synthesis of CdSe NPLs. One way to solve this problem is by dissolving the $\text{Cd}(\text{OAc})_2$ with an additional solvent, for example, methyl acetate.

To compare the success and the effects of the methyl acetate on the CdSe NPLs, Figure 16 showcases the results of the CdSe NPLs synthesis without adding methyl acetate. This synthesis results in 3 ML thick CdSe NPLs, based on the light-hole and heavy-hole peaks at 435 nm and 462 nm in the absorbance (Figure 16a), which is according to the literature.⁹³ Another indicator for CdSe NPLs is the full width at half maximum (FWHM) of these peaks. The light-hole at 435 nm has a FWHM value of 13 nm, the heavy-hole has a value of 9 nm. These values are similar to the results found in the literature.⁴⁶ Furthermore, the emission's peak is located at 463 nm, delivering another evidence of 3 ML CdSe NPLs (Figure 16a). This peak also corresponds to the literature.²² This peak's FWHM value is 8 nm, once again fitting the value found in the literature.⁹⁴ The TEM image in Figure 16b presents large CdSe NPLs with a length of $88 \text{ nm} \pm 22 \text{ nm}$ and width of $32 \text{ nm} \pm 9 \text{ nm}$, resulting in an area size of approximately $2834 \text{ nm}^2 \pm 1282 \text{ nm}^2$. Determining the size was difficult because of the rolled-up NPLs. Due to their large size, the CdSe NPLs in Figure 16b occasionally roll up, which was also observed in the literature.^{95,96} To highlight the problems when using $\text{Cd}(\text{OAc})_2$, one scale-up of the synthesis was attempted (Figure 16c). The large batch is not only extremely turbid, but the solid component is also precipitating after a few minutes. Furthermore, this suspension was centrifuged, and a solid residue of $\text{Cd}(\text{OAc})_2$ was left (Figure 16d).

Cd(OAc)₂ synthesis, without methyl acetate

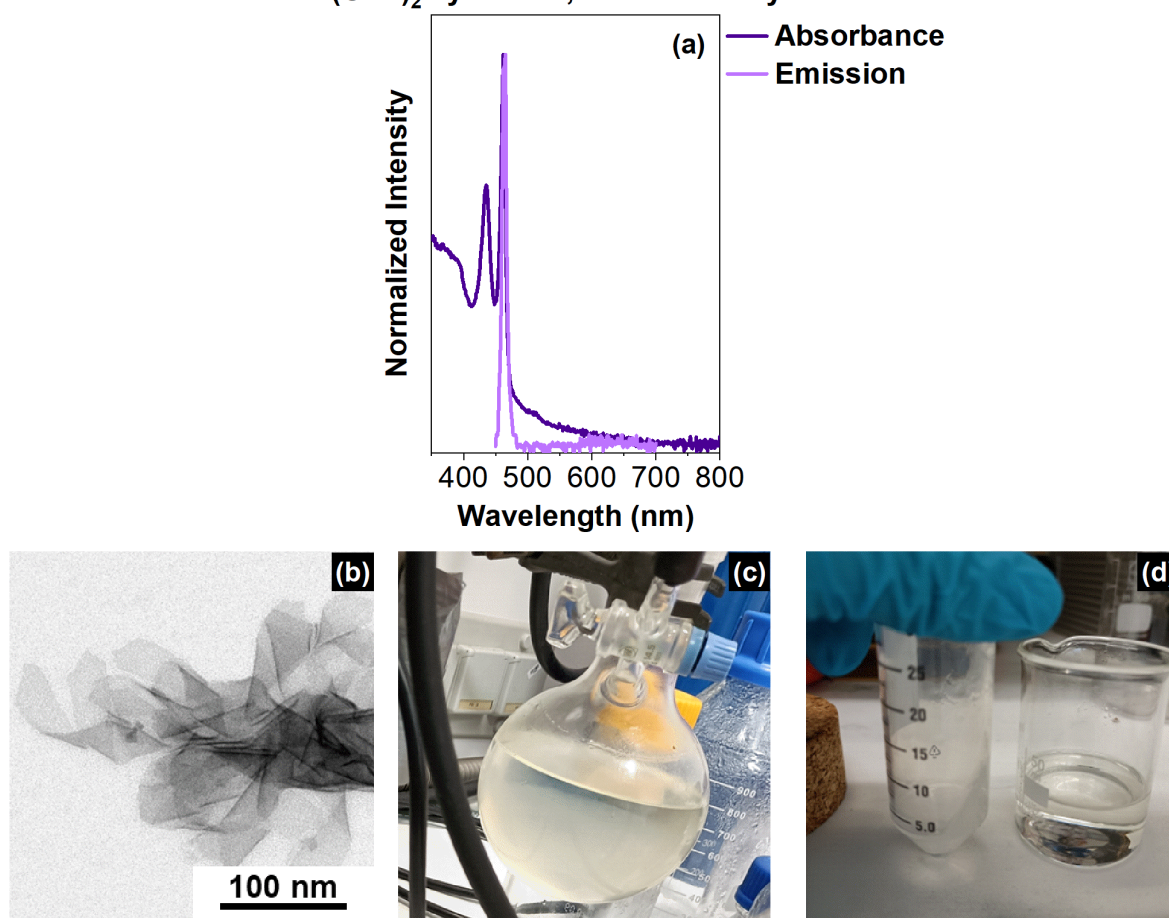


Figure 16: The CdSe NPL synthesis without the usage of methyl acetate. (a) showcases the absorbance and the emission of the purified CdSe NPLs. (b) showcases a TEM image of the CdSe NPLs. (c) and (d) showcase the insoluble Cd(OAc)₂ in a scale up (c) and then after centrifugation (d).

Figure 17 presents now the synthesis with the addition of methyl acetate. Similar to the synthesis without methyl acetate, we obtained 3 ML CdSe NPL based on their absorbance and emission (Figure 17a). Their FWHM values are once again between 8 to 13 nm. The TEM image of the CdSe NPLs also showcases very large NPLs, which roll up again (Figure 17b). Their length is $55 \text{ nm} \pm 14 \text{ nm}$, their width is $35 \text{ nm} \pm 10 \text{ nm}$, and their area size is roughly $1977 \text{ nm}^2 \pm 845 \text{ nm}^2$. Like the previous sample, the size determination was challenging as the NPLs rolled up and stacked. As a result, the methyl acetate added to the synthesis did not negatively impact the formation of the CdSe NPLs. However, adding methyl acetate did not dissolve the Cd(OAc)₂, as seen in Figure 17c. Other solvents like ethanol, acetone, and butanal were tested, as well. However, none of them dissolved the Cd(OAc)₂. In the end, the idea of trying to dissolve added Cd(OAc)₂ was not followed any further.

Cd(OAc)₂ synthesis, with methyl acetate

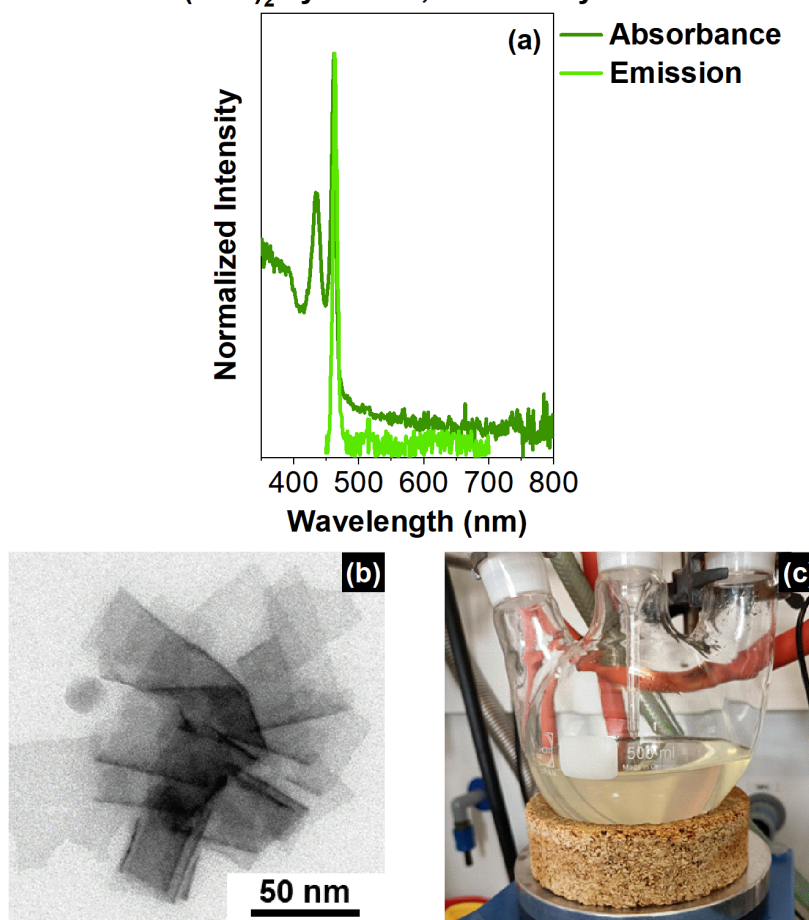


Figure 17: The CdSe NPL synthesis with the addition of methyl acetate. (a) showcases the absorbance and the emission of the purified CdSe NPLs. (b) showcases a TEM image of the CdSe NPLs. (c) is a photo of a scale-up attempt which turns turbid again.

The addition of Cd(OAc)₂ is not favorable for a CdSe NPLs flow reactor synthesis as this component is not soluble in the solvent used, which is ODE. However, a short-chained cadmium carboxylate is needed in order to synthesize CdSe NPLs. As a long-chained cadmium carboxylate is present in the synthesis with cadmium oleate, a short-chained carboxylate is still needed as a crucial component. Based on the synthesis in which pentanoic acid was added to produce cadmium pentanoate,⁴⁹ the new approach adds acetic acid, AcOH, to the synthesis. The addition of AcOH turns the present cadmium oleate *in situ* to Cd(OAc)₂. In this new approach, the amount of AcOH was twice the cadmium oxide amount in the synthesis, which equals 0.6 mmol of AcOH. These synthesis results can be seen in Figure 18. Once again, 3 ML CdSe NPLs resulted based on the absorbance and emission in Figure 18a. The TEM image in Figure 18b reveals CdSe NPLs with a length of 87 nm ± 24 nm and a width of 19 nm ± 6 nm, resulting in an area size of 1677 nm² ± 891 nm². While these results are promising, sadly, the precursor

solution immediately turned into a turbid suspension after the AcOH was added. However, the new approach can be further improved by adjusting the amount of AcOH.

0.6 mmol AcOH synthesis, without Cd(OAc)₂

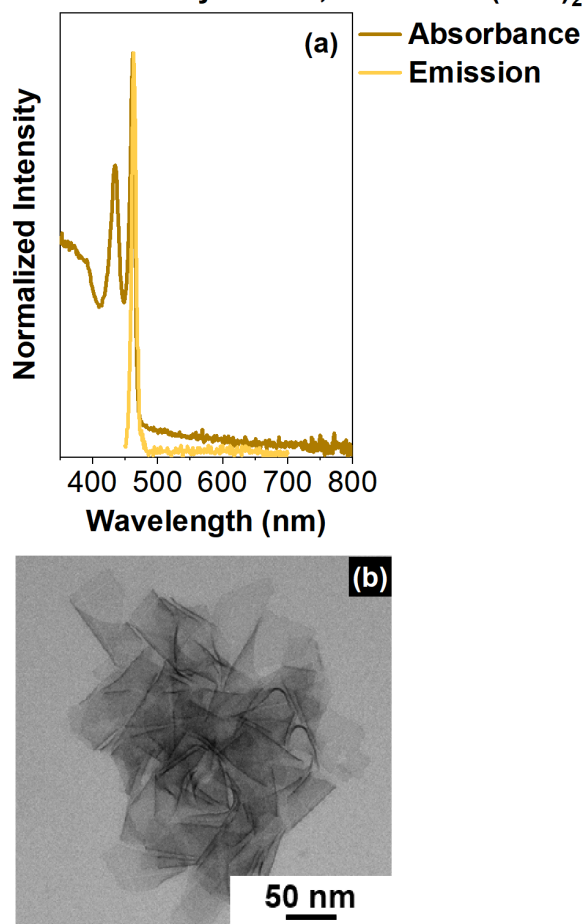


Figure 18: The CdSe NPL synthesis with 0.6 mmol AcOH. (a) shows the absorbance and the emission of the purified NPLs and (b) shows a TEM image of the purified CdSe NPLs.

The amount of AcOH can be lowered to match the amount of Se in the synthesis, which is 0.2 mmol. Through the lower amount of AcOH, the formation of a high amount of Cd(OAc)₂ can be avoided. In Figure 19 are the results when using 0.2 mmol of Cd(OAc)₂. Similar to the previous approaches, mainly 3 ML CdSe NPLs have formed with their light-hole and heavy-hole peaks at 435 nm and 462 nm in the absorbance and a sharp emission peak at 463 nm (Figure 19a). The FWHM values are once again for the absorption 13 nm and 9 nm, while the FWHM value for the emission is 8 nm. Interestingly, a double peak at 372 nm and 393 nm is visible in the absorption, as well as another additional peak at 513 nm. According to the literature, this double peak can be attributed to 2 ML thick CdSe NPLs.⁹¹ The other peak, at 513 nm, is likely arising from a 4 ML thick CdSe NPL population.^{28,91} This can be further supported by the additional peak in the emission at 514 nm.^{28,91} Figure 19b shows a TEM image of the CdSe

NPLs. In comparison to the previous attempts, the platelets are remarkably smaller. The CdSe NPLs lengths are on average $58 \text{ nm} \pm 20 \text{ nm}$, and their width is $16 \text{ nm} \pm 5 \text{ nm}$. As a result, their area size is $955 \text{ nm}^2 \pm 534 \text{ nm}^2$, which is smaller than the CdSe NPLs area sizes from the previous synthesis approaches. The most important question is whether the lower amount of AcOH leads to a complete liquid synthesis precursor at room temperature or not. Fortunately, the synthesis is completely liquid at room temperature and even when a scale-up is performed, as seen in Figure 19c.

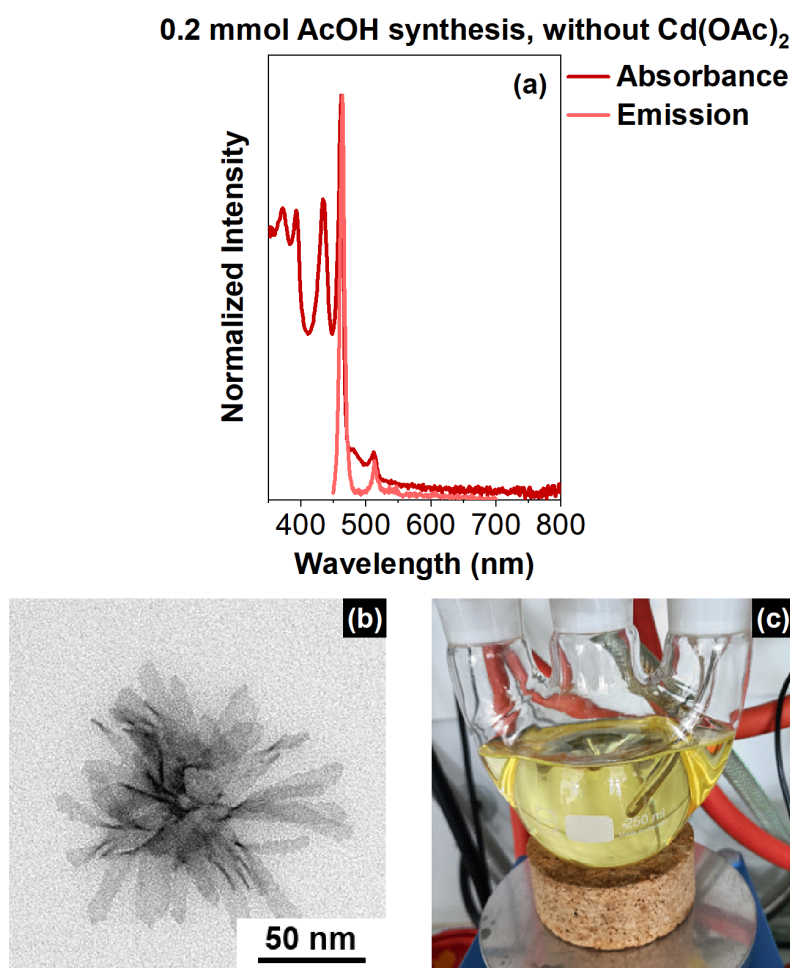


Figure 19: The CdSe NPL synthesis with 0.2 mmol AcOH. (a) shows the absorbance and the emission of the purified NPLs, and (b) shows a TEM image of the purified CdSe NPLs. In (c) is a scale-up of the unreacted precursor solution. Photo used with permission from Funk et al. under creative common license.⁹⁷

To compare all four synthesis approaches so far, Figure 20 showcases the fluorescence decays. Furthermore, Table 1 summarizes their area sizes, their intensity-weighted fluorescence lifetimes (FLT), and quantum yields (QY). The QY was determined indirectly with Coumarin 153 as a reference (see Chapter 4.3.1.2). As expected, similar to the results found in the literature, the synthesized CdSe NPLs exhibit short FLT of a few nanoseconds.^{98,99} Furthermore, all

synthesized CdSe NPLs have very low QYs of less than 1 %. The low QY can be explained by the large sizes of the CdSe NPLs, which have more defects than smaller CdSe NPLs.^{29,98}

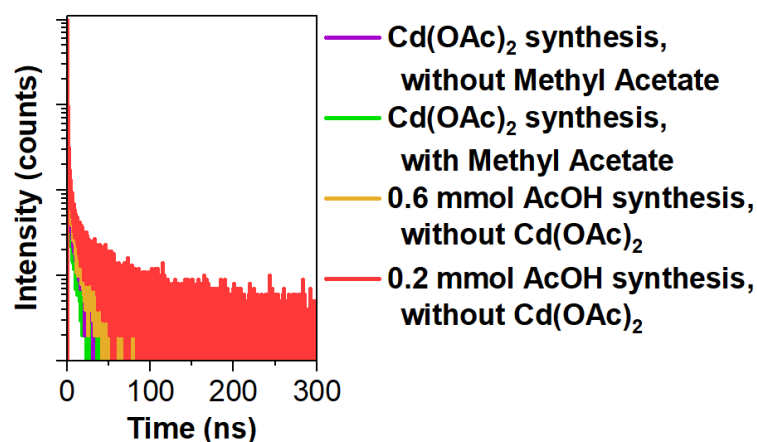


Figure 20: The fluorescence decay for all four synthesis approaches without and with methyl acetate, as well as with 0.6 mmol and 0.2 mmol AcOH.

Table 1: Area sizes, intensity-weighted fluorescence lifetimes and quantum yields for all for synthesis approaches.

Synthesis approach	Area size [nm ²]	FLT [ns]	QY [%]
Cd(OAc) ₂ synthesis, without Methyl Acetate.	2834 ± 1282	1.9	<1
Cd(OAc) ₂ synthesis, with Methyl Acetate.	1977 ± 845	1.5	<1
0.6 mmol AcOH synthesis	1677 ± 891	2.2	<1
0.2 mmol AcOH synthesis	955 ± 534	3.6	<1

It should be noted that the precursor solution does not form a precipitate not only when a scale-up is performed but also when the precursor is more concentrated by reducing the amount of the solvent ODE by half. With a successful scale-up, this synthesis approach is not only suitable for the flow reactor but makes it possible for these CdSe NPLs to be accessible for multiple applications through mass production. This precursor is stable for a long time as long as the AcOH is not added. Once the AcOH has been added, the liquid precursor should be used up shortly, as the precursor is not stable long-term with AcOH in it. As mentioned above, Cd(OAc)₂ is still forming in the precursor. The more time passes, the more Cd(OAc)₂ is

forming. Figure 21 shows the flow reactor suitable precursor, with 0.2 mmol AcOH, after four days have passed.

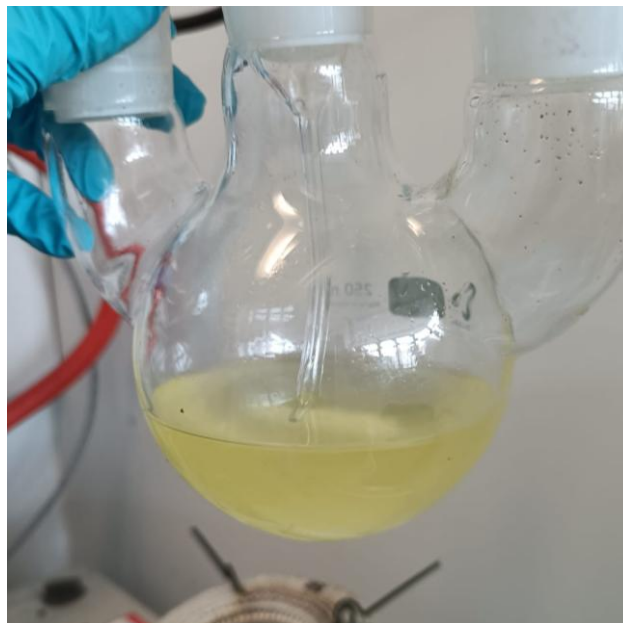


Figure 21: A CdSe NPL precursor with 0.2 mmol AcOH after 4 days have passed. The once clear solution has turned into a yellow, turbid suspension. Photo used with permission from Funk et al. under creative common license.⁹⁷

This turbid precursor in Figure 21 demonstrates that while the flow reactor suitable precursor has a high potential for mass-producing CdSe NPLs, it has its flaws with its missing long-term stability. However, this flaw poses no hindrance to mass production. The AcOH can be added to bigger batches, which are then consumed right away in an industrial flow reactor. To summarize, a suitable flow reactor synthesis has been found with AcOH as a crucial precursor component.

6.2 Flow reactor synthesis of CdSe NPL

As suitable and liquid precursors are found, a flow reactor synthesis is finally possible. The entire flow reactor setup (Figure 22a), including a close-up of the syringe pumps filled with the flow reactor precursor (Figure 22b), can be found in Figure 22.

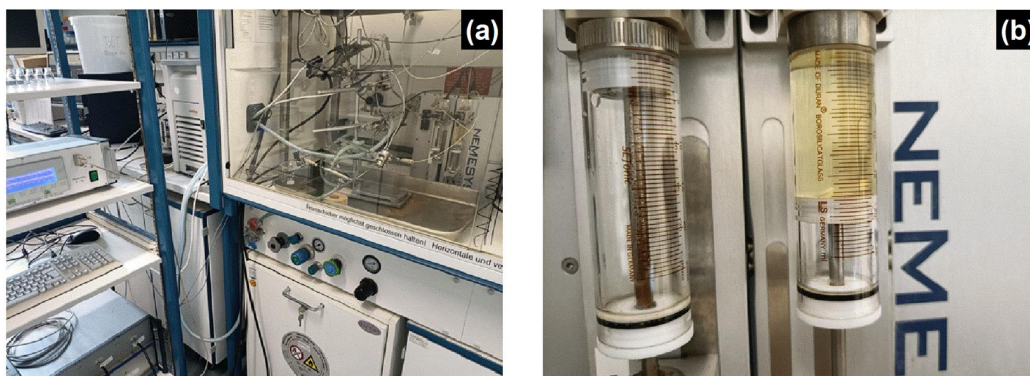


Figure 22: Photos of the flow reactor setup. (a) shows the entire flow reactor setup, including parts of the temperature controller and the UV/Vis spectrometer. (b) shows a close look at the syringe pumps filled with the reactor precursor.

Through syringe pumps, the flow rate can be controlled precisely. In this regard, it is necessary to know the flow profile in the reactor, as this can greatly affect the synthesis conditions. One method to calculate the flow profile is through the Reynolds number Re . As 1/16-inch PEEK tubes are used for the flow reactor, the characteristic length is $1.0 \cdot 10^{-3}$ m. The kinematic viscosity of ODE is $3.6 \cdot 10^{-6} \text{ m}^2 \cdot \text{s}^{-1}$. With these given values and using the highest possible flow rate for this setup, which is $7.3 \cdot 10^{-2} \text{ m} \cdot \text{s}^{-1}$, the following Reynolds number is obtained:

$$Re = \frac{1.0 \cdot 10^{-3} \text{ m} \cdot 3.6 \cdot 10^{-6} \text{ m}^2 \cdot \text{s}^{-1}}{7.3 \cdot 10^{-2} \text{ m} \cdot \text{s}^{-1}} = 20.$$

This obtained value is below 2300; thus, the flow reactor synthesis is likely in a laminar flow regime.^{54,55,60} Considering the setup can be described as a microreactor, the obtained Reynolds number is also below the value of 500, which once again describes laminar flow.⁶⁰ As the Reynolds number depends on the flow diameter, changing the ovens does not change the Reynolds number obtained.

The tracer method was used next to get conclusive results about the flow regime. In Figure 23 are the results of these residence time distribution experiments for the different ovens. To act as a reference, the ideal turbulent flow and ideal laminar flow residence time distribution are present in the graphs. As expected from the previous Reynolds number results, none of these graphs showcase a turbulent flow regime. The 5 m oven (Figure 23a) showcases a more turbulent behavior compared to the 90 cm oven (Figure 23b). Moreover, the 90 cm is more turbulent than the 30 cm oven (Figure 23c). This trend, which is that a shorter length of the overall flow reactor system leads to a more laminar flow profile, was already visible in the Reynolds numbers from before. Consequently, these results are within expectations.

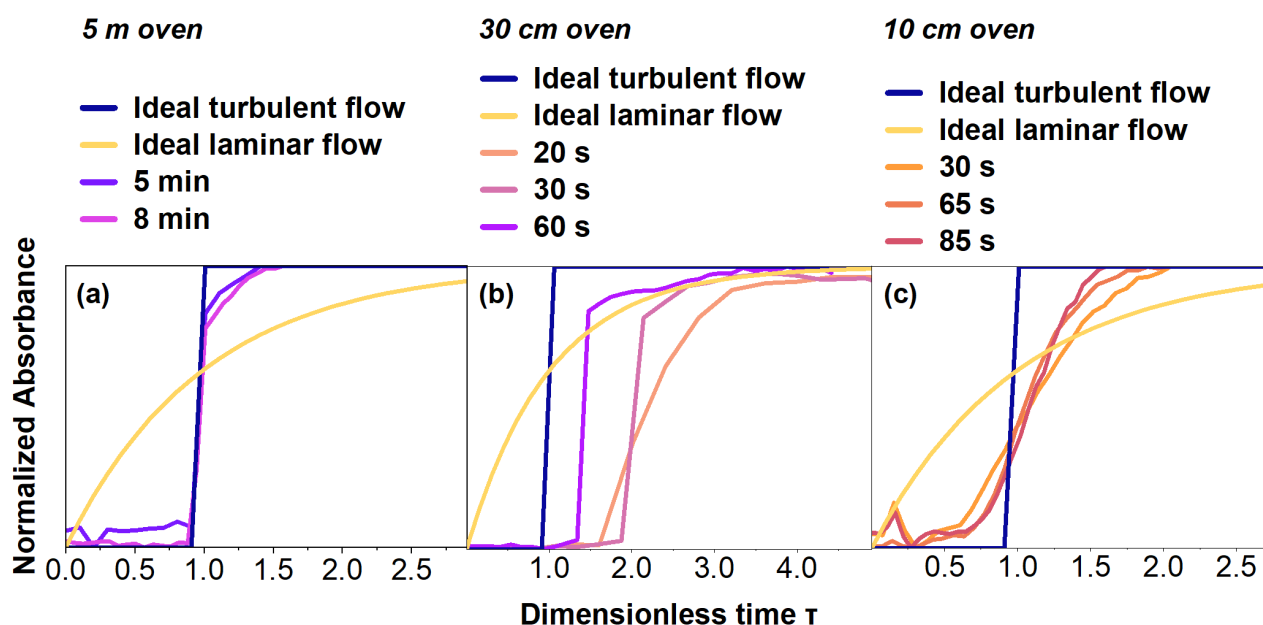


Figure 23: Residence time distribution experiments for different reactor oven lengths in order to determine the flow profile. The flow profile for the 5 m oven is in (a), for the 30 cm oven in (b), and for the 10 cm oven in (c). Figure by Funk et al. with slight modifications used with permission and under creative common license.⁹⁷

With the flow profiles now available, the CdSe NPLs synthesis can be carried out in the flow reactor. In order to get further details on the growth mechanism, it is important to know the nucleation temperature. The 5 m oven was chosen for this in order to realize longer synthesis times, similar to the reaction times in a flask synthesis. Additionally, the flow rate was adjusted so that the synthesis time, specifically the time the precursor solution was heated, for these experiments was always 6 minutes.

Figure 24 shows the normalized absorbance and emission spectra, including the non-normalized emission. At low temperatures, between 130 to 160 °C, there is no notable peak in the absorbance (Figure 24a) or emission (Figure 24b) present, which indicates the formation of any

CdSe NPLs. Starting at 170 °C, the emission's intensity decreases, but there is still no peak available that belongs to CdSe NPLs. Once the temperature reaches 180 °C, a small peak at 461 nm appears. This peak shifts to 463 nm at 210 °C and includes the appearance of the 435 nm and 462 nm double peak in the absorbance, typical for the 3 ML CdSe NPLs. The shift can likely be explained by the lateral size of the CdSe NPLs. At 180 °C, the CdSe NPLs are most probably smaller than at 210 °C. As a result, the exciton is less confined in a CdSe NPL with large lateral dimensions than a CdSe NPL with small lateral dimensions.¹⁰⁰ Aside from this small Stokes-shift, the nucleation temperature for the CdSe NPLs in the flow reactor is at 180 °C. In the literature, the nucleation of CdSe NPLs was found at temperatures of at least 170 °C²⁷ and higher.¹⁰¹ Taking the literature into account,^{27,101} the found nucleation temperature in the flow reactor fits into these results, as well.

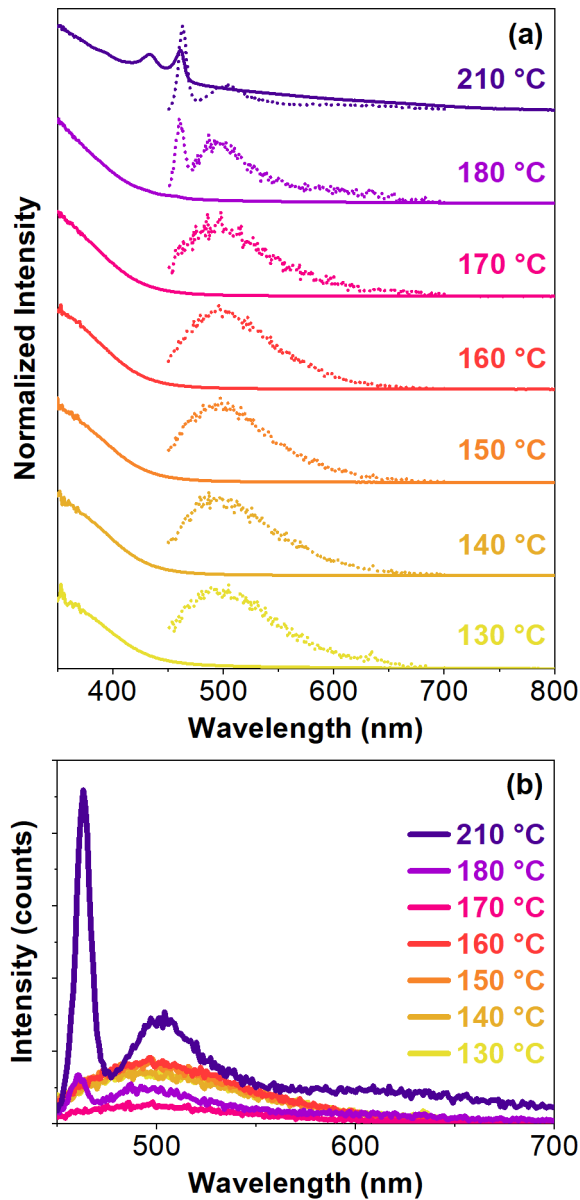


Figure 24: Normalized absorbance and emission spectra of flow reactor samples with a fixed synthesis time of 6 min, conducted at different temperatures. Figure by Funk et al. with slight modifications used with permission and under creative common license.⁹⁷

In conclusion, the flow reactor exhibits a laminar flow profile for all available ovens. Furthermore, the nucleation temperature for the CdSe NPL is found at 180 °C.

6.2.1 The correlation between MSCs and NPL

The earliest stages of CdSe NPL synthesis can be easily accessed in the flow reactor in order to obtain information on their growth. To synthesize these early stages, the 10 cm oven was used to keep the residence time in the oven to as low as 5 seconds. Figure 25 shows these early stages for different temperatures. It becomes apparent that in the first 15 seconds (s) at 210 °C, the Precursor remains unchanged (Figure 25a). Starting at 220 °C, the precursor is slightly decreasing in its intensity with a residence time of 15 s (Figure 25b). This decrease is more pronounced at 230 °C and 15 s (Figure 25c). At 240 °C, the synthesis was observed between 5 s to 30 s (Figure 25d). When the residence is increased, the absorbance is once again decreasing. This decrease implies that the precursor is being consumed. In the spectrum, however, it is unclear what the precursor is being consumed for as there is no peak visible, which could hint towards a certain nanostructure. Hence, in order to see what the precursor is consumed for, longer residence times are needed until a peak is visible. Therefore, in order to have a chance to see a potential pre-structure prior to the CdSe NPLs, temperatures lower than 240 °C are more favorable.

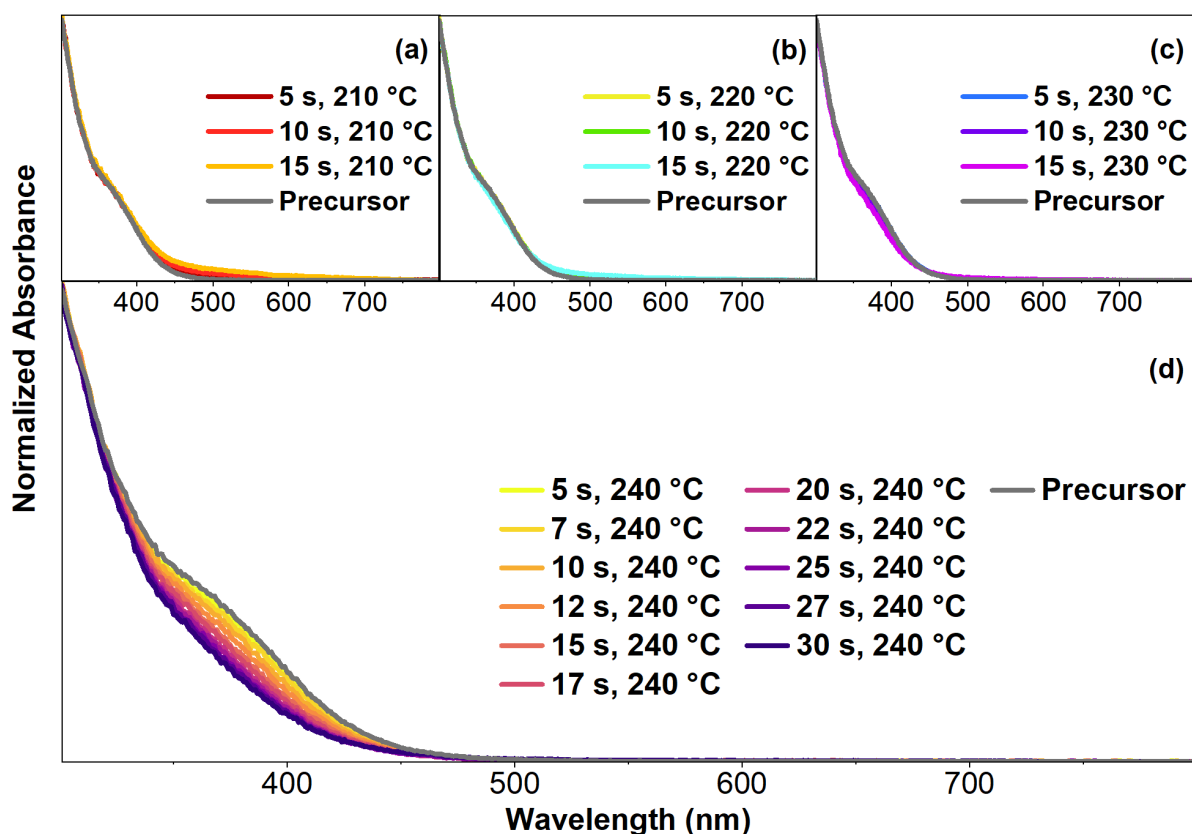


Figure 25: Normalized absorbance of the CdSe NPLs synthesis performed at reaction times of under one minute in a 10 cm oven. (a) shows the first 5 to 15 seconds at 210 °C, (b) the first 5 to 15 seconds at 220 °C, and (c) the first 5 to 15 seconds at 230 °C. (d) shows the first 5 to 30 seconds at 240 °C. The unreacted precursor is shown in grey.

Consequently, residence times between 50 s to 85 s were tested with a temperature of 210 °C. Figure 26 showcases these results. At 210 °C, a peak at 360 nm is visible for a residence time of 50 s (Figure 26a). By increasing the residence time further to 55 s and 60 s, this peak increases in its intensity until the maximum intensity is reached at a residence time of 70 s. At a higher residence time of 75 s, the intensity starts to decrease. The trend of the decreasing intensity continues for the following residence times of 70 s and 85 s. Compared to the previous results, a pre-structure as indeed formed with this absorbance peak at 360 nm. The peak cannot originate from 2 ML thick CdSe NPLs as they have their distinct peaks at 372 nm and 393 nm.⁹¹ Judging the position of the peak, this pre-structure has to be smaller than 2 nm. Nanostructures with a size lower than 2 nm are commonly associated with magic-size clusters (MSCs).⁵² These MSCs can be assigned to a so-called MSC-family based on their absorption maximum.¹⁰² As a result, the MSCs observed in Figure 26 are CdSe-360 MSCs.

Based solely on the peak's position, certain MSC structures come to mind. Popular examples are the stoichiometric (CdSe)₁₃ and (CdSe)₃₄ MSCs. In the case of (CdSe)₁₃, a double peak at approximately 360 nm and 330 nm is expected,^{103,104} while for (CdSe)₃₄ the double peak would appear at approximately 360 nm and 405 nm.¹⁰⁴⁻¹⁰⁸ However, there are a few problems with this assignment approach.

First of all, it is difficult to determine the exact composition and structure of CdSe MSCs, especially based on these absorption spectra alone.¹⁰⁹ Additionally, the synthesis condition in the flow reaction needs to be considered. Oleic acid and acetic acid are used, which are both carboxylate ligands. As reported by other groups, carboxylate ligands favor the formation of non-stoichiometric MSC structures.¹¹⁰⁻¹¹² So, if the MSCs need to be assigned to a structure, they are most likely non-stoichiometric, tetrahedral shaped based on the synthesis conditions in the flow reactor.

Nevertheless, this peak confirms the presence of CdSe MSCs. Moreover, the decreasing starting intensity at 70 s and 210 °C indicates that the formed MSCs are used for a new step within the synthesis of CdSe NPLs.

At 240 °C and 50 s, the previously visible absorbance peak at 360 nm is now more shoulder-like (Figure 26b). The intensity increases for 55 s and 60 s. Starting at 65 s; however, the intensity of this shoulder-like structure decreases again until 85 s. Similar to the observation above, this decrease indicates that the as-formed MSCs are being consumed for a different process.

Additionally, this different process is more favored at higher temperatures of 240 °C, which is strongly suggested by the lower intensity of their absorbance.

To make the trends more obvious, the absorbance at 360 nm is plotted against the reaction time from the experiments performed at 210 °C and 240 °C in Figure 27. This confirms the trends that have already been observed in Figure 26. Furthermore, it shows that at 210 °C and 65 s, the absorbance is lower compared to the other absorbances at 60 s and 70 s. Except for this discordant value at 65 s, the general trend for 210 °C remains the same as previously stated.

Even higher temperatures, at 300 °C and a reaction time of 50 s, showcase no absorbance peak at 360 nm (Figure 26c). Instead, very small peaks at 435 nm, 463 nm, 481 nm, and 513 nm are visible in this specific spectrum. According to the literature, the first peaks at 435 nm and 463 nm belong to 3 ML thick CdSe NPL,⁹³ whereas the other peaks at 481 nm and 513 nm arise from 4 ML CdSe NPL.^{28,91} The intensity of these four peaks increases with increasing residence times. Hence, the maximum intensity is reached at 300 °C and a residence time of 85 s for this experiment. It is important to note that under these specific conditions, with temperatures as high as 300 °C, no NPLs would form as an isotropic growth would be expected.¹⁰ The spectra in Figure 26c are steep, indicating that nanodots as a side-product have formed, as well. An explanation for these results lies in the flow reactor itself, as it exhibits a laminar flow profile. The heat is distributed more evenly in a turbulent flow profile compared to a laminar flow.⁶¹ Consequently, the observed CdSe NPLs at 300 °C indicate that the laminar flow profile affects the synthesis conditions for the CdSe NPLs.

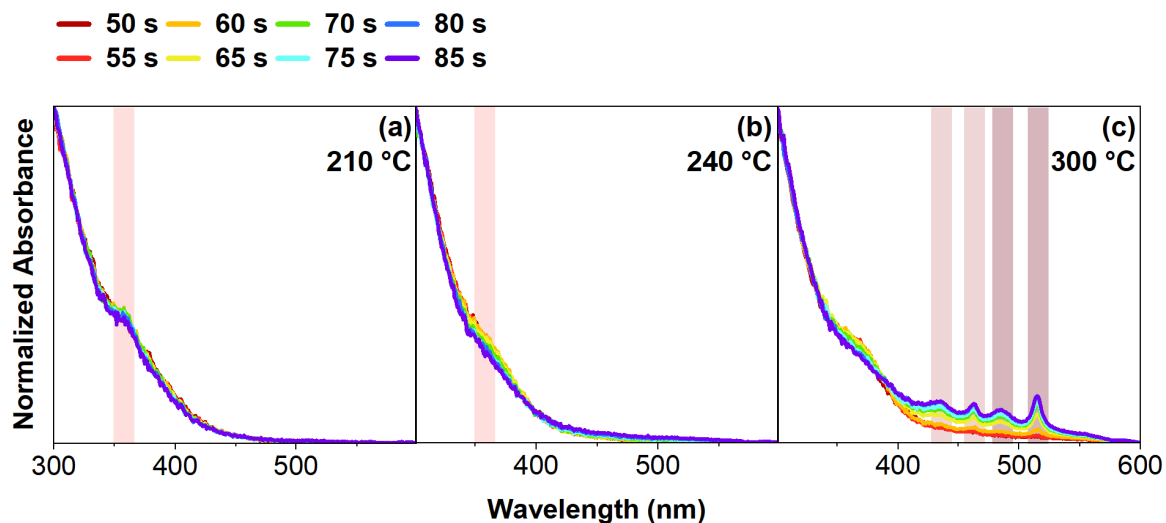


Figure 26: Normalized absorbance of the CdSe NPLs synthesis performed at reaction times of around one minute in a 10 cm oven. (a) shows various residence times conducted at 210 °C. The peak at 360 nm is marked in a light salmon color, which belongs to CdSe MSCs. (b) shows the various residence times at 240 °C, also with the light salmon color marking. (c) showcases the different reactions conducted at 300 °C. The double peaks of the 3 ML CdSe NPLs are marked in a pale pink color, and the peaks of the 4 ML CdSe NPLs are marked in a dark pink color. Figure by Funk et al. with slight modifications used with permission and under creative common license.⁹⁷

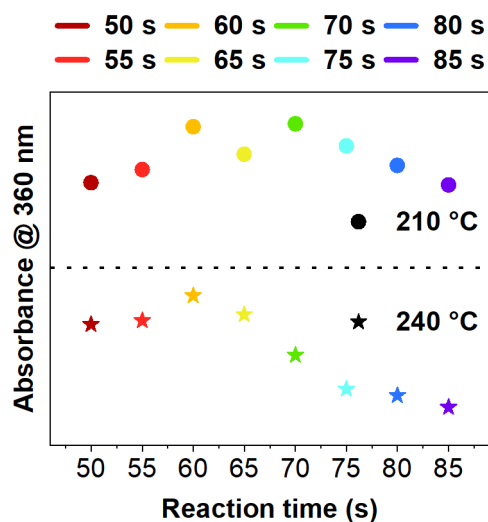


Figure 27: Corresponding absorbance at 360 nm plotted against the Reaction time for the CdSe NPLs synthesis performed at reaction times of around one minute in a 10 cm oven (from Figure 26).

In literature, the synthesis of CdSe MCSs is conducted at room temperature¹⁰³ or at temperatures as low as 0 °C.¹⁰⁶ If CdSe MSCs are forming prior to the formation of CdSe NPLs, then an aged precursor would increase the absorbance intensity at 360 nm of these CdSe-360 MSCs, as CdSe MSCs would have formed from the aging process at room temperature. So, the same precursor from the experiments in Figure 26 had aged for 4 days, and the experiment was repeated. Figure 28 shows the results of using an aged precursor.

At 210 °C and 50 s (Figure 28a), there is an absorption peak at 360 nm, like the previous results. Once again, the peak's intensity increases by increasing the residence time. The peak's maximum intensity is at 65 s, which is slightly different from the previous experiment, where the peak's maximum was reached at 70 s. By increasing the residence time in the oven further to 70 s, the peak at 360 nm decreases. The decrease continues until the final residence time of 85 s is reached. In comparison to the previous attempt, the peak at 360 nm is more pronounced. Moreover, the peak's intensity at 65 s and 210 °C is higher for the aged precursor than for the non-aged precursor. This observation proves that this peak does indeed belong to CdSe MSCs.

Higher temperatures of 240 °C (Figure 28b) show that the shoulder from before now exhibits a tiny peak at 360 nm. At 55 s, the peak's intensity increases; another increase is visible at 60 s, which is also the maximum. The peak is then followed by a decrease at 65 s. Once again, the minimum value is reached at 85 s. This experiment proves again that the peak must arise from CdSe MSCs. Especially with the previous experiment where the peak was not as visible, the more prominent peak shows that despite the higher temperatures of 240°C, the MSCs are present in the synthesis before they are used for a different process.

Once again, to make the stated trends clearer, the absorbance at 360 nm is plotted against the reaction time for the experiments conducted at 210 °C and 240 °C in Figure 29. It becomes apparent that at 210 °C and 75 s, the absorbance decreased way more than the other experiments. However, the general trend remains the same.

Similar to the previous experiment, the reaction at 50 s and 300 °C showcases 3 ML and 4 ML thick CdSe NPLs based on the absorption peaks at 435 nm, 463 nm, 481 nm, and 513 nm (Figure 28c). Once again, the peaks have their highest intensity for the longest residence time, which is 85 s. Both experiments thus showcase that CdSe MSCs are indeed forming prior to the formation of CdSe NPLs.

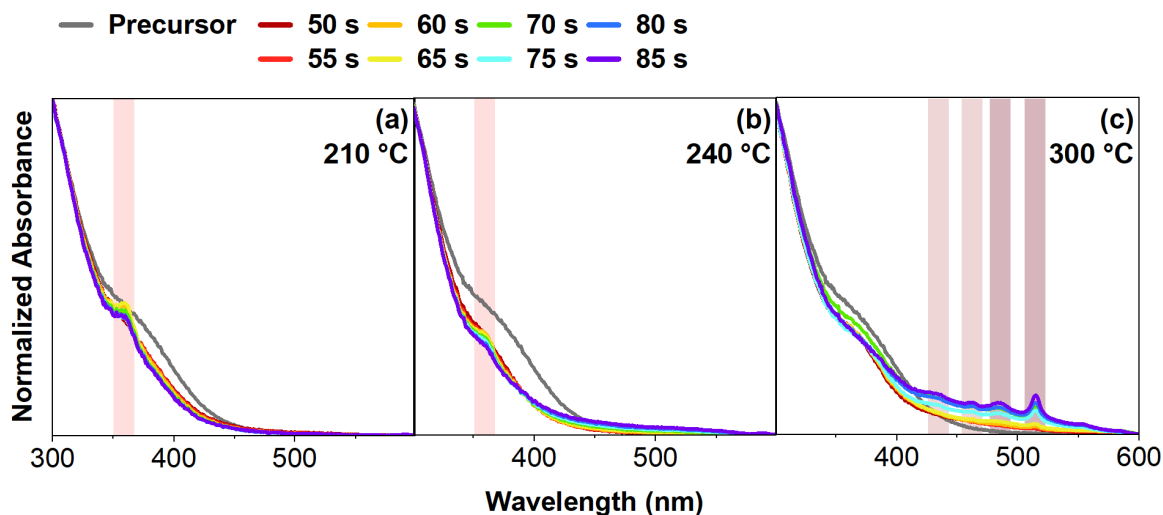


Figure 28: Normalized absorbance of the CdSe NPLs synthesis performed at reaction times of around one minute in a 10 cm oven using a 4-day old precursor solution. (a) shows the results conducted at 210 °C, (b) at 240 °C, and (c) at 300 °C. The light salmon color marks the peak position for the CdSe MSCs, the pale pink color for 3 ML CdSe NPLs, and the dark pink color for 4 ML CdSe NPLs. Figure by Funk et al. with slight modifications used with permission and under creative common license.⁹⁷

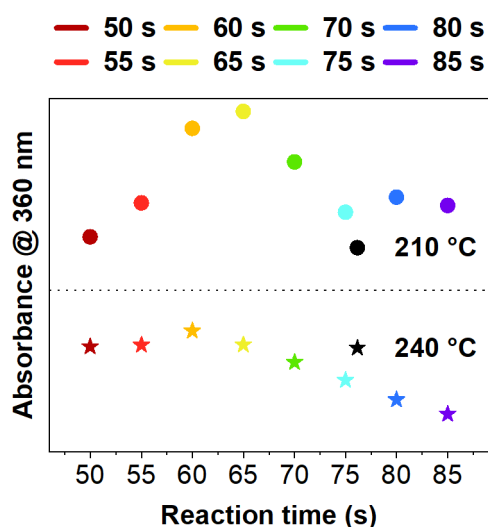


Figure 29: Corresponding absorbance at 360 nm plotted against the Reaction time for the CdSe NPLs synthesis performed at reaction times of around one minute in a 10 cm oven (from Figure 26).

With the confirmed presence of CdSe MSCs, photoluminescence excitation (PLE) is used as one method to determine the cluster size of these CdSe MSCs. Figure 30 shows PLE spectra for two experiments performed in the flow reactor with different oven lengths. For the PLE measurements, the emission was set to 463 nm, which is the value of the heavy-hole absorption peak for the 3 ML CdSe NPLs.

The first experiment starts at 210 °C and 60 s in a 10 cm oven (Figure 30a). Compared to the unreacted Precursor in grey, the spectrum shows a peak at 413 nm. Another slightly higher intensity can be assumed at approximately 365 nm. In the context of the previous absorbance measurements, the PLE peak at 413 nm strongly indicates that another CdSe MSC family is forming, likely corresponding to CdSe-413. This is a common observation, as other groups reported the formation of multiple CdSe MSCs families at the same time in one synthesis.^{102,113} Furthermore, the PLE spectra of the precursor and this experiment prove that CdSe MSCs form during the synthesis of the NPLs and are not present in the unreacted precursor. A temperature increase to 225 °C leads to a remarkable blue-shift in the PLE spectrum from 413 nm to 405 nm. Another increase in temperature to 240 °C doesn't impact the spectrum this much; the shift is, this time, around 1-2 nm at most. Slight shifts in the wavelength might be caused by the ligands on the CdSe MSCs surfaces as the flow reactor synthesis contains two different ligands with oleic acid and acetic acid.^{107,108} It should be noted here, that bigger shifts were reported based on the ligand influence, as well.^{107,108} It was also reported that carboxylate may cause etching of the CdSe MSCs, which results in a minimal blue shift.¹⁰⁹ Based on these reports, the very small shifts observed by 1-2 nm might be a result of the CdSe MSCs slightly decreasing in size.

The big shift between 413 nm and 405 nm, however, more likely arises from the ligands, as bigger shifts are influenced by ligands, as well.¹¹⁴ Additionally, oleic acid and acetic acid are reported to exhibit CdSe MSCs whose absorption maximum is in the range between 413 nm and 405 nm, as well.¹⁰⁹ If the shape of these CdSe MSCs is also considered here, Schnitzenbaumer et al. and Yang et al. reported tetrahedral CdSe MSCs with an absorption maximum of approximately 405 nm.^{115,116} As a result, there is a possibility that both the CdSe-413 and CdSe-405 are the same CdSe-MSC family. To outline the possibility that CdSe-413 and CdSe-405 are the same species, further experiments are needed.

Switching to a 30 cm oven without changing the temperature (240 °C) or residence time (60 s) leads to another small shift. Another small shift can be observed by increasing the residence time in the 30 cm oven to 70 s and 80 s, respectively. Once the residence time is increased to

90 s at 240 °C, not only another blue-shift but also a small peak at 435 nm appears, corresponding to the 3 ML CdSe NPLs.⁹³ The intensity of this peak rises when the residence time is further increased to 120 s at 240 °C, further confirming that this peak certainly belongs to the 3 ML CdSe NPLs.

Figure 30b shows another experiment for reproducibility, this time with an unchanging oven length of 90 cm. The precursor exhibits no peak, while at 200 °C and 20 s, a peak at 405 nm has formed, which corresponds to the CdSe-405 MSCs. This observation supports the previous discussion that the CdSe-413 and CdSe-405 may be the same cluster species. As CdSe-405 MSCs are observed here and have been observed in other reports, the possibility is high that the CdSe MSCs family is likely CdSe-405.^{115,116} Aside from this theory, the observation proves once again that CdSe MSCs form during the synthesis of CdSe NPLs and are not present from the beginning in the precursor.

By increasing the residence time to 40 s and then to 60 s at 200 °C, a very small blue-shift is visible again. This blue-shift continues when the temperature is increased to 210 °C. A further blue-shift is observed when the temperature is increased to 220 °C. Similar to the previous experiment, at 230 °C and 60 s, there is a new peak appearing at 435 nm, and another blue-shift is observed. This peak belongs to the 3 ML CdSe NPLs. By increasing the temperature to 240 °C, the PLE intensity at 435 nm increased, this time without being accompanied by a blue-shift in the region below 400 nm. The intensity at 435 nm is further increased at 240 °C and 120 s, implying that with longer residence times, more 3 ML CdSe NPLs have formed.

Based on the experiments, CdSe-360 and CdSe-405 are determined. Moreover, the blue shift observed throughout the experiment strongly implies that the CdSe MSCs undergo an additional process, through an intermediate, before CdSe NPLs form. This intermediate structure is likely smaller than the CdSe MSCs as seen in the small blue-shifts in the PLE spectra.

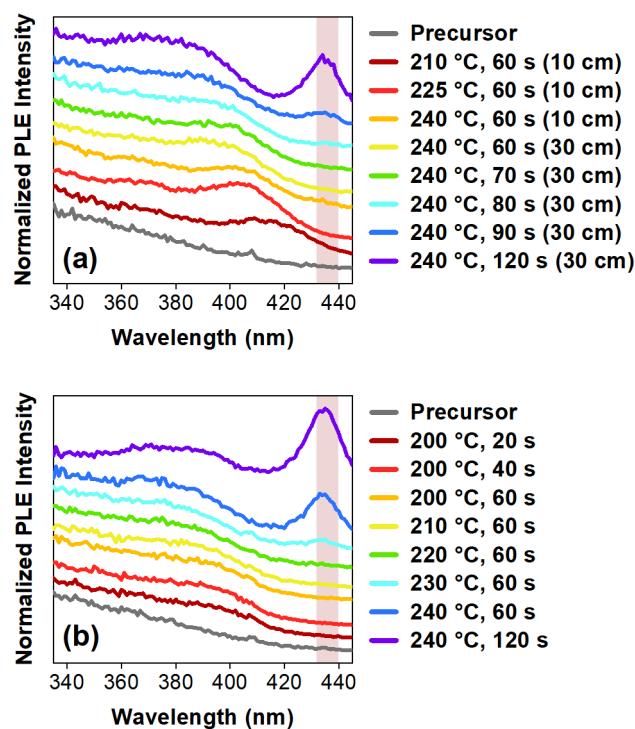


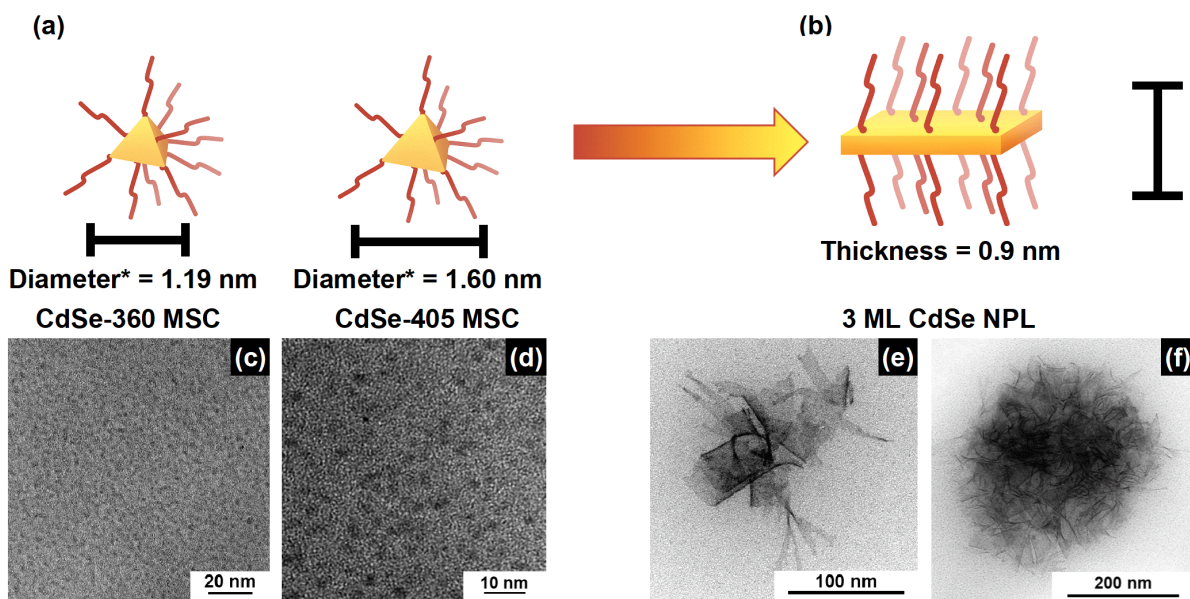
Figure 30: Normalized PLE spectra for two flow reactor experiments with an emission set at 463 nm. (a) shows PLE spectra for increasing temperatures, then for increasing residence times performed in two ovens with a length of 10 cm and 30 cm. (b) presents the results for increasing residence times, then increasing temperature performed in a 90 cm oven. The pale pink color marks the position for the light-hole peak corresponding to 3 ML CdSe NPLs. Figure by Funk et al. with slight modifications used with permission and under creative common license.⁹⁷

To explain the likelihood that the intermediate structure from the PLE spectra is smaller than the CdSe MSCs observed, the size of the CdSe MSCs is needed. One method to determine the size of spherical CdSe clusters based on their absorption maximum has been developed by Yu et al.¹¹⁷ As the CdSe MSCs in the flow reactor are likely non-stoichiometric,¹¹⁰⁻¹¹² a spherical shape was assumed for calculating a theoretical diameter for the CdSe MSCs observed in the CdSe NPL synthesis. With this assumption made, CdSe-360 MSCs approximately have a diameter of 1.19 nm and CdSe-405 MSCs of 1.60 nm (Figure 31a). If we assume CdSe-413 is a different family to CdSe-405, their diameter would be 1.67 nm. As the CdSe MSCs are non-stoichiometric, their actual diameter is expected to be larger. The calculated diameters for all CdSe MSCs are larger than the 3 ML CdSe NPL with their thickness of 0.9 nm (Figure 31b).⁴⁴

Regarding this size difference, the intermediate structure has to connect these two structures so that its size probably fits between these structures. Peng et al. already proposed such an intermediate structure in their CdSe NPL growth theory.¹¹ According to their theory, the CdSe seeds they used transformed into a two-dimensional embryo through an intra-particle ripening

process.¹¹ It is, therefore, reasonable to assume that this proposed two-dimensional embryo is the structure in question that connects the MSCs (Figure 31a) to the CdSe NPLs (Figure 31b). Further evidence of CdSe MSCs being present in the CdSe NPLs synthesis can be found in the TEM images of the unpurified reactor product in Figure 31c and Figure 29d. At 200 °C and 40 s, the spherical CdSe nanoparticles observed have a size of 2.1 ± 0.4 nm. The size is within the range of CdSe MSCs, proving once more that CdSe MSCs have indeed formed prior to the CdSe NPLs. Figure 31e and Figure 31f both show crude flow reactor products of CdSe NPLs (240 °C, 120 s). Based on Figures 31e and 31f, the as-produced CdSe NPLs have varying lateral sizes. The width of the depicted CdSe NPL is 25 ± 19 nm, with a length of 75 ± 26 nm. As a result, the lateral size of the CdSe NPLs is approximately 2066 ± 2110 nm. As shown in Figures 31e and 31f, the CdSe NPLs are so large that they end up rolling up and, thus, only allowing approximate values for their lateral sizes. The “rolling-up” behavior of large CdSe NPLs has been reported already.¹¹⁸

This is expected as the CdSe NPL flow reactor synthesis used is a one-pot approach, and the product from the flow reactor is not purified. Aside from the varying lateral size of the CdSe NPLs, the TEM images confirm a successful synthesis of CdSe NPLs in a flow reactor.



*Spherical MSCs were assumed for the calculation of the diameter

Figure 31: Schematic drawings of CdSe-360 MSC, CdSe-405 and a 3 ML CdSe NPL, accompanied by TEM images of these structures. (a) shows CdSe-360 MSC with a diameter of 1.19 nm and CdSe-405 MSC with a diameter of 1.60 nm. (b) shows a 3 ML CdSe NPL with a thickness of 0.9 nm. (c) and (d) show TEM images of the CdSe-MSCs synthesized in the flow reactor, whereas (e) and (f) show TEM images of the CdSe NPLs synthesized in the flow reactor. Figure by Funk et al. with slight modifications used with permission and under creative common license.⁹⁷

To further investigate the intermediate structure that is forming between the CdSe MSCs and the CdSe NPLs, emission spectra with an excitation wavelength of 350 nm have been recorded. 350 nm corresponds to a wavelength that is absorbed by the CdSe MSCs. Figure 32 shows these results.

At 210 °C and 60 s in the 10 cm oven (Figure 32a), a peak at 432 nm is visible. This peak corresponds to the CdSe-MSCs as they usually emit with high intensity in this range.^{102,114,119} Increasing the temperature to 225 °C and 60 s, the peak rises in its intensity. Furthermore, a slight shift is observable at around 426 nm. A further increase to 240 °C and 60 s leads to another emission peak shift. Additionally, a plateau is visible at around 530 nm. This plateau-like emission might originate from the intermediate structure forming in the synthesis. Switching the oven to 30 cm without changing the conditions (240 °C, 60 s) leads to a decrease in the emissions's intensity maximum. The plateau at 530 nm remains visible and barely decreases in its intensity. This strongly suggests that there might be an intermediate structure that emits at this wavelength range. Additionally, the emission's maximum shifted once again by a few

nanometers. The shift could be explained by the CdSe MSCs being influenced by the presence of this intermediate, as the CdSe MSCs are the building blocks for this intermediate structure. As they are used for building blocks, this likely affects the ligands on the surfaces of the CdSe MSCs, thus impacting their optical properties.¹⁰⁵ Furthermore, the decrease in the emission may also be a result of the CdSe MSCs being consumed for the formation of the intermediate structure. The plateau in the emission is also observed for the following residence time at 70 s and 240 °C, including the decrease in the emission intensity at around 426 nm. This is also the case for the experiment at 80 s and 240 °C, although the plateau starts to decrease in intensity, as well. Starting at 240 °C and 90 s, a small peak at 463 nm arises, originating from the 3 ML CdSe NPLs. In this sample, the emission in the region of 530 nm also notably lost intensity. At 240 °C and 120 s, the peak at 463 nm increased again, implying that more 3 ML CdSe NPLs have formed. Furthermore, the peak, which used to be located at 426 nm, shifts to around 416 nm. The plateau at around 530 nm is not visible in this spectrum anymore. Based on this spectrum, the intermediate structure is not as present as before. All these observations so far correspond well to the PLE spectra in Figure 30a.

The emission spectra in Figure 32b vary seemingly from the previous observations. Here, all experiments were conducted in a 30 cm oven. At 200 °C and 20 s, the emission's intensity increases to around 420 nm, thus confirming the presence of CdSe MSCs.^{102,114,119} The increase in this emission's intensity continues at 200 °C and 40 s. Additionally, there is a clear emission arising at around 530 nm. Similar to the previous flow reactor experiment, this is likely arising from the intermediate that starts to form. An increase in the residence time to 60 s at 200 °C barely changes the spectrum. Only an increase in temperature to 210 °C and 60 s leads to a notable increase in the overall emission at around 420 nm and the region around 530 nm. Starting at 220 °C and 60 s, the emission's intensity at 420 nm decreases while it remains unchanged for 530 nm. Like the previous experiment, the intermediate structure likely forms from the CdSe MSCs, hence, a decrease at 420 nm is observed. At 230 °C and 60 s, a tiny peak at 463 nm appears, confirming the formation of 3 ML CdSe NPLs. Another increase in temperature to 240 °C and 60 s not only leads to an increase in the emission intensity at 463 nm, but a new peak at 514 nm arises. This peak belongs to the 4 ML CdSe NPLs. At the final settings, that is 240 °C and 120 s, the peaks at 463 nm and 514 nm increase a lot in their intensity. This highly suggests that the concentration of 3 ML and 4 ML CdSe NPLs increased in the flow reactor as the samples were all prepared and diluted the same. Similar to the previous experiment, the emission at 530 nm decreased notably, suggesting that the intermediate structures have been consumed for the formation of the CdSe NPLs. Comparing both results, it becomes

evident that fewer CdSe NPLs have formed in Figure 32a compared to Figure 32b, although in both cases, a 30 cm oven has been used. The difference can be explained by the run time of the experiments, as all samples have been conducted in a single session. This means that in the left image, the overall experiment conducted in the 30 cm oven is shorter in time compared to the right image. As the flow reactor has a laminar flow profile, the precursor is likely impacted from the previously conducted experiments in Figure 32b.

Overall, these emission spectra with an excitation wavelength of 350 nm strongly suggest that after the formation of CdSe MSCs, an intermediate structure is forming before CdSe NPLs start to grow. Moreover, the CdSe MSCs are being used to form this intermediate structure.

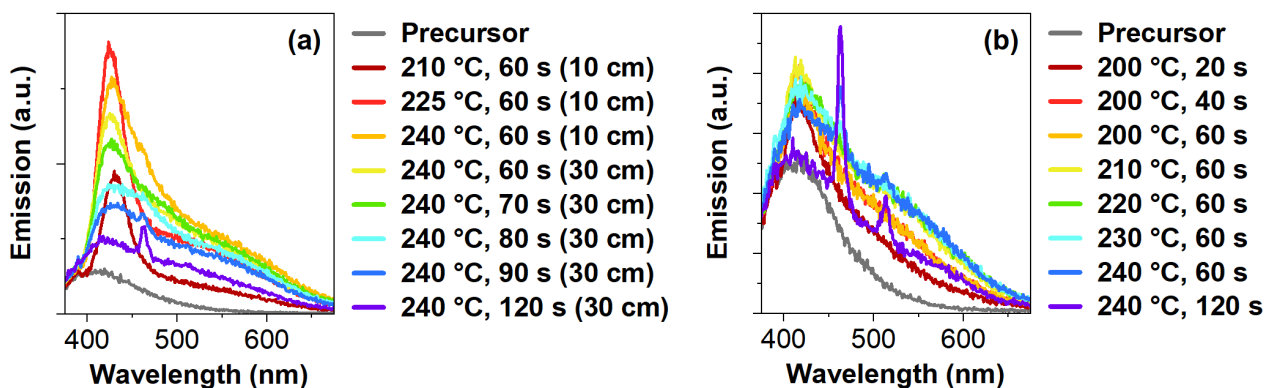


Figure 32: Emission spectra of flow reactor experiments with an excitation wavelength of 350 nm. (a) shows results for a 10 cm and 30 cm oven, while (b) is conducted entirely in a 30 cm oven. Figure by Funk et al. with slight modifications used with permission and under creative common license.⁹⁷

In the previous emission spectra, the excitation wavelength at 350 nm excites the CdSe MSCs more in comparison to the 3 ML CdSe NPLs, as their absorption maximum is at a larger wavelength of 435 nm. To fully verify when and how many CdSe NPLs formed in both experiments, the emission spectra with an excitation wavelength of 435 nm were taken in Figure 33.

Figure 33a shows that at 225 °C and 60 s in a 10 cm oven, no CdSe NPLs are present. Interestingly, the emission rises from 500 nm to 450 nm. This aligns with the previous emission spectra that the emission maximum for the CdSe MSCs lies at higher energy levels, consequently at smaller wavelengths. The sample at 240 °C and 60 s in the 10 cm oven has a high emission intensity with an excitation wavelength of 435 nm, which is like the previous results. Furthermore, a tiny peak at 463 nm is visible in this sample. While this sample contains CdSe MSCs and the intermediate structure, it seems that a very small population of 3 ML CdSe NPLs have formed, too. Switching to the 30 cm oven at 240 °C and 60 s leads to a visible decrease in the overall emission's intensity. At 240 °C and 70 s and 80 s, the spectra's overall emission

increased slightly but contains no CdSe NPLs. Once the synthesis is at 240 °C and 90 s, a visible peak at 463 nm appears, originating from the 3 ML CdSe NPLs that form in the flow reactor synthesis. Increasing the residence time to 120 s at 240 °C not only increases the peak's intensity at 463 nm, but another peak at 514 nm appears, corresponding to the 4 ML CdSe NPLs. Aside from the two peaks, the emission between 515 nm and 700 nm visibly decreased in this sample. It is possible that this overall emission decrease is a result of the CdSe MSCs being used for the formation of the CdSe NPLs. However, the emission may also result from CdSe nanodots as they are found as a side product in the synthesis.

Figure 33b shows the results conducted only in a 30 cm oven. The first samples, which include 200 °C and 20 s, 200 °C and 40 s, 200 °C and 60 s, and finally 210 °C and 60 s, show barely any emission at all. There is no evidence for any CdSe NPLs. At 220 °C and 60 s, a peak at 463 nm appears from the 3 ML CdSe NPLs, accompanied by another very small peak at 514 nm from the 4 ML CdSe NPLs. The peak at 514 nm barely increases at 230 °C and 60 s, while the other peak at 463 nm rises visibly for this sample. This trend, that the intensity at 463 nm increases more than at 514 nm, continues for 60 s at 240 °C and 120 s at 240 °C, respectively. Considering that the formation of 3 ML CdSe NPLs is more favored than that of 4 ML CdSe NPLs, this trend is within expectations. In the literature, thinner CdSe NPLs are usually more favored to form than thicker ones.¹⁰ The key difference between Figure 33a and Figure 33b lies in the emission of the CdSe MSCs. It is likely that in the first experiment in Figure 33a, their growth and formation are more favored than in the second experiment in Figure 33b. This would also explain the slight differences in Figures 32 and 30. Nevertheless, in both cases, CdSe MSCs have formed. In the flow reactor experiment with the two ovens, it becomes evident that, apparently, more CdSe MSCs have formed than in the flow reactor experiment with one single oven. In both flow reactor experiments, the formation of 3 ML and 4 ML CdSe NPLs is evident based on Figure 33.

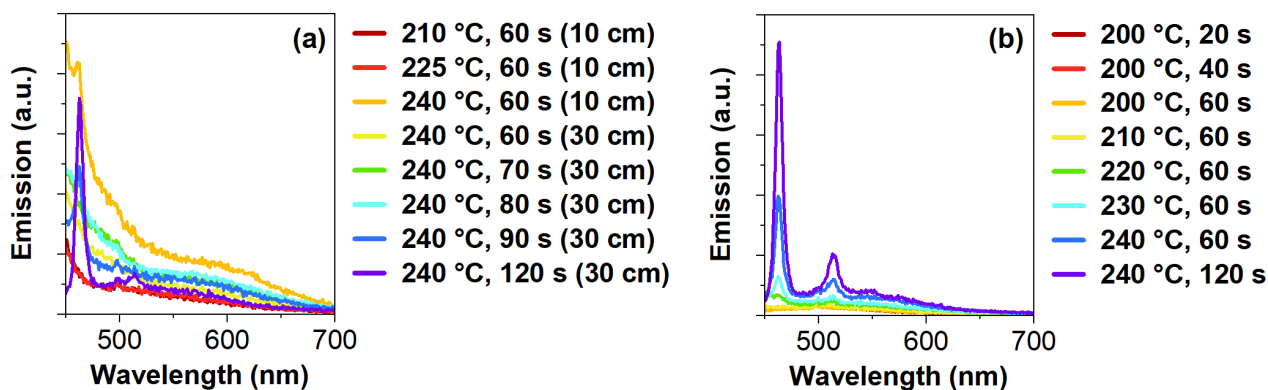


Figure 33: Emission spectra of flow reactor experiments with an excitation wavelength of 435 nm. (a) presents results for a 10 cm and 30 cm oven, while (b) showcases results from a 30 cm oven. Figure by Funk et al. with slight modifications used with permission and under creative common license.⁹⁷

It is already known for wurtzite CdSe NPLs that CdSe MSCs play a key role in their formation.⁴² This is contrary to the proposed growth mechanism of zinc blende CdSe NPLs by Riedinger et al. and by Peng et al. because none of them included CdSe MSCs.^{10,11} As CdSe MSCs are visible in the flow reactor synthesis, this raises the question of whether the flow reactor CdSe NPLs have a wurtzite or a zinc blende crystal structure.

Powder X-ray diffraction (powder XRD) measurements are a method for determining the crystal structure of the flow reactor CdSe NPLs. Figure 34 shows the results of the powder XRD measurements. Based on similar synthesis approaches, the CdSe NPLs from the flow reactor are expected to have a zinc blende structure.^{10,11,48,101} To verify the results from the flow reactor, the flow reactor precursor has also been conducted as a regular batch experiment (rose color in Figure 34). In this experiment, the precursor was stirred at 240 °C for 10 min in a nitrogen atmosphere before cooling it rapidly down. Both the NPLs from the flow reactor and from the flask synthesis showcase diffraction patterns that generally suit the zinc blend structure the most. The calculated d-spacings for the wurtzite CdSe bulk,¹²⁰ the zinc blende CdSe bulk,¹²⁰ as well as the found d-spacings for the synthesized CdSe NPLs, which can be found in Table 2. Additional values can be found in the appendix. It becomes apparent that the synthesized CdSe NPLs have a diffraction at a 2θ -value of approximately 20, which doesn't belong to the wurtzite or the zinc blende structure. This value can be assigned to organic ligands, according to literature.¹²¹

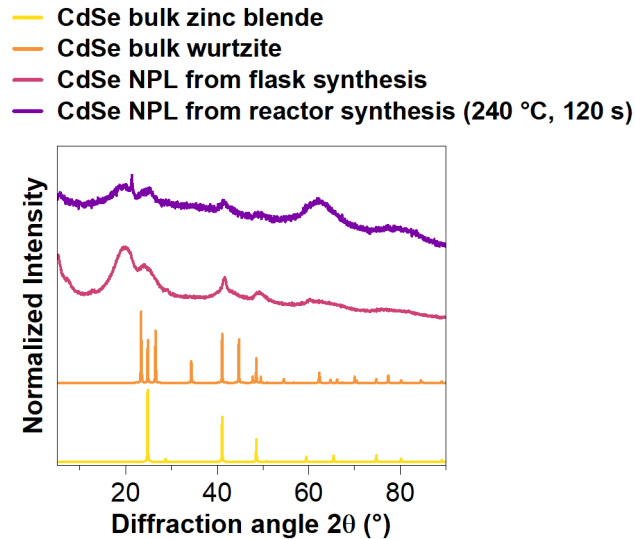


Figure 34: Powder XRD measurements to determine the crystal structure of the CdSe NPLs. Violet shows the CdSe NPLs produced in a flow reactor synthesis, red shows the CdSe NPLs produced in a flask. In both cases, the precursor used is the same. Orange and yellow show the bulk wurtzite and bulk zinc blende structures for CdSe, respectively.¹²⁰ Figure by Funk et al. with slight modifications used with permission and under creative common license.⁹⁷

Table 2: The d-spacings for bulk CdSe with a wurtzite and zinc blende structure,¹²⁰ as well as the d-spacings found for the CdSe NPLs synthesized in a flask and in the flow reactor. Additional information can be found in the appendix.

Wurtzite CdSe bulk ¹²⁰ [Å]	Zinc blende CdSe bulk ¹²⁰ [Å]	CdSe NPL	
		Flask synthesis [Å]	Flow reactor synthesis [Å]
3.810	3.590	4.497	4.545
3.590	2.209	3.688	4.167
3.369	1.885	2.166	3.604
2.621	1.564	1.855	2.175
2.209	1.436	1.536	1.856
2.036	1.278	–	–
1.885	–	–	–
1.500	–	–	–
1.242	–	–	–

Another method to further determine the crystal structure of the CdSe NPLs is to calculate the d-spacing from the TEM diffractions. Figure 35 showcases the selected area for electron diffraction (SAED) for CdSe NPLs synthesized in a flask. The value 1.293 Å is in good agreement with the zinc blende structure, whereas the value 2.024 Å is associated with the wurtzite

structure (Figure 35a). Based on the synthesis conditions which include the usage of carboxylates, it is unlikely that the CdSe NPLs or the CdSe MSCs showcase a wurtzite structure.^{115,122–124} A transition from zinc blende CdSe NPLs to wurtzite CdSe NPLs is only plausible through the introduction of an amine.¹²² For the CdSe MSCs, the formation of a wurtzite-like structure usually occurs when the concentration of Selenium is high.¹²³ Furthermore, a temperature below 260 °C promotes growth of a zinc blende structure, whereas temperatures of 300 °C promote growth of a wurtzite structure.¹²⁵ Finally, Figure 35a showcases very broad rings, which makes it more difficult to find the appropriate ring for the d-spacing calculation.¹²⁶

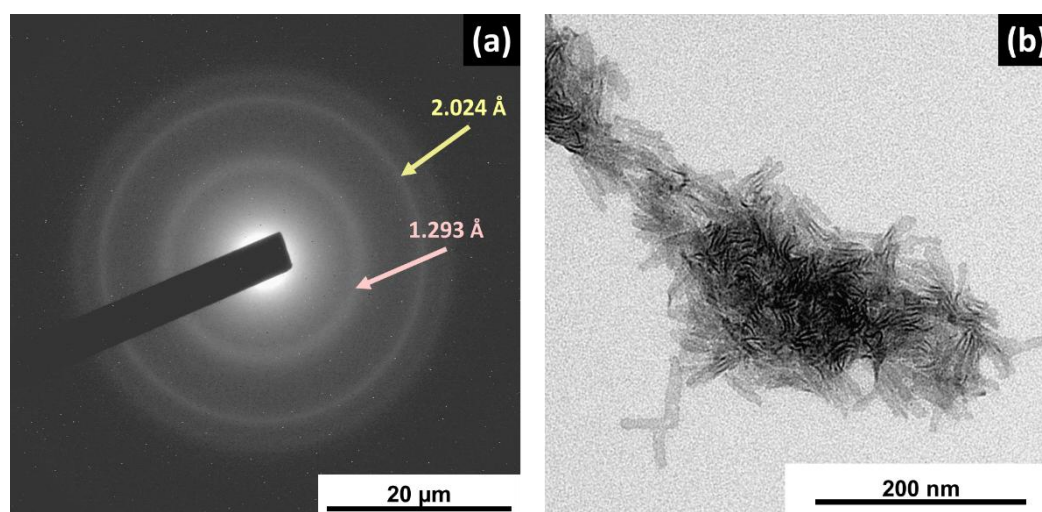


Figure 35: TEM diffractions, which are used to determine the crystal structure of the CdSe NPLs synthesized in a flask at 240 °C for 10 min. (a) presents the SAED, (b) the corresponding TEM images of the CdSe NPLs.

Overall, the CdSe NPLs likely have a zinc blende structure. After obtaining the information on the crystal structure, more information about the formation of the CdSe NPLs is needed. This additional information can be obtained through small-angle X-ray scattering (SAXS).

In Figure 36, the normalized SAXS patterns are shown, including the different power-laws in black for the different shapes. At first, at 200 °C and 20 s, the low q regime strongly indicates a spherical-like structure. The wording *spherical-like* is chosen, as the CdSe MSCs observed in the flow reactor likely have a non-stoichiometric shape.^{110–112} Over the course of the reaction, the spherical-like structure q^0 slowly transitions to the anisotropic platelet structure q^{-2} , which is clearly obtained from the flow reactor sample at 240 °C and 120 s. Figure 36 confirms that in the early stages of the CdSe NPL synthesis, structures can be found which do not exhibit a typical anisotropic platelet-shape like the CdSe NPLs. Instead, this anisotropic platelet-shape evolves over time.

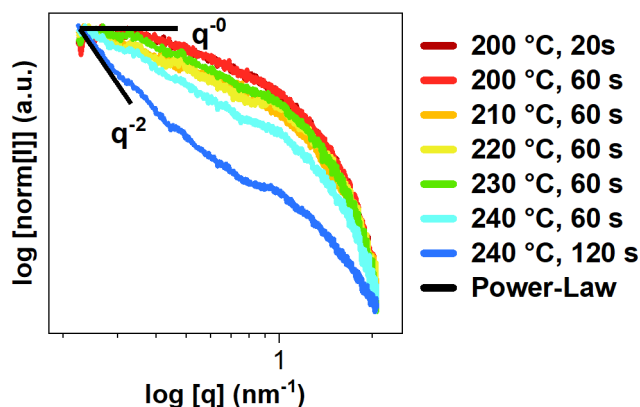


Figure 36: Normalized SAXS pattern of the flow reactor samples showcasing the different power-law in black. The flow reactor samples were conducted at different residence times and temperatures, shown here in a rainbow-color palette. Figure by Funk et al. with slight modifications used with permission and under creative common license.⁹⁷

The SAXS patterns were also fitted as shown in Figure 37. To facilitate the fitting process with the non-stoichiometric CdSe MSCs, the particles were assumed to be spherical apart from the final sample. Additionally, it should be noted that all diameters and lengths obtained from the SAXS fits are only average values.

With these assumptions made, it allows the use of the sphere fit for the first sample at 200 °C and 20 s. The applied sphere-fit revealed a diameter of 1.8 nm for this sample, which corresponds to the size regime of CdSe MSCs.^{52,109} In the next sample at 200 °C and 60 s, the sphere fit was once again applied, resulting in a diameter of 3.2 nm. The diameter visibly increased, indicating that the CdSe MSCs agglomerate during the synthesis. As the CdSe MSCs are likely non-stoichiometric in shape, the found diameter might depend on the orientation of the CdSe MSCs, as well. This observed agglomeration may be the first step in the formation of an intermediate structure. Based on the previous results, an intermediate structure is likely forming before CdSe NPL starts to form.

While an agglomeration is visible for the sample at 200 °C and 60 s, the SAXS pattern also reveals that no oriented attachment process takes place in the synthesis. A superlattice would be expected for an oriented attachment,¹²⁷ which is absent in the SAXS results presented in Figure 37. Meanwhile, the agglomeration is also present in the low q region of the flow reactor sample 210 °C and 60 s, the sample 220 °C and 60 s, and the sample 230 °C and 60 s, respectively. The observable agglomeration further indicates that an intermediate structure is forming. As the structure of the intermediate is unknown, the SAXS fit used for the following samples is a combination of powerlaw and sphere model. Interestingly, starting with the sample at

210 °C and 60 s, the diameter obtained from the combined fit model decreases to 2.4 nm. The diameter further decreases for the following sample at 220 °C and 60 s to 1.8 nm. However, for the sample at 230 °C and 60 s the diameter starts to increase again to 6.4 nm.

The decrease in diameter, then the following sudden increase in diameter, connects to the previous blue-shifts observed in the corresponding PLE spectra in Figure 30b. As the PLE spectra indicate stronger exciton confinement, the intermediate forming is smaller in size than the CdSe MSCs that formed prior. This observation is within expectations based on the SAXS results. Additionally, the sample at 230 °C and 60 s also exhibits the light-hole peak at 435 nm in the PLE spectrum in Figure 30b. This suggests that the previously formed intermediate turned into very small CdSe NPLs, as suggested by the increased diameter of 6.4 nm. In the next sample at 240 °C and 60 s, the diameter from the combined fit increased again to 15 nm.

For the last sample, at 240 °C and 120 s, the parallelepiped fit model was used. This fit model was also used by Bouet et al. when they applied a SAXS fit to their CdSe NPLs.²⁷ Based on the SAXS pattern in Figure 37, the obtained 3 ML CdSe NPLs from the flow reactor have a thickness of 0.9 nm, which is the same value as reported by Bouet et al. for their 3 ML CdSe NPLs.²⁷ The fit from Figure 37 also results in CdSe NPL sizes of 13.8 nm x 161.3 nm. This result is in good agreement with the CdSe NPL sizes found in the TEM image results from Figure 31.

All results so far give evidence that CdSe MSCs form first, which turn into intermediate. This intermediate then further transforms into the CdSe NPLs. However, the results so far give no indication of the exact shape and structure of the intermediate.

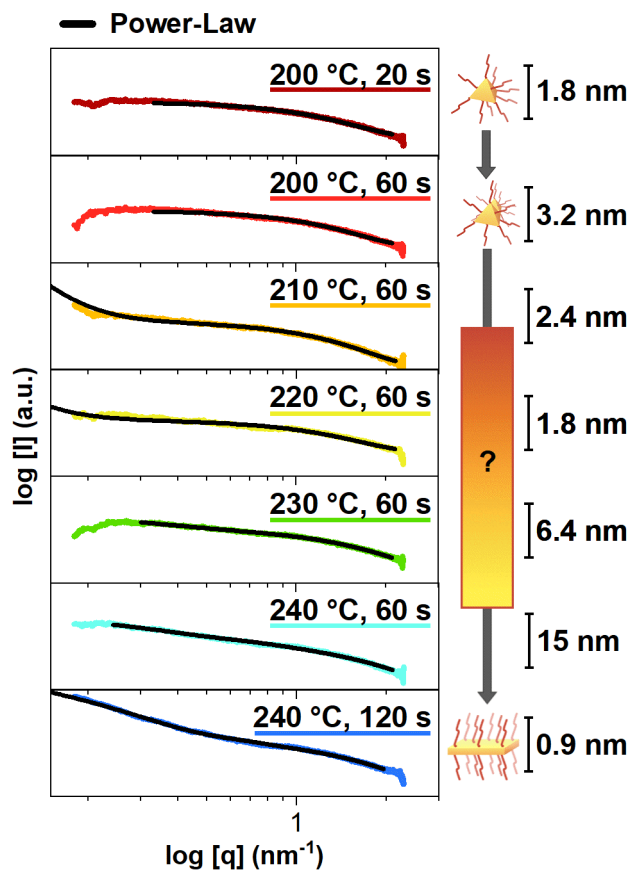


Figure 37: The SAXS data and fits from various fitting models that reveal average solvation sizes. For the first two samples (200 °C, 20 s, and 200 °C, 60 s), a sphere model was used. The last sample (240 °C, 120 s) utilized a parallelepiped model for the SAXS fit. The remaining sizes were obtained using a sphere model in combination with power-law. On the right side are theoretical drawings of what the structure may look like based on the average solvation size obtained from the fit. Figure by Funk et al. with slight modifications used with permission and under creative common license.⁹⁷

There are some proposed intermediate structures that may apply to the intermediate found in the CdSe NPL flow reactor synthesis. These possible intermediates are shown in Figure 38.

One possible structure is the 2D-embryo structure proposed by Peng et al.¹¹ They proposed that the spherical CdSe seeds they used firstly form basal planes through intra-particle ripening before these as-formed intermediates with basal planes fuse together to form a 2D-embryo structure through oriented attachment.¹¹ It is likely that the intermediate structure observed may consist of these two structures: First, the CdSe MSCs agglomerate (see SAXS results), and then they slowly form basal planes (see PLE spectra). This concept would be similar to the one proposed by Peng et al.,¹¹ with the difference that the CdSe MSCs agglomerate and do not undergo an oriented attachment process.

Another structure to describe the intermediate would be an egg-tray structure, which has been proposed by Weller et al. for PbS sheets.⁴⁰ They proposed that this structure also forms through oriented attachment. Furthermore, the oleic acid used as a ligand may initiate structural changes to promote surface reconstruction to form 2D PbS sheets from this intermediate structure.⁴⁰ While the formation of this intermediate relies on oriented attachment once again, there is still a possibility that the CdSe MSCs observed in the flow reactor agglomerate in an egg-tray fashion, as well.

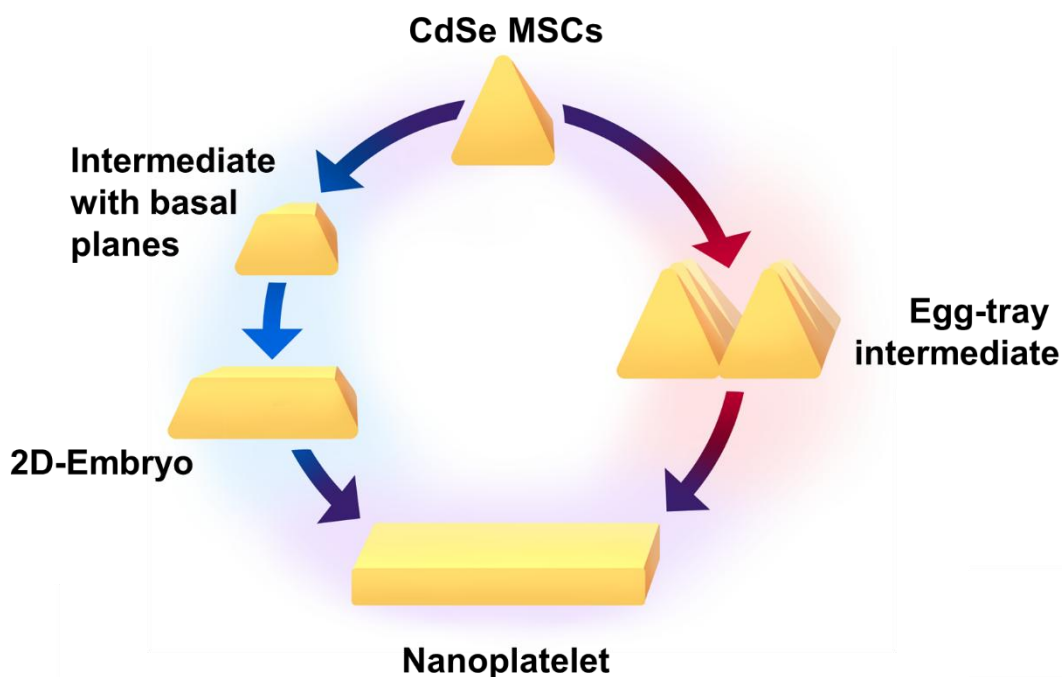


Figure 38: Schematic drawings of possible intermediate structures. The blue arrows showcase the intermediate structures proposed by Peng et al.¹¹ The red arrows showcase the intermediate structure proposed by Weller et al. for the PbS sheets.⁴⁰ Both pathways represent plausible intermediate structures, which may form during the CdSe NPL synthesis.

Based on all the results found to connect the CdSe MSCs to the CdSe NPLs, it seems likely that the formation is a three-step process. A schematic drawing of two potential three-step processes is shown in Figure 39. In the first step of the CdSe NPL synthesis, CdSe MSCs form (Figure 39a). As CdSe MSCs families, CdSe-360 and CdSe-405 could be determined based on the absorption and PLE spectra. Then, two potential pathways are possible for the second step.

Following the red arrows, the CdSe MSCs population agglomerate (Figure 39b). While an agglomeration alone will not lead to the thin CdSe NPLs, they additionally need to undergo intra-particle ripening and size focusing. This step is most similar to the proposed intermediates by Peng et al.¹¹ and Weller et al.⁴⁰ Through the size focus process, an intermediate-like structure is formed, which leads to the earlier blue shifts observed in the PLE spectra. This intermediate

then ripens to a small, anisotropic CdSe NPL in the third step, which could be confirmed by the increasing size in the SAXS results and the corresponding PLE spectra.

The other potential pathway for the second step pathway is marked by blue arrows, in which the CdSe MSCs act as monomer reservoirs (Figure 39c). This pathway is like the proposed growth mechanism by Riedinger et al.¹⁰ In their proposed growth theory, CdSe NPL nuclei form. Additionally, the formation of insoluble, concentrated Cd(OAc)₂ droplets in the solution promotes island-nucleation-limited growth of these nuclei. Connecting their theory to the CdSe MSCs, it is possible that the CdSe MSCs release so many monomer units that their concentration increases rapidly locally. This part with a high number of monomers may act like the droplet from the proposed theory. Similar to the other proposed pathway, a small CdSe NPL is then forming.

Finally, the third step begins, in which the nanoplatelets grow, especially in the lateral dimensions (Figure 39d). Under specific conditions, even growth in thickness occurs, which would then follow the growth model by Riedinger et al.¹⁰ Both pathways combined likely play a vital role in the growth of CdSe NPLs. The intraparticle ripening and size focusing may occur by partial dissolution process because the CdSe MSC agglomerates need to reconstruct to form an intermediate. Additionally, the released CdSe monomer units from the dissolution process may attach to the intermediate structure so that it can grow in the lateral dimensions, like a CdSe NPL. As an intermediate structure is observed in the SAXS patterns and PLE spectra, the combination of both pathways is most likely closest to the actual formation of CdSe NPLs.

of multiple CdSe MSC families at once during the synthesis has already been reported,^{102,113} this observation is thus within expectations. Moreover, PLE spectra revealed the formation of an intermediate structure before CdSe NPL formed. TEM images confirmed the presence of CdSe MSCs and CdSe NPLs from the flow reactor synthesis method. Additional XRD measurement confirmed a zinc blende structure for the obtained CdSe NPLs from the flow reactor. The emission spectra, obtained with an excitation wavelength of 435 nm, confirmed the formation of CdSe NPLs with a small nanodot byproduct. In the emission spectra in which the samples were excited with 350 nm, a blue-shift was observed, giving further evidence of the formation of an intermediate structure. SAXS pattern and fits reveal the transformation of CdSe MSCs to CdSe NPLs while forming an intermediate structure. The results were used to propose a growth mechanism for the CdSe NPLs, which involve the CdSe MSCs and an intermediate structure.

6.3 Adding a shell to CdSe NPL

CdSe NPLs can be successfully synthesized in a flow reactor, enabling mass production of these anisotropic structures. As access to mass production is a big step in using CdSe NPLs for applications, their quantum yield leaves room for improvement.¹²⁹ One solution to improve the QY is to improve surface passivation by introducing bromide.¹²⁹ However, other methods may be preferred to improve the QY of CdSe NPLs, which may depend on their final application. In the following are proof-of-principle results to encapsulate CdSe NPLs with two different methods.

6.3.1 Encapsulation of CdSe NPL in polystyrene – PI-b-PEO shell

CdSe NPLs with oleic acid ligands are not water-stable, which makes it challenging to use them for possible biological applications. Hereby, the seeded emulsion polymerization was used to encapsulate the anisotropic CdSe NPLs, as this method can be used for any nanoparticle shape and size.⁶³ A polystyrene-PI-b-PEO shell was used to encapsulate the CdSe NPLs. All results can be found in Figure 40.

The encapsulated CdSe NPLs retain their optical features, which can be seen in Figure 40a. In contrast to the absorption peaks, the emission of the encapsulated CdSe NPLs is gone. The slight shift in the absorbance spectra can be explained by the addition of PI-b-PEO.¹¹⁴ This observation can be explained by the encapsulation of the CdSe NPLs in the TEM images (Figures 40c and 40d). Before the encapsulation, the CdSe NPLs already had a low quantum yield of below 1 %. Oleic acid as a ligand can promote the stacking of CdSe NPLs.¹³⁰ Through the encapsulation, mainly CdSe NPL stacks were encapsulated which can be seen in Figure 40d.

The stacking of the CdSe NPLs results in meeting the requirements for a HOMO-FRET to occur. Within these stacks, the FRET occurs rapidly until the exciton gets trapped by a quencher NPL.^{85,131} Once the exciton is trapped, a non-radiative recombination happens, resulting in a lower QY.⁸⁵ The quencher NPL can be explained by the emission intermittency, commonly called blinking.^{132,133} As CdSe NPL exhibit trap states, they may switch between an “on” and an “off” state. During the “on” state, the CdSe NPLs emit while being in an “off” state, mainly non-radiative recombinations of the exciton occur.¹³²

While the stacking of CdSe NPLs within the polystyrene-PI-b-PEO shells led to these non-emitting products, the encapsulation process itself worked greatly on these anisotropic nanoparticles. A scheme to portray the encapsulation process is also shown in Figures 40e and 40f. Although a polymer excess of 12000 per particle was used for this method, which would lead to single-encapsulated particles in theory, it is evidently not enough to prevent the stacking of these CdSe NPLs. As already mentioned above, OA promotes stacking. Consequently, in order to obtain single-encapsulated CdSe NPLs, a ligand exchange right before the encapsulation process likely prevents the stacking process from happening. That a ligand exchange prevents the CdSe NPLs from stacking has already been reported.¹³⁰

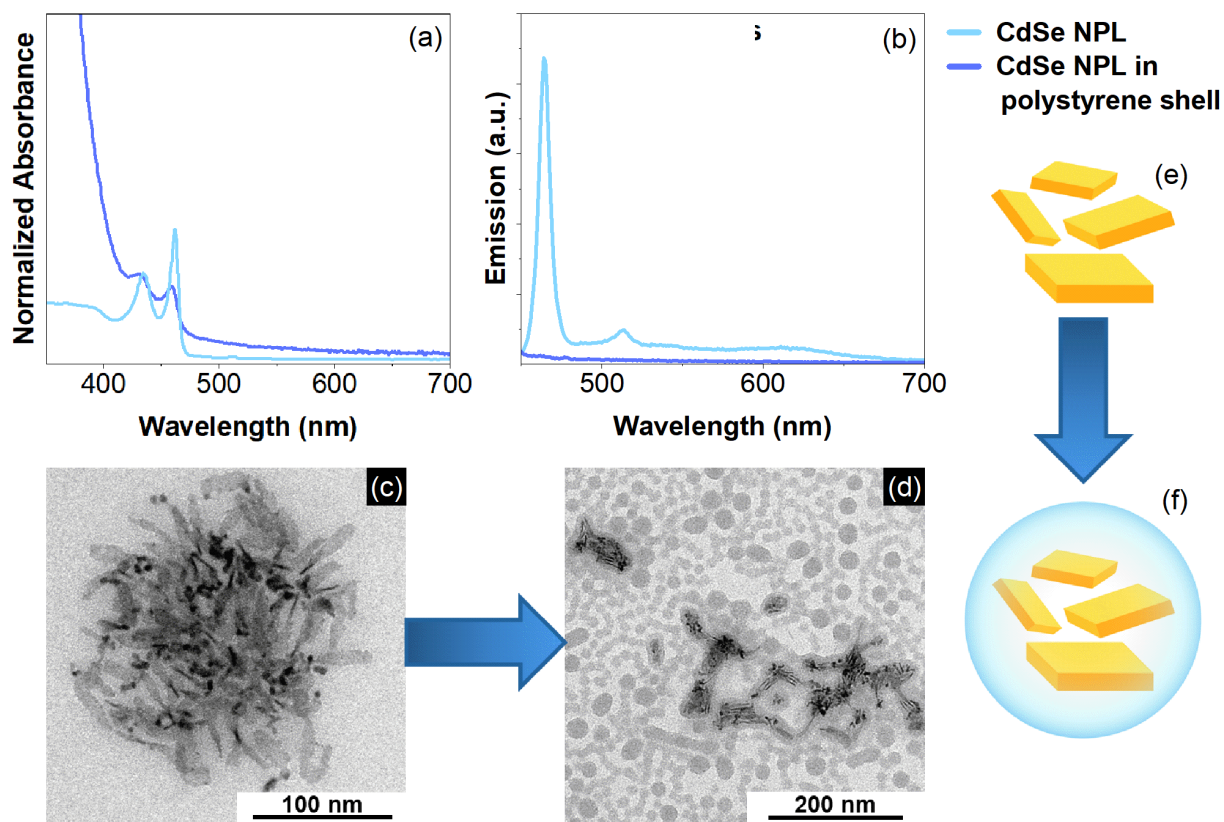


Figure 40: Results of the CdSe NPLs encapsulated in a polystyrene-PI-b-PEO shell. (a) shows the normalized absorption of the CdSe NPLs before and after encapsulation and (b) the respective emission spectra. The CdSe NPL with and without the polystyrene shell were normalized at the light-hole absorbance peak with a peak maxima at 435 nm and 431 nm respectively. TEM images of the CdSe NPL before encapsulation (c) and after encapsulation (d). (e) and (f) show a schematic drawing of how the CdSe NPLs were encapsulated in the polystyrene-PI-b-PEO shell.

Another important aspect of encapsulation is long-term stability. Figure 41 shows the aging of an encapsulated CdSe NPL batch after 7 months. It becomes apparent that after 7 months, the amount of CdSe NPLs decreased, and CdSe quantum dots have apparently formed based on the very broad absorption. The polymer shell itself might explain this. Only PI-b-PEO and polystyrene were used to encapsulate the CdSe NPLs. Adding divinyl benzene could have improved the shell with cross-polymerization as this would lead to a more dense polymer shell, improving the long-term stability.¹³⁴

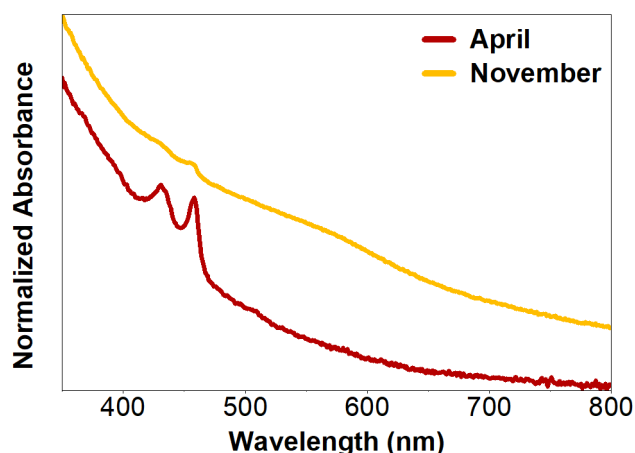


Figure 41: Aging experiment results for the encapsulated CdSe NPLs in a polystyrene-PI-b-PEO shell. In red is the “newly” polymerized batch from April, and marked in orange is the same batch after 7 months (November).

Figures 40 and 41 show that the encapsulation of CdSe NPLs in a polystyrene-PI-b-PEO shell works as a proof-of-concept. Stacking of the CdSe NPLs needs to be avoided, and the addition of divinyl benzene to ensure long-term stability is recommended.

6.3.2 CdSe/CdS core-shell NPL

Another method to shell and optimize the CdSe NPLs is the high-temperature thick-shell method developed by Riedinger et al.³¹ The results from this shelling method are shown in Figure 42. Figure 42a shows that a clear red-shift appeared in the absorption, as well as in the emission spectrum. The exciton in the CdSe/CdS core-shell NPL is less confined with the CdS shell. Additionally, electrons can delocalize into the shell so that these results are within expectations. A red shift in the spectra, including the broadening of the emission, has been reported, as well.³¹ The FWHM in the emission broadened from 6 nm to 14 nm (Figure 42b). A similar increase in the FWHM is reported for CdSe/CdS core-shell NPLs.¹³⁵

Figures 42c and 42d are TEM images of the CdSe NPLs prior to the shelling. Similar to before, only approximate values for the length and width can be taken as the CdSe NPLs were large and started to roll up.¹¹⁸ As a result, the CdSe NPLs have a length of $48 \text{ nm} \pm 110 \text{ nm}$, a width of $23 \text{ nm} \pm 4 \text{ nm}$, and, thus, a lateral area of $1119 \text{ nm}^2 \pm 340 \text{ nm}^2$. Compared to the CdSe/CdS core-shell NPLs, there is a significant change in the size of the core-shell NPLs. Unlike before, the CdSe/CdS core-shell NPLs do not roll up anymore, making it easier to gather their sizes. These core-shell NPLs have a length of $65 \text{ nm} \pm 11 \text{ nm}$, and a width of $29 \text{ nm} \pm 7 \text{ nm}$, resulting in a lateral size of $1896 \text{ nm}^2 \pm 627 \text{ nm}^2$. Based on the lateral size of the CdSe NPLs, it is not surprising that the determined QY is once again below 1 %. Interestingly, the QY improved to

1.5 % through the addition of the CdS shell despite the initial QY being very low. This is once again within expectations as the CdS shell passivates the surfaces of the core CdSe NPL, thus improving the QY.

A close look at the TEM images of Figures 42e and 42f reveals that the CdSe/CdS core-shell NPLs have a caterpillar-like appearance. In Figure 42 e, the upper small NPL even looks like it has a small cut in it. This structure may result from etching processes caused by the oleylamine used in the shelling process. As reported in the paper with 4 ML thick CdSe NPLs,³¹ the 3 ML thick CdSe NPL used for these results may be etched so that this caterpillar structure appears at the end.

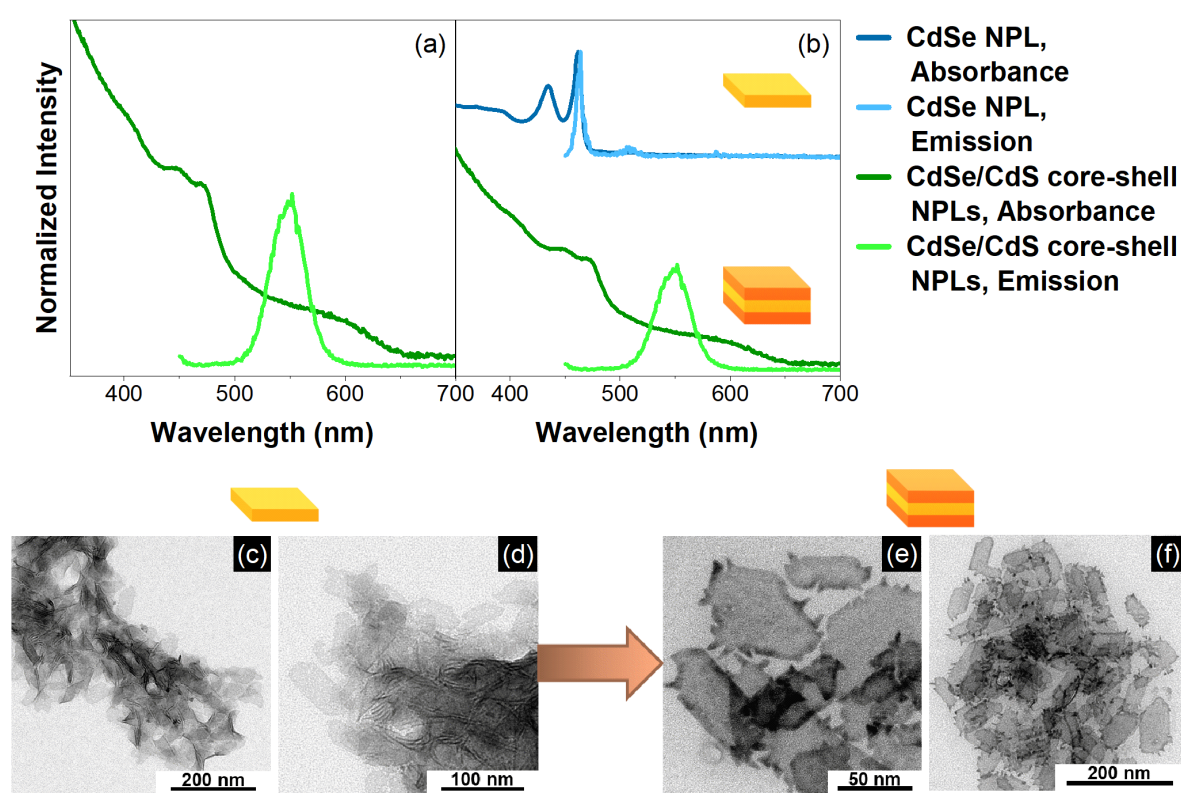


Figure 42: Results of the CdSe/CdS core-shell NPLs produced with the method by Riedinger et al.³¹ (a) shows the absorption and emission of the CdSe/CdS core/shell NPLs. In (b), the absorption and emission of the CdSe NPLs before the CdS-shell addition are shown. Absorption is normalized at the heavy-hole absorption peak that is 462 nm for CdSe NPLs and 471 nm for the CdSe/CdS core/shell NPLs. (c) and (d) show TEM images of the CdSe NPLs before the shell-method is performed. In (e) and (f) are TEM images of the finished CdSe/CdS core-shell NPLs present.

Figure 42 shows that the addition of a CdS shell to the CdSe NPLs works, once again, as a proof-of-principle. By tuning the optical properties of the CdSe NPLs with a CdS shell, multiple color ranges can be accessed for future applications, like QLED screens.¹³⁵

7 Outlook

The flow reactor synthesis of CdSe NPLs enables mass-producing CdSe NPLs for various applications. However, some improvements are still needed to make this happen.

One aspect is to create CdSe NPLs with a small and uniform lateral size. The small size is needed to ensure a high QY.¹³⁶ A uniform lateral size and thickness are desired to ensure that the CdSe NPLs exhibit similar optical properties, which are typical for CdSe NPLs, for future applications. To achieve this, one possibility would be to separate the cadmium precursor from the selenium precursor and using a mixing chamber in the flow reactor setup,¹³⁷ so that the growth and nucleation of the CdSe NPLs can be adequately separated. In this approach, the selenium component remains Se-ODE. The cadmium component should again be cadmium oleate, to which acetic acid is added at least 30 min before the flow reactor synthesis. By using two syringe pumps and the mixing chamber, both the cadmium and selenium precursors are then mixed in the flow reactor system, which likely improves the lateral size of the CdSe NPLs. Through this method, an adjustment of the reaction time, as well as finding a suitable temperature for the mixing chamber and the oven are needed.

Once the flow reactor synthesized CdSe NPLs have similar lateral sizes, they can be used for various applications. Improving the polymer shell could enable, for example, bio-labeling *ex vivo* applications. With their narrow absorption and emission peaks, CdSe NPLs have the potential to be even more sensitive bio labels than CdSe quantum dots with their broader absorption and emission.^{138,139} Another possible future application can be found in the QLED TVs mentioned in the introduction.⁴ The CdSe NPLs and CdSe/CdS core-shell NPLs have the potential to improve color purity significantly in LED applications with their narrow emission peaks. Reported for blue-emitting,¹⁴⁰ green-emitting,¹³⁵ and red-emitting NPLs,¹⁴¹ all important additive colors for LED applications can be synthesized, so that semiconductor quantum dots can be replaced with semiconductor nanoplatelets in this specific case.

Overall, the ability to mass produce CdSe NPLs in a flow reactor and the ability to modify them post-synthesis opens up improved applications, and also, technical improvements for the future.

8 Materials and methods

8.1 Applied devices and materials

Table 3: Applied devices, software and their manufacturers.

Devices and software	Manufactures
Varian Cary 50 spectrometer	AGILENT TECHNOLOGIES
Varian Cary UV Scan Application software	AGILENT TECHNOLOGIES
Citavi software	Swiss Academic Software GmbH
Clip Studio Paint Pro software	CELSYS
Electron microscope JEM-1011	JEOL
Electron microscope JEM-2200FS	JEOL
Excel 2019 software	Microsoft Corporation
Fluoromax-4 spectrofluorometer	HORIBA Scientific
FluorEssence software version 3.5	HORIBA Scientific
Heating Catridge	HS-Heizelemente
Elotech R2500 temperature controller with 16 zones	Elotech Industrieelektronik
Heat exchanger (titanium)	Micro4industries
ImageJ software	Wayne Rasband
Mercury software	Cambridge Crystallographic Data Centre
MultiSpec Pro 2 software	Tec5
OriginPro 2022b software	OriginLab Corporation
P03 X-ray Scattering Beamline PETRA III	DESY, Hamburg
PILATUS 2M detector	Dectris
PowDLL software	N. Kourkoumelis
Powerpoint 2019 software	Microsoft Corporation
PEEK-Tubing and ferrules	UPCHURCH SCIENTIFIC, Klaus Ziemer
QMix Elements software	CETONI
Reactor Oven (titanium-tubing part)	ETHEN ROHRE
Reactor Oven (aluminum housing, with spiral titanium-tubing)	University Hamburg Workshop
SasView software	NSF award DMR-0520547; SINE2020 project

Table 3 (continuation): Applied devices, software and their manufacturers.

Devices and software	Manufactures
Sigma centrifuges (type 2-16P and 3-18KS)	Sigma
SIMHEX interdigital micro mixer (encapsulation)	Micro4industries
NEMESYS Syringe Pumps (Flow Reactor and encapsulation process), mid-pressure modules	CETONI
SuperK Fianium High Power Supercontinuum laser (1.5 W visible power)	NKT Photonics
Temperature detector (flow reactor)	Unitherm, PT-100, two-wire configuration
Titanium valco union, ferrules and nuts	Macherey-Nagel
UV/Vis measuring cell (flow reactor), 3 mm, PEEK	Knauer GmbH
UV/Vis spectrometer (flow reactor) with optical fibers	Tec5
Water chiller	Julabo F25-MC
Word 2019 software	Microsoft Corporation
X'Pert PRO X-Ray diffractometer	Philips

8.2 Applied chemicals

Table 4: Applied chemicals and their manufacturers.

Substances, Purity	Manufactures	Abbreviation
Acetic acid, ≥ 99.5 %	Chem Solute	AcOH
Acetic anhydride, ≥ 99 %	Merck	
Acetone, ≥ 99.8 %	VWR Chemicals	
Azobis(isobutyronitrile), ≥ 98 %	Merck	AIBN
Cadmium acetate, anhydrous, ≥ 99 %	Carl Roth and Merck	Cd(OAc) ₂
Cadmium oxide, ≥ 99.9 %	Merck	CdO
Coumarin 153, ≥ 99 %	Sigma-Aldrich	
Ethanol, ≥ 99.8 %	VWR Chemicals	EtOH
Ethyl acetate, ≥ 99.8 %	VWR Chemicals	
Glycerol, ≥ 99.5 %	Sigma-Aldrich	
<i>n</i> -Hexane, ≥ 95 %	Fisher Chemicals	
Hydrochloric acid, 37%	VWR Chemicals	HCl
Hydrochloric acid, 1 M	Own production	HCl
Isopropanol, ≥ 99.7 %	VWR Chemicals	
Methanol, ≥ 99.8 %	VWR Chemicals	MeOH
Methyl acetate, ≥ 99 %	Merck	
1-Octanthiol, ≥ 98.5 %	Sigma-Aldrich	
1-Octadecene, ≥ 90 %	Sigma-Aldrich	ODE
Oleic Acid, ≥ 90 %	Sigma-Aldrich	OA
Oleylamine, ≥ 70 %	Sigma-Aldrich	
Polyisoprene-block-poly(ethylene oxide)	CAN GmbH/ Fraunhofer-IAP CAN	PI-b-PEO
Selenium powder, ≥ 99.9 %	Sigma-Aldrich	Se
Styrene, stabilized, ≥ 99 %	Merck	
Tetrahydrofuran, stabilized, ≥ 99 %	VWR Chemicals	THF
Polyoxyethylene(20)-sorbitan-monosuccinate (TWEEN 60), ≥ 90 %	Sigma-Aldrich	TWEEN 60

8.3 Experimental section

8.3.1 Synthesis Methods

8.3.1.1 Synthesis of Se-ODE solution

Depending on the desired concentration, the amount of selenium varied in relation to the ODE.

For 10 mL 0.15 M Se-ODE solution, 120 mg (1.50 mmol) Se and 10 mL ODE were added to a three-neck flask and degassed for 30 min at 110 °C. The mixture was then heated to 205 °C for 60 min. At this time, the grey suspension turned into a yellow solution. Ultimately, the finished product was kept under a nitrogen atmosphere for later usage.

The procedure for a 0.19 M Se-ODE solution was similar to the previously mentioned solution. However, 50 mL of ODE were used, so 750 mg (9.50 mmol) Se were needed. The degassing time was extended to two hours, and the heating time at 205 °C was also extended to six hours to obtain a yellow solution.

8.3.1.2 Synthesis of CdSe NPL with Cd(OAc)₂ and without methyl acetate

In a three-neck flask, 19 mg (0.15 mmol) CdO, 190 μL (0.60 mmol) OA, and 19 mL of ODE were degassed at 110 °C for 30 min. Then, the mixture was heated to 240 °C and held for 30 min under a nitrogen atmosphere. The previously brownish turbid suspension turned into a colorless clear solution in this process. After this mixture cooled down to RT, 60 mg (0.23 mmol) of Cd(OAc)₂ was added to the flask. With this addition, the colorless turbid suspension was degassed again for 20 min. In an attempt to dissolve the Cd(OAc)₂, the mixture was heated to 210 °C for 10 min under nitrogen flow. After the mixture cooled down to 80 °C, 1 mL of a 0.19 M Se-ODE solution was added. Another final degassing step at 80 °C for 10 min was conducted. Under a nitrogen atmosphere, the mixture was heated to 240 °C and held there for 10 min before rapidly cooling down the yellow-turbid suspension.

8.3.1.3 Synthesis of CdSe NPL with Cd(OAc)₂ and with methyl acetate

The synthesis method was similar to the method mentioned in Chapter 9.3.2.1 with minor adjustments. After the 0.15 M Se-ODE solution was added and the mixture was degassed, 50 μL (0.63 mmol) of methyl acetate was added to the mixture. Before heating the mixture, the mixture was stirred for an additional hour under nitrogen flow at room temperature. Like the method mentioned in 9.3.2.1, the synthesis of CdSe NPL happened at 240 °C with a reaction time of 10 min.

8.3.1.4 Synthesis of CdSe NPL with Cd(OAc)₂ and with acetic anhydride

Aside from the flow reactor project, this synthesis was used to produce CdSe NPL for the CdS shell growth in chapter 9.3.1.13. At first, 87 mg (0.33 mmol) Cd(OAc)₂, 250 μL (0.79 mmol) OA, 70 μL (0.74 mmol) acetic anhydride, and 14 mL ODE were degassed for one hour at 110 °C. Then, 1 mL of a 0.19 M Se-ODE solution was injected under a nitrogen atmosphere. After the injection, the synthesis was heated to 240 °C and kept there for 10 min. After 10 minutes, the flask was rapidly cooled down, and 1 mL of OA was added at 80 °C.

8.3.1.5 Synthesis of CdSe NPL without Cd(OAc)₂ and using AcOH

In a three-neck flask, 38 mg (0.3 mmol) CdO, 285 μL (0.9 mmol) OA, and 39 mL ODE were heated to 240 °C and kept there for 10 min. During this time, the brown suspension turned into a colorless solution. The mixture was cooled down to 110 °C and degassed for 30 min to one hour. After cooling down the mixture to RT, 1 mL of a 0.19 M Se-ODE solution was injected under a nitrogen atmosphere. Then, the mixture was degassed again for another 10 to 30 min. After degassing, 11 μL (0.19 mmol) of AcOH was added to the mixture and stirred for 30 min under nitrogen flow.

Then, the synthesis was conducted at 240 °C for 10 min before rapidly cooling down the mixture to obtain CdSe NPL.

In another approach, 35 μL (0.60 mmol) AcOH was added instead of the 11 μL (0.19 mmol) AcOH. After the addition of a higher amount of AcOH, the mixture turned into a colorless turbid solution within a few minutes.

It was also possible to use 19 mL ODE instead of 39 mL.

8.3.1.6 Reactor precursor synthesis

This approach was similar to the method mentioned in Chapter 9.3.1.4 with minor adjustments. The mentioned amounts were multiplied by a factor of 2.5, 5, or 7. This also impacts the degassing and heating times. For the first step, the mixture was heated to 240 °C for one hour to obtain a colorless and clear solution. The degassing step lasted then for one to two hours. After adding the Se-ODE solution, the second degassing step lasted at least 30 min. Then, the mixture was stored under nitrogen until the flow reactor synthesis happened. On the day of the flow reactor synthesis, the AcOH was added to the mixture. The 30 min stirring time remained before the synthesis in the flow reactor.

8.3.1.7 Flow reactor setup

A schematic illustration of the complete flow reactor setup is shown in Figure 43. The flow reactor was built by Robert Seher.^{137,142} A few modifications have been made to this setup. The syringe pumps (NEMESYS mid-pressure modules, CETONI) had two openings which acted as a one-way system (Figure 43b): One inlet to fill up the syringe pump and one outlet to empty the syringe pump. The inlet had 1/16 inch of Polyether ether ketone (PEEK) tubing screwed into it with PEEK ferrules. This PEEK tube could be put into the flask with the flow reactor precursor (Figure 43a). The two syringe pumps had built-in pressure sensors. These pressure sensors enabled observation of possible clogging in the flow reactor. Each syringe pump was connected to a self-built titanium oven (Figure 43c). This connection between the syringe pump and the oven was made with tubes, ferrules, unions, and nuts, which were either made of PEEK or titanium. All components fitted the tubes with 1/16 inches out of PEEK and titanium. The ovens had a length of 10 cm, 30 cm, 90 cm, or 5 m and could be switched out depending on the desired flow rate and thus residue time in the ovens. Every oven had an inlet for a heating cartridge by HS-Heizelemente. The heating cartridge was connected to an Elotech R2500 temperature controller with 16 zones. This controller monitors and set the temperature of many heating cartridges connected to the device. It also allowed the heating rate to be controlled. A titanium heat exchanger was located behind each oven (Figure 43d). This heat exchanger was connected to a chiller, Julabo F25-MC. The water temperature was set to 20 °C. A hot fluid within the inner part of the heat exchanger could thus be quickly cooled down because the chilled water was pumped through the outer parts of the heat exchanger. PEEK tubes connected the two heat exchangers to a T-piece. This PEEK T-piece was connected to an optical flow cell by Knauer (Figure 43e). The flow cell had a path length of 3 mm and contains quartz glass windows. Optical fibers connect the flow cell to a UV/Vis spectrometer by Tec5. A PC was connected to the UV/Vis spectrometer and the syringe pumps. The program MultiSpec Pro 2 allowed the measurement of absorbance spectra in the flow cell, while the program QMix Elements controlled the syringe pump volume and flow rate. QMix Elements also allowed the pressure of the syringe pumps to be monitored. In the end, more PEEK-Tube was used to collect samples (Figure 43f).

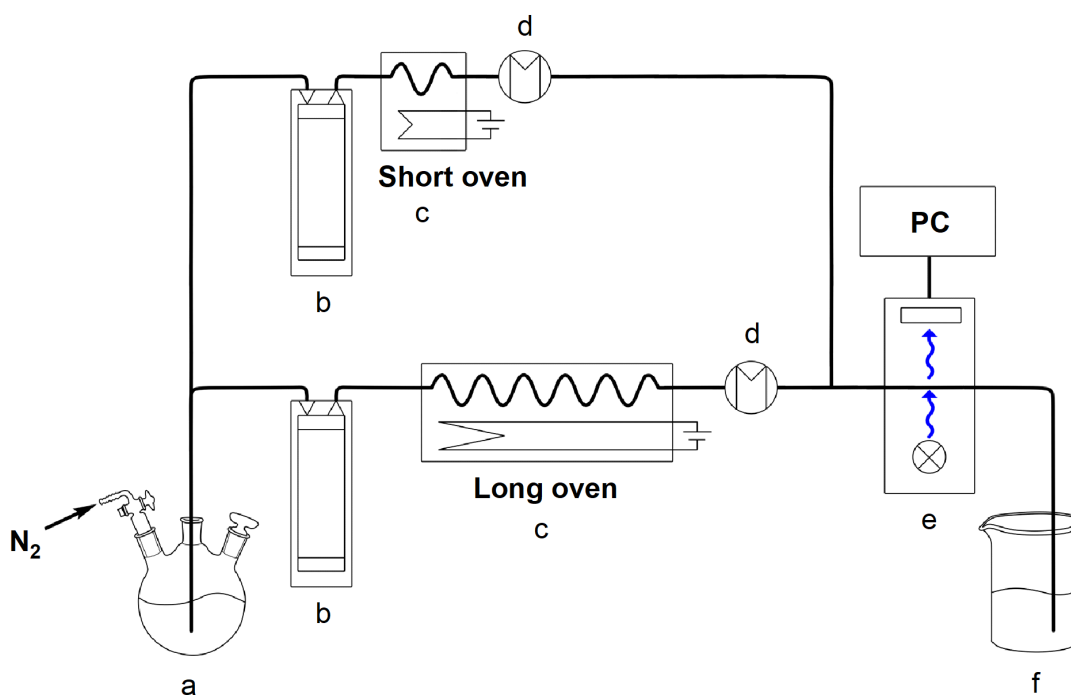


Figure 43: Schematic illustration of the flow reactor setup. The precursor (a) was connected to the syringe pumps (b). Each syringe pump was connected to an oven with a different length (c). Behind the oven, a heat exchanger was placed (d). Both heat exchangers were now connected to one optical flow cell, which enables *in situ* absorbance spectroscopy (e). The sample could be collected behind the optical flow cell (f). Figure by Funk et al. with slight modifications used with permission and under creative common license.⁹⁷

8.3.1.8 Synthesis of CdSe NPL in a flow reactor

At first, the flow reactor setup was flooded with *n*-hexane to check the system for possible leaks. Next, the system was purged with ODE to measure reference spectra with the *in situ* absorbance spectrometer. These recordings acted as the baseline for the *in situ* absorbance measurements. Then, the system was flooded with the reactor precursor solution. Now, the first spectra of the unreacted precursor solution were recorded. After the syringe pump was filled with a total volume of 25 mL, the synthesis was conducted as follows: The syringe pumps were set to the desired flow rate with the NEMESYS QMIX program, and the reactor oven was heated to the desired temperature. After the first residue time of the sample had passed in the flow reactor, *in situ* absorbance spectra were recorded. This applied to all the samples. While the absorbance spectra were recorded, samples were collected with glass vials at the end of the flow reactor. When all spectra were recorded and the sample was collected, the flow reactor settings were adjusted, and the steps were repeated. In the end, when the syringe pumps were close to being empty, or all samples had been collected, the heat cartridges

were turned off, and the oven cooled down to room temperature while the remaining precursor solution was pumped through the flow reactor system.

8.3.1.9 Cleaning of the flow reactor after the CdSe NPL synthesis

The cleaning of the flow reactor after the CdSe NPL synthesis was a crucial step which always happened after the synthesis was conducted. Cadmium acetate was forming over time in the reactor precursor solution, hence a proper cleaning was needed to avoid its residue in the flow reactor system. Another reason was that the anisotropic CdSe NPLs can clog the flow reactor system if they grew large enough and agglomerated.

The first step was to flood the entire system with *n*-hexane. Next, ethanol or isopropanol were used to flood the flow reactor system, followed up by water. Now, a 1 M HCl-solution was used to free the flow reactor from any remaining CdSe NPLs. Next, a 3 M TWEEN 60-water solution was purged through the flow reactor system. Finally, the flow reactor was flooded multiple times with water.

The flow reactor system was purged again with ethanol or isopropanol, then with *n*-hexane, and finally with ODE to conduct new experiments.

8.3.1.10 Purification of the raw CdSe NPL product

The procedure for purifying the raw CdSe NPL product was the same as that for the flow reactor and flask products. In a centrifuge tube, 7 mL of the raw CdSe NPL product, 6 mL *n*-hexane, and 6 mL EtOH were centrifuged for 10 min at 7000 g and RT. The supernatant was discarded. 10 mL *n*-hexane and 5 mL EtOH were added to the precipitate and sonicated. The slightly turbid yellow liquid was centrifuged again at 7000 g, RT for 10 min. Hopefully clear in color, the supernatant was discarded. 5 mL of *n*-hexane was added to the precipitate to obtain a purified sample of CdSe NPL in *n*-hexane.

This sample could also be diluted more with 14 mL instead of 5 mL *n*-hexane. For the stabilization of the particles, 1 mL OA was additionally added. This dilution was used to prepare for the CdSe/CdS core/shell growth experiments.

If the supernatant was still very yellow at the second centrifugation step, it was transferred to a new centrifuge tube. At this point, a few drops of MeOH were added until the yellow liquid became turbid again. Then, the supernatant was centrifuged at 7000 g, RT for 10 min. Both precipitates were combined with *n*-hexane to obtain a CdSe NPL sample in *n*-hexane with a total volume of 5 mL.

8.3.1.11 Cd(oleate)₂-ODE-solution for CdSe/CdS core-shell NPL synthesis

To prepare the Cd(oleate)₂-ODE-solution, 128 mg (0.99 mmol) CdO, 637 mg (2.26 mmol) OA and 10 mL of ODE were degassed for 30 min at 80 °C. Afterward, the brownish mixture was heated to 240 °C and kept there for 2.5 hours until a colorless, clear solution was obtained. The mixture was cooled down to room temperature and stored under a nitrogen atmosphere. Following these steps, a 0.1 M Cd(oleate)₂-ODE-solution was obtained.

8.3.1.12 1-Octanthiol-ODE-solution for CdSe/CdS core-shell NPL synthesis

To a total volume of 9 mL ODE, 63 µL (0.36 mmol) 1-octanthiol was added. This mixture was purged with nitrogen for 30 min before being stored under a nitrogen atmosphere.

8.3.1.13 CdSe/CdS core-shell NPL synthesis

The Riedinger et al. high-temperature shell growth method was used.³¹ At first, the *n*-hexane needed to be removed from the purified CdSe NPL solution. In a centrifuge tube, 5 mL of the purified CdSe NPL solution and 5 mL EtOH were centrifuged at 9000 g for 10 min. The supernatant was discarded. 50 µL (0.16 mmol) OA and 12.5 mL ODE were added to the precipitate and sonicated to obtain a yellow liquid. The yellow liquid was transferred to a three-neck flask with 504 µL of the 0.1 M Cd(oleate)₂-ODE-solution. Then, the mixture was first purged with nitrogen for 30 min at 80 °C, following a degassing step at the same temperature for 30 min. After that, the mixture was heated to 300 °C. Once the temperature increased, 1 mL of oleylamine was added to the mixture. At 180 °C, 0.6 mL of the 1-octanthiol-ODE-solution was injected with a flow rate of 3 mL per hour. Once the entire 1-octanthiol-ODE-solution was injected, the mixture was kept at 300 °C for an additional 10 min. After the 10 min were over, the flask was rapidly cooled down. At 60 °C, 10 mL of *n*-hexane and 1 mL of OA were added.

8.3.1.14 Purification of the raw CdSe/CdS core-shell NPL product.

The purification method presented here followed the same procedure as the purification method of the high-temperature shell growth purification method by Riedinger.³¹ In a centrifuge tube, the entire raw CdSe/CdS core-shell NPL liquid was centrifuged at 4830 g for 7 min. After this, the supernatant was discarded, and 10 mL *n*-hexane and 20 mL ethyl acetate were added to the precipitate. The mixture was centrifuged at 8000 g for 7 min. Once again, the supernatant was discarded, and 5 mL *n*-hexane was added to the precipitate.

8.3.1.15 Encapsulation method of CdSe NPL in polystyrene – PI-b-PEO shell

Here, our seeded emulsion polymerization method was used.^{63,65,143} At first, 1 mL of the purified CdSe NPL liquid with a total volume of 2 mL *n*-hexane was centrifuged with 3 mL EtOH

at 10000 g for 12 min to precipitate them. In the meantime, 200 mg PI-b-PEO ($M = 15000$ g/mol) was dissolved in 1 mL THF with a sonication bath. This amount equaled a polymer excess of 12000 per particle. The PI-b-PEO solution in THF was being added to the precipitated CdSe NPL. To prevent aggregation, the NPL liquid was being filtered with a $0.45\ \mu\text{m}$ PTFE syringe filter. At the end of the filter process, THF was used to flush the filter and thus ensure a high yield of the NPL liquid. However, the final volume of the NPL-THF liquid was not exceeding 3 mL. For the phase transfer of the NPL-THF liquid into water, NEMESYS syringe pumps by Cetoni were used, which can be controlled by a computer. The syringe pump system here featured two syringe pumps, each having a volume of 25 mL. Then, there was a third syringe pump with a total volume of 6 mL. The syringe pumps were connected with each other through an interdigital micromixer out of titanium (by Micro4industries).¹⁴⁴ Prior to the experiment, the third syringe pump was purged with THF. The two syringe pumps with a volume of 25 mL were filled with bidistilled Water. Into the third syringe pump came the NPL-THF liquid. For the conduction of the NPL phase transfer, the flow rate of each water syringe was set to 7.2 mL per minute, adding up to a total water flow rate of 14.4 mL per minute. The syringe pump filled with the NPL-THF liquid had a flow rate of 1.6 mL per minute. After the entire NPL-THF liquid had been transferred into the water, the remaining THF was removed by heating the solution to $80\ ^\circ\text{C}$ and purging it with nitrogen. Once the THF was removed, the NPL-water mixture was cooled down to RT. At RT, $54\ \mu\text{L}$ styrene was added to the mixture. While the NPL-water liquid stirred for 25 min, another solution was prepared consisting of 70 mg AIBN dissolved in 1 mL bidistilled Water and 0.5 mL of THF. Once the 25 min was over, the AIBN solution was added to the NPL-water mixture, and everything was kept at $80\ ^\circ\text{C}$ for at least 8 hours to complete the emulsion polymerization.

After the complete emulsion polymerization, the encapsulated NPL-water liquid was concentrated using the Sartorius® filter centrifuge tubes. The filters had a Molecular Weight Cut Off (MWCO) of 300000. Multiple times, the filter centrifuge tube with the NPL-water liquid was centrifuged at 4000 g for 12 min until a final volume of roughly 2 mL was obtained.

Now, a glycerol gradient was prepared to purify the encapsulated NPLs.⁶⁸ Three glycerol-water solutions with different concentrations were prepared. One solution contained 80 vol% glycerol, the other 15 vol%, and the final one consisted of 3 vol% glycerol. In a 50 mL centrifuge tube, the glycerol gradient was created by putting 7 mL of the 80 vol% glycerol solution at the bottom, followed by 12 mL of the 15 vol% glycerol solution in the middle, and on top, 5 mL of the 3 vol% glycerol was added. On the glycerol gradient, the concentrated encapsulated NPL-

water mixture was carefully added. The loaded glycerol gradient was centrifuged at 10 °C and 4000 g for one hour. After centrifugation, the encapsulated CdSe NPLs appear in a yellow color in the 15 vol% glycerol-solution, above the 80 vol% glycerol-solution.

The encapsulated CdSe NPLs were rinsed multiple times with bidistilled water using the filter centrifuge tubes with a MWCO of 300000 to remove the remaining glycerol.

8.3.2 Characterization

8.3.2.1 *In situ* absorbance spectroscopy

As mentioned in Section 8.3.1.7, the flow reactor setup contained a flow cell that was connected to a UV/Vis spectrometer. The flow cell had a pathway of 3 mm and quartz glass windows. Within the program MultiSpec Pro 2, different configurations could be made. The program allowed us to specifically record a reference spectrum, as well as the dark current background of the reference sample. It was also possible to set time intervals for the absorbance measurements.

For the flow reactor measurements, a reference spectrum and dark current background was measured by purging the flow reactor system with ODE. The reactor precursor solution was measured afterwards at room temperature, followed by the other samples at high temperatures and different residue times. Every sample was being collected at the end of the flow reactor after one residue time of the sample had passed within the flow reactor system.

Normalization of the absorbance spectra was performed in relation to the intensity at 300 nm.

8.3.2.2 *Ex situ* UV/Vis spectroscopy

For all *ex situ* UV/Vis spectroscopy experiments, quartz glass cuvettes with a path length of 1 cm had been used.

Measurements of the purified CdSe NPL from flask experiments were conducted as follows: A few μL of the purified CdSe NPL sample were added to the cuvette, and the sample was further diluted with *n*-hexane to obtain an optical density of around 0.1 in the absorbance spectra. The flow reactor samples were usually diluted 1:4 in *n*-hexane to ensure comparability between these samples. In the case of the encapsulated CdSe NPL, bidistilled water was used to dilute and prepare the samples for the UV/Vis spectroscopy characterization.

Prior to the absorbance spectroscopy of the samples reference spectra were measured of the pure organic solutions. For the diluted CdSe NPLs samples, *n*-hexane was the reference thus for undiluted flow reactor samples ODE was used.

Absorbance spectra were taken in a Cary 50 UV/Vis spectrometer in a range from 250 to 800 nm and an integration time of 0.1 s. The very same cuvette was also measured in a Fluoromax-4 spectrofluorometer. For the excitation spectra, the entrance and exit bandpass slits were set to 2 nm. The excitation range of the laser was set from 325 to 445 nm with an integration time of 0.1 s. For the emission spectra, the range varied between CdSe MSCs and CdSe NPL samples. In the case of CdSe MSCs samples, the laser excitation was set to 350 nm, and the measurement ranged from 365 nm to 690 nm. For the CdSe NPL and CdSe/CdS NPL, the laser excitation was set to 435 nm, and the range was set from 450 to 700 nm. Normalization of the absorbance spectra was performed at 300 nm.

The emission was sometimes also recorded in the Fluorotime 300 fluorescence lifetime spectrometer. Here, the settings were the same as the Fluoromax-4 emission settings.

Fluorescent dyes were used to determine the quantum yield of some samples. A quartz glass cuvette with Coumarin 153 in EtOH was prepared to obtain an optical density of 0.1 in its absorbance spectrum. For the CdSe/CdS core-shell NPL, Rhodamine 6G in EtOH was used. Similar to before, the optical density was set to 0.1 for the Rhodamine 6G. For these fluorescent dyes, a reference spectrum of pure EtOH was taken prior to their absorbance measurements.

8.3.2.3 Fluorescence lifetime

The fluorescence lifetimes were recorded using a Picoquant Fluorotime 300 fluorescence lifetime spectrometer. The same sample preparation from Chapter 9.3.2.2 was used.

The laser was set to the excitation maximum of the NPLs. For 3 ML CdSe NPLs with a low quantum yield and a large lateral size, a wavelength of 435 nm was chosen. The monochromator was set to 463 nm, equaling the emission of 3 ML CdSe NPLs. Furthermore, the laser power was set to 100 %, with a repetition rate of 2.8 MHz and a bandwidth of 2.7 nm. Finally, all spectra were recorded with an integration time of 0.1 s per point. In case of a pile-up in the lifetime spectra, the repetition rate was lowered.

For all fluorescence lifetime measurements, an instrument response function (IRF) was measured.⁸⁰

8.3.2.4 TEM

TEM samples were prepared by using copper grids with a thin graphene film on one side. The diluted samples from Chapter 8.3.2.2 were used. From the diluted samples, 8 μL were dropped onto the copper grid with the thin graphene film. The drop stayed onto the grid for 1 minute before the excess solution was carefully removed with a filter paper. Then, the TEM grid was left to dry at room temperature for at least 24 hours.

All TEM measurements were conducted by Stefan Werner and Andrea Köppen from the chemistry department TEM team under the leadership of Dr. Charlotte Ruhmlieb.

The JEM 1011 electron microscope by JEOL had an acceleration voltage of 100 kV for TEM measurements. As a cathode to produce the electron beam, LaB_6 was used and a SIS CCD camera system was used with a resolution of 1376 x 1032 pixels. The camera constant for the SAED-data varied depending on the experimental setup.

The other microscope, the JEM 2200 FS by JEOL, had an acceleration voltage of 200 kV for the TEM measurements. A field emission gun created the electron beam in this electron microscope.

8.3.2.5 SAXS measurements

For the SAXS measurements, quartz glass capillaries were used with a length of 80 mm, a wall thickness of 0.01 mm, and an outer diameter of 2.0 mm or 1.0 mm were used.

The quartz glass capillaries were filled with the unpurified flow reactor precursors using syringes. One quartz glass capillary was filled with pure ODE for a reference measurement. The filled capillaries were sealed by using hot glue.

All the SAXS measurements were performed by Dr. Benedikt Sochor at the beamline P03 (PETRA III) at the DESY campus in Hamburg. An X-ray radiation of 1.023 Å was used to conduct the experiment. As a scattering detector, a PILATUS 2M Detector system was used with a distance of 39.1 m to the sample. For every measurement, the capillary was scanned in a range of 50 mm with a step size of 0.1 mm and a time of 0.1 s per step. The obtained data was averaged and modeled using SasView. As fitting modes, a combination of the spherical form and parallelepiped was used.

8.3.2.6 Powder XRD measurements

For powder XRD measurements, only purified samples were used. For preparation of the samples for powder XRD measurement, 17 μL of the sample was drop cast onto a silicon wafer.

After the drop dried completely, the sample was drop-casted again on the same spot. This cycle continued until the sample built up visibly on the silicon wafer with color. To get this kind of build-up it was necessary to use 5 or 6 drops.

Reference crystal structures of CdSe were obtained using the Materials Project archive to evaluate the obtained XRD data.¹²⁰ The measurement settings were simulated on these reference crystal structures to obtain XRD Data of these references using Mercury and converted to an Excel file using PowDLL.

All XRD measurements were conducted by Nina Schober from the chemistry department XRD team, who is also a member of the Bigall group. The X'Pert PRO X-ray diffractometer by Philips was used with a Copper K α radiation of 1.541 Å for K α 1 and 1.544 Å for K α 2. This X-ray beam operated at 45 kV and 40 mA. For the measurements, a step size of 0.033 ° was used in a range between 5 and 90 °.

8.3.2.7 Residence time experiments in the flow reactor

A tracer needed to be prepared to measure the residence time in the flow reactor.

7 mg of Coumarin 153 was dissolved in 10 mL acetone. From this prepared Coumarin solution, 500 μ L were taken and added to 150 mL ODE. ODE was used because it was the main solvent for the flow reactor synthesis (see Chapter 9.3.1.6).

The flow reactor was flooded with ODE, and a reference spectrum of ODE was measured using the built-in spectrometer. Then, the syringe pumps were filled with the tracer solution. With a set flow rate, every 20 seconds, an absorption spectrum was recorded until the tracer reached a constant value in the spectrometer.

9 List of references

References

- (1) Thakur, A.; Thakur, P.; Khurana, S. P., Eds. *Synthesis and Applications of Nanoparticles*, 1st ed. 2022; Springer Nature Singapore; Imprint Springer, 2022. DOI: 10.1007/978-981-16-6819-7.
- (2) Rute Neves, A. *Nanoparticles in Life Sciences and Biomedicine*, 1st ed.; Pan Stanford Publishing, 2018.
- (3) Gopinath, S. C. B. *Nanoparticles in Analytical and Medical Devices*; Elsevier, 2020.
- (4) Divsar, F., Ed. *Quantum Dots: Fundamental and Applications*; IntechOpen, 2020. DOI: 67502.
- (5) Gangula, A. *Point-Of-Care Testing of COVID-19: Current Status, Clinical Impact, and Future Therapeutic Perspectives*, 1st ed.; SpringerBriefs in Applied Sciences and Technology Series; Springer, 2022.
- (6) Thanh, N. T. K.; Maclean, N.; Mahiddine, S. Mechanisms of nucleation and growth of nanoparticles in solution. *Chemical reviews* **2014**, *114* (15), 7610–7630. DOI: 10.1021/cr400544s. Published Online: Jul. 8, 2014.
- (7) *Nanotechnology and microelectronics: Global diffusion, economics and policy*, IGI Global; IGI Global (701 E. Chocolate Avenue Hershey Pennsylvania 17033 USA), 2010. DOI: 10.4018/978-1-61692-006-7.
- (8) Laudon, M.; Romanowicz, B., Eds. *TechConnect briefs 2016*, Vol. 3; TechConnect, 2016.
- (9) Riedinger, A.; Ott, F. D.; Mule, A.; Mazzotti, S.; Knuesel, P. N.; Kress, S. J. P.; Prins, F.; Erwin, S. C.; Norris, D. J. How semiconductor nanoplatelets form **2016**. DOI: 10.48550/arXiv.1605.06553.
- (10) Riedinger, A.; Ott, F. D.; Mule, A.; Mazzotti, S.; Knüsel, P. N.; Kress, S. J. P.; Prins, F.; Erwin, S. C.; Norris, D. J. An intrinsic growth instability in isotropic materials leads to quasi-two-dimensional nanoplatelets. *Nature materials* **2017**, *16* (7), 743–748. DOI: 10.1038/NMAT4889. Published Online: Apr. 3, 2017.
- (11) Chen, Y.; Chen, D.; Li, Z.; Peng, X. Symmetry-Breaking for Formation of Rectangular CdSe Two-Dimensional Nanocrystals in Zinc-Blende Structure. *Journal of the American Chemical Society* **2017**, *139* (29), 10009–10019. DOI: 10.1021/jacs.7b04855. Published Online: Jul. 17, 2017.
- (12) Atkins, P. W.; Paula, J. de; Keeler, J. J. *Atkins' physical chemistry*, Twelfth edition; Oxford University Press, 2023.

- (13) Mello Donegá, C., Ed. *Nanoparticles: Workhorses of nanoscience*; Material science/chemistry; Springer, 2014.
- (14) Scholes, G. D.; Rumbles, G. Excitons in nanoscale systems. *Nature materials* **2006**, *5* (9), 683–696. DOI: 10.1038/nmat1710.
- (15) Kuno, M. *Introductory nanoscience: Physical and chemical concepts*; GS Garland Science, 2011.
- (16) Zhang, Y.; Liu, Y.; Li, C.; Chen, X.; Wang, Q. Controlled Synthesis of Ag₂S Quantum Dots and Experimental Determination of the Exciton Bohr Radius. *J. Phys. Chem. C* **2014**, *118* (9), 4918–4923. DOI: 10.1021/jp501266d.
- (17) Ashby, M. F.; Ferreira, P. J.; Schodek, D. *Nanomaterials, nanotechnologies and design: An introduction for engineers and architects*; Butterworth Heinemann, 2009.
- (18) Hens, Z.; Delerue, C. D. A tight-binding model for illustrating exciton confinement in semiconductor nanocrystals. *The Journal of chemical physics* **2024**, *160* (11). DOI: 10.1063/5.0192031.
- (19) Efros, A. L.; Brus, L. E. Nanocrystal Quantum Dots: From Discovery to Modern Development. *ACS nano* **2021**, *15* (4), 6192–6210. DOI: 10.1021/acsnano.1c01399. Published Online: Apr. 8, 2021.
- (20) Spittel, D.; Poppe, J.; Meerbach, C.; Ziegler, C.; Hickey, S. G.; Eychmüller, A. Absolute Energy Level Positions in CdSe Nanostructures from Potential-Modulated Absorption Spectroscopy (EMAS). *ACS nano* **2017**, *11* (12), 12174–12184. DOI: 10.1021/acsnano.7b05300. Published Online: Dec. 1, 2017.
- (21) Tong, X. *Core/Shell Quantum Dots: Synthesis, Properties and Devices*; Lecture Notes in Nanoscale Science and Technology Ser, v.28; Springer International Publishing AG, 2020.
- (22) Ithurria, S.; Dubertret, B. Quasi 2D colloidal CdSe platelets with thicknesses controlled at the atomic level. *J. Am. Chem. Soc.* **2008**, *130* (49), 16504–16505. DOI: 10.1021/ja807724e.
- (23) Klimov, V. I., Ed. *Nanocrystal quantum dots*, Second edition; CRC Press Taylor & Francis Group, 2010.
- (24) Hunklinger, S.; Enss, C. *Festkörperphysik*, 6. Auflage; De Gruyter Studium; De Gruyter Oldenbourg, 2023. DOI: 10.1515/9783111027227.
- (25) Manfra, M. J.; Pfeiffer, L. N.; West, K. W.; Picciotto, R. de; Baldwin, K. W. High mobility two-dimensional hole system in GaAs/AlGaAs quantum wells grown on (100) GaAs substrates. *Applied Physics Letters* **2005**, *86* (16). DOI: 10.1063/1.1900949.

- (26) Katz, D.; Wizansky, T.; Millo, O.; Rothenberg, E.; Mokari, T.; Banin, U. Size-dependent tunneling and optical spectroscopy of CdSe quantum rods. *Physical review letters* **2002**, *89* (8), 86801. DOI: 10.1103/PhysRevLett.89.086801. Published Online: Jul. 31, 2002.
- (27) Castro, N.; Bouet, C.; Ithurria, S.; Lequeux, N.; Constantin, D.; Levitz, P.; Pontoni, D.; Abécassis, B. Insights into the Formation Mechanism of CdSe Nanoplatelets Using in Situ X-ray Scattering. *Nano letters* **2019**, *19* (9), 6466–6474. DOI: 10.1021/acs.nanolett.9b02687. Published Online: Aug. 27, 2019.
- (28) Ithurria, S.; Tessier, M. D.; Mahler, B.; Lobo, R. P. S. M.; Dubertret, B.; Efros, A. L. Colloidal nanoplatelets with two-dimensional electronic structure. *Nature materials* **2011**, *10* (12), 936–941. DOI: 10.1038/NMAT3145. Published Online: Oct. 23, 2011.
- (29) Yu, J.; Chen, R. Optical properties and applications of two-dimensional CdSe nanoplatelets. *InfoMat* **2020**, *2* (5), 905–927. DOI: 10.1002/inf2.12106.
- (30) Olutas, M.; Guzelurk, B.; Kelestemur, Y.; Yeltik, A.; Delikanli, S.; Demir, H. V. Lateral Size-Dependent Spontaneous and Stimulated Emission Properties in Colloidal CdSe Nanoplatelets. *ACS nano* **2015**, *9* (5), 5041–5050. DOI: 10.1021/acs.nano.5b01927. Published Online: May. 12, 2015.
- (31) Rossinelli, A. A.; Riedinger, A.; Marqués-Gallego, P.; Knüsel, P. N.; Antolinez, F. V.; Norris, D. J. High-temperature growth of thick-shell CdSe/CdS core/shell nanoplatelets. *Chemical communications (Cambridge, England)* **2017**, *53* (71), 9938–9941. DOI: 10.1039/c7cc04503d.
- (32) Piveteau, L.; Dirin, D. N.; Gordon, C. P.; Walder, B. J.; Ong, T.-C.; Emsley, L.; Copéret, C.; Kovalenko, M. V. Colloidal-ALD-Grown Core/Shell CdSe/CdS Nanoplatelets as Seen by DNP Enhanced PASS-PIETA NMR Spectroscopy. *Nano letters* **2020**, *20* (5), 3003–3018. DOI: 10.1021/acs.nanolett.9b04870. Published Online: Apr. 29, 2020.
- (33) Yang, H.; Xiang, W.; Zhao, X.; Ge, X.; Zhu, B.; Cui, Y.; Zhang, J. Size-dependent third-order optical nonlinearity in colloidal CdSe/CdS core/crown nanoplatelets with quasi-type II band-structure. *Optics & Laser Technology* **2022**, *156*, 108615. DOI: 10.1016/j.optlas-tec.2022.108615.
- (34) Schlosser, A.; Graf, R. T.; Bigall, N. C. CdS crown growth on CdSe nanoplatelets: core shape matters. *Nanoscale Adv.* **2020**, *2* (10), 4604–4614. DOI: 10.1039/d0na00619j.
- (35) LaMer, V. K.; Dinegar, R. H. Theory, Production and Mechanism of Formation of Monodispersed Hydrosols. *J. Am. Chem. Soc.* **1950**, *72* (11), 4847–4854. DOI: 10.1021/ja01167a001.

- (36) Murray, C. B.; Norris, D. J.; Bawendi, M. G. Synthesis and characterization of nearly monodisperse CdE (E = sulfur, selenium, tellurium) semiconductor nanocrystallites. *J. Am. Chem. Soc.* **1993**, *115* (19), 8706–8715. DOI: 10.1021/ja00072a025.
- (37) Peng, X.; Manna, L.; Yang, W.; Wickham, J.; Scher, E.; Kadavanich, A.; Alivisatos, A. P. Shape control of CdSe nanocrystals. *Nature* **2000**, *404* (6773), 59–61. DOI: 10.1038/35003535.
- (38) Manna, L.; Scher, E. C.; Alivisatos, A. P. Synthesis of Soluble and Processable Rod-, Arrow-, Teardrop-, and Tetrapod-Shaped CdSe Nanocrystals. *J. Am. Chem. Soc.* **2000**, *122* (51), 12700–12706. DOI: 10.1021/ja003055%2B.
- (39) Joo, J.; Son, J. S.; Kwon, S. G.; Yu, J. H.; Hyeon, T. Low-temperature solution-phase synthesis of quantum well structured CdSe nanoribbons. *J. Am. Chem. Soc.* **2006**, *128* (17), 5632–5633. DOI: 10.1021/ja0601686.
- (40) Schliehe, C.; Juarez, B. H.; Pelletier, M.; Jander, S.; Greshnykh, D.; Nagel, M.; Meyer, A.; Foerster, S.; Kornowski, A.; Klinke, C.; Weller, H. Ultrathin PbS sheets by two-dimensional oriented attachment. *Science (New York, N.Y.)* **2010**, *329* (5991), 550–553. DOI: 10.1126/science.1188035.
- (41) Liu, Y.-H.; Wang, F.; Wang, Y.; Gibbons, P. C.; Buhro, W. E. Lamellar assembly of cadmium selenide nanoclusters into quantum belts. *Journal of the American Chemical Society* **2011**, *133* (42), 17005–17013. DOI: 10.1021/ja206776g. Published Online: Sep. 29, 2011.
- (42) Wang, F.; Wang, Y.; Liu, Y.-H.; Morrison, P. J.; Loomis, R. A.; Buhro, W. E. Two-dimensional semiconductor nanocrystals: properties, templated formation, and magic-size nanocluster intermediates. *Accounts of chemical research* **2015**, *48* (1), 13–21. DOI: 10.1021/ar500286j. Published Online: Dec. 9, 2014.
- (43) Chen, X.; Ge, J.; Xiao, P.; Deng, Y.; Wang, Y. Ligand-induced, magic-size clusters enabled formation of colloidal all-inorganic II–VI nanoplatelets with controllable lateral dimensions. *Nano Res.* **2023**, *16* (2), 3387–3394. DOI: 10.1007/s12274-022-5210-9.
- (44) Nicolo Castro; Cécile Bouet; Sandrine Ithurria; Nicolas Lequeux; Doru Constantin; Pierre Levitz; Diego Pontoni; Benjamin Abécassis. Insights into the Formation Mechanism of CdSe Nanoplatelets Using in Situ X-ray Scattering.
- (45) Mahler, B.; Nadal, B.; Bouet, C.; Patriarche, G.; Dubertret, B. Core/shell colloidal semiconductor nanoplatelets. *J. Am. Chem. Soc.* **2012**, *134* (45), 18591–18598. DOI: 10.1021/ja307944d. Published Online: Nov. 1, 2012.
- (46) Christodoulou, S.; Climente, J. I.; Planelles, J.; Brescia, R.; Prato, M.; Martín-García, B.; Khan, A. H.; Moreels, I. Chloride-Induced Thickness Control in CdSe Nanoplatelets. *Nano*

letters **2018**, *18* (10), 6248–6254. DOI: 10.1021/acs.nanolett.8b02361. Published Online: Sep. 7, 2018.

(47) Meerbach, C.; Wu, C.; Erwin, S. C.; Dang, Z.; Prudnikau, A.; Lesnyak, V. Halide-Assisted Synthesis of Cadmium Chalcogenide Nanoplatelets. *Chem. Mater.* **2020**, *32* (1), 566–574. DOI: 10.1021/acs.chemmater.9b04438.

(48) Cho, W.; Kim, S.; Coropceanu, I.; Srivastava, V.; Diroll, B. T.; Hazarika, A.; Fedin, I.; Galli, G.; Schaller, R. D.; Talapin, D. V. Direct Synthesis of Six-Monolayer (1.9 nm) Thick Zinc-Blende CdSe Nanoplatelets Emitting at 585 nm. *Chem. Mater.* **2018**, *30* (20), 6957–6960. DOI: 10.1021/acs.chemmater.8b02489.

(49) Ott, F. D.; Riedinger, A.; Ochsenein, D. R.; Knüsel, P. N.; Erwin, S. C.; Mazzotti, M.; Norris, D. J. Ripening of Semiconductor Nanoplatelets. *Nano letters* **2017**, *17* (11), 6870–6877. DOI: 10.1021/acs.nanolett.7b03191. Published Online: Oct. 17, 2017.

(50) Herron, N.; Suna, A.; Wang, Y. Synthesis of ≈ 10 Å thiophenolate-capped CdS clusters. Observation of a sharp absorption peak. *J. Chem. Soc., Dalton Trans.* **1992** (15), 2329–2335. DOI: 10.1039/DT9920002329.

(51) Serena Busatto and Celso de Mello Donega. Magic-Size Semiconductor Nanostructures: Where Does the Magic Come from?

(52) Singh, V.; Priyanka; More, P. V.; Hemmer, E.; Mishra, Y. K.; Khanna, P. K. Magic-sized CdSe nanoclusters: a review on synthesis, properties and white light potential. *Mater. Adv.* **2021**, *2* (4), 1204–1228. DOI: 10.1039/D0MA00921K.

(53) Andrew B. Pun, Sergio Mazzotti, Aniket S. Mule, and David J. Norris. Understanding Discrete Growth in Semiconductor Nanocrystals: Nanoplatelets and Magic-Sized Clusters.

(54) Trambouze, P.; Euzen, J.-P. *Chemical reactors: From design to operation*, New ed.; Institut français du pétrole publications; Editions Technip, 2004.

(55) Jess, A.; Wasserscheid, P. *Chemical technology: From principles to products*, Second edition; Wiley-VCH, 2020.

(56) Nauman, E. B. *Chemical reactor design, optimization, and scaleup: Extensive information on optimization and scaleup; reactor types and purposes; biochemicals and polymers*; Professional engineering; McGraw-Hill, 2002. DOI: 26699.

(57) Salmi, T.; Mikkola, J.-P.; Wärnå, J. P. *Chemical reaction engineering and reactor technology*, Second edition; Chemical industries; CRC Press, 2019.

(58) Stachowiak, G. *Engineering Tribology*, 3rd ed.; Elsevier Science & Technology, 2006.

(59) Schubert, H., Ed. *Handbuch der mechanischen Verfahrenstechnik: Partikeleigenschaften, Mikroprozesse, Makroprozesse, Schüttgut*; Wiley-VCH, 20XX-.

- (60) Reschetilowski, W., Ed. *Microreactors in preparative chemistry: Practical aspects in bioprocessing, nanotechnology, catalysis and more*; Wiley-VCH, 2013.
- (61) Carberry, J. J. *Chemical and catalytic reaction engineering*, 1. publ., unabridged, slightly corrected republ. of the work originally publ. in 1976 by McGraw-Hill; Dover books on chemistry; Dover, 2001.
- (62) Doğu, T.; Doğu, G. *Fundamentals of chemical reactor engineering: A multi-scale approach*; Wiley, 2022.
- (63) Kloust, H.; Pösel, E.; Kappen, S.; Schmidtke, C.; Kornowski, A.; Pauer, W.; Moritz, H.-U.; Weller, H. Ultrasmall biocompatible nanocomposites: a new approach using seeded emulsion polymerization for the encapsulation of nanocrystals. *Langmuir : the ACS journal of surfaces and colloids* **2012**, 28 (18), 7276–7281. DOI: 10.1021/la300231r. Published Online: Apr. 25, 2012.
- (64) Pösel, E.; Schmidtke, C.; Fischer, S.; Peldschus, K.; Salamon, J.; Kloust, H.; Tran, H.; Pietsch, A.; Heine, M.; Adam, G.; Schumacher, U.; Wagener, C.; Förster, S.; Weller, H. Tailor-made quantum dot and iron oxide based contrast agents for in vitro and in vivo tumor imaging. *ACS nano* **2012**, 6 (4), 3346–3355. DOI: 10.1021/nm300365m. Published Online: Apr. 6, 2012.
- (65) Kloust, H.; Schmidtke, C.; Feld, A.; Schotten, T.; Eggers, R.; Fittschen, U. E. A.; Schulz, F.; Pösel, E.; Ostermann, J.; Bastús, N. G.; Weller, H. In situ functionalization and PEO coating of iron oxide nanocrystals using seeded emulsion polymerization. *Langmuir : the ACS journal of surfaces and colloids* **2013**, 29 (15), 4915–4921. DOI: 10.1021/la400713p. Published Online: Apr. 5, 2013.
- (66) Kloust, H.; Schmidtke, C.; Merkl, J.-P.; Feld, A.; Schotten, T.; Fittschen, U. E. A.; Gehring, M.; Ostermann, J.; Pösel, E.; Weller, H. Poly(ethylene oxide) and Polystyrene Encapsulated Quantum Dots: Highly Fluorescent, Functionalizable, and Ultrastable in Aqueous Media. *J. Phys. Chem. C* **2013**, 117 (44), 23244–23250. DOI: 10.1021/jp4045836.
- (67) Schmidtke, C.; Pösel, E.; Ostermann, J.; Pietsch, A.; Kloust, H.; Tran, H.; Schotten, T.; Bastús, N. G.; Eggers, R.; Weller, H. Amphiphilic, cross-linkable diblock copolymers for multifunctionalized nanoparticles as biological probes. *Nanoscale* **2013**, 5 (16), 7433–7444. DOI: 10.1039/c3nr01520c.
- (68) Steinigeweg, D.; Schütz, M.; Salehi, M.; Schlücker, S. Fast and cost-effective purification of gold nanoparticles in the 20–250 nm size range by continuous density gradient centrifugation. *Small (Weinheim an der Bergstrasse, Germany)* **2011**, 7 (17), 2443–2448. DOI: 10.1002/sml.201100663. Published Online: Jun. 28, 2011.

- (69) Agnello, S., Ed. *Spectroscopy for materials characterization*; Wiley, 2021.
- (70) Luo, X.; Hu, R.; Liu, S.; Wang, K. Heat and fluid flow in high-power LED packaging and applications. *Progress in Energy and Combustion Science* **2016**, *56*, 1–32. DOI: 10.1016/j.pecs.2016.05.003.
- (71) Dou, H.; Yuan, C.; Zhu, R.; Li, L.; Zhang, J.; Weng, T.-C. Impact of Surface Trap States on Electron and Energy Transfer in CdSe Quantum Dots Studied by Femtosecond Transient Absorption Spectroscopy. *Nanomaterials (Basel, Switzerland)* **2023**, *14* (1). DOI: 10.3390/nano14010034. Published Online: Dec. 22, 2023.
- (72) Rao Singuru, M. M.; Sun, S.-C.; Chuang, M.-C. Advances in oligonucleotide-based detection coupled with fluorescence resonance energy transfer. *TrAC Trends in Analytical Chemistry* **2020**, *123*, 115756. DOI: 10.1016/j.trac.2019.115756.
- (73) Liu, J.; Guillemeney, L.; Abécassis, B.; Coolen, L. Long Range Energy Transfer in Self-Assembled Stacks of Semiconducting Nanoplatelets. *Nano letters* **2020**, *20* (5), 3465–3470. DOI: 10.1021/acs.nanolett.0c00376. Published Online: Apr. 24, 2020.
- (74) Sapsford, K. E.; Berti, L.; Medintz, I. L. Materials for fluorescence resonance energy transfer analysis: beyond traditional donor-acceptor combinations. *Angewandte Chemie (International ed. in English)* **2006**, *45* (28), 4562–4589. DOI: 10.1002/anie.200503873.
- (75) Rogach, A. L.; Klar, T. A.; Lupton, J. M.; Meijerink, A.; Feldmann, J. Energy transfer with semiconductor nanocrystals. *J. Mater. Chem.* **2009**, *19* (9), 1208–1221. DOI: 10.1039/B812884G.
- (76) Pramanik, G.; Humpolickova, J.; Valenta, J.; Kundu, P.; Bals, S.; Bour, P.; Dracinsky, M.; Cigler, P. Gold nanoclusters with bright near-infrared photoluminescence. *Nanoscale* **2018**, *10* (8), 3792–3798. DOI: 10.1039/C7NR06050E.
- (77) Rurack, K.; Spieles, M. Fluorescence quantum yields of a series of red and near-infrared dyes emitting at 600-1000 nm. *Analytical chemistry* **2011**, *83* (4), 1232–1242. DOI: 10.1021/ac101329h. Published Online: Jan. 20, 2011.
- (78) Zhang, Z.; Sun, H. Manipulation of the Optical Properties of Colloidal 2D CdSe Nanoplatelets. *Advanced Photonics Research* **2021**, *2* (8). DOI: 10.1002/adpr.202100045.
- (79) Sillen, A.; Engelborghs, Y. The Correct Use of “Average” Fluorescence Parameters. *Photochem & Photobiology* **1998**, *67* (5), 475–486. DOI: 10.1111/j.1751-1097.1998.tb09082.x.
- (80) Li, Y.; Natakorn, S.; Chen, Y.; Safar, M.; Cunningham, M.; Tian, J.; Li, D. D.-U. Investigations on Average Fluorescence Lifetimes for Visualizing Multi-Exponential Decays. *Front. Phys.* **2020**, *8*. DOI: 10.3389/fphy.2020.576862.

- (81) Sharma, S. K.; Verma, D. S.; Khan, L. U.; Kumar, S.; Khan, S. B., Eds. *Handbook of materials characterization*; Springer, 2018.
- (82) Williams, D. B.; Carter, C. B. *Transmission Electron Microscopy: A Textbook for Materials Science*, 2. ed.; Springer US, 2009. DOI: 10.1007/978-0-387-76501-3.
- (83) Ithurria, S.; Talapin, D. V. Colloidal atomic layer deposition (c-ALD) using self-limiting reactions at nanocrystal surface coupled to phase transfer between polar and nonpolar media. *J. Am. Chem. Soc.* **2012**, *134* (45), 18585–18590. DOI: 10.1021/ja308088d. Published Online: Nov. 1, 2012.
- (84) Mahler, B.; Guillemot, L.; Bossard-Giannesini, L.; Ithurria, S.; Pierucci, D.; Ouerghi, A.; Patriarche, G.; Benbalagh, R.; Lacaze, E.; Rochet, F.; Lhuillier, E. Metallic Functionalization of CdSe 2D Nanoplatelets and Its Impact on Electronic Transport. *J. Phys. Chem. C* **2016**, *120* (23), 12351–12361. DOI: 10.1021/acs.jpcc.6b02101.
- (85) Guzel Turk, B.; Erdem, O.; Olutas, M.; Kelestemur, Y.; Demir, H. V. Stacking in colloidal nanoplatelets: tuning excitonic properties. *ACS nano* **2014**, *8* (12), 12524–12533. DOI: 10.1021/nn5053734. Published Online: Dec. 11, 2014.
- (86) Bertrand, G. H. V.; Polovitsyn, A.; Christodoulou, S.; Khan, A. H.; Moreels, I. Shape control of zincblende CdSe nanoplatelets. *Chemical communications (Cambridge, England)* **2016**, *52* (80), 11975–11978. DOI: 10.1039/c6cc05705e.
- (87) Schlosser, A.; Meyer, L. C.; Lübke, F.; Miethe, J. F.; Bigall, N. C. Nanoplatelet cryoaerogels with potential application in photoelectrochemical sensing. *Physical chemistry chemical physics : PCCP* **2019**, *21* (18), 9002–9012. DOI: 10.1039/C9CP00281B.
- (88) Jiang, Y.; Ojo, W.-S.; Mahler, B.; Xu, X.; Abécassis, B.; Dubertret, B. Synthesis of CdSe Nanoplatelets without Short-Chain Ligands: Implication for Their Growth Mechanisms. *ACS omega* **2018**, *3* (6), 6199–6205. DOI: 10.1021/acsomega.8b01006. Published Online: Jun. 8, 2018.
- (89) Huang, X.; Parashar, V. K.; Ao, Z.; Gijs, M. A. M. Insight into the Growth of Anisotropic CdSe Nanocrystals: Attachment of Intrinsically Different Building Blocks. *J. Phys. Chem. C* **2020**, *124* (50), 27754–27762. DOI: 10.1021/acs.jpcc.0c07933.
- (90) Bouet, C.; Mahler, B.; Nadal, B.; Abecassis, B.; Tessier, M. D.; Ithurria, S.; Xu, X.; Dubertret, B. Two-Dimensional Growth of CdSe Nanocrystals, from Nanoplatelets to Nanosheets. *Chem. Mater.* **2013**, *25* (4), 639–645. DOI: 10.1021/cm304080q.
- (91) Delikanli, S.; Yu, G.; Yeltik, A.; Bose, S.; Erdem, T.; Yu, J.; Erdem, O.; Sharma, M.; Sharma, V. K.; Quliyeva, U.; Shendre, S.; Dang, C.; Zhang, D. H.; Sum, T. C.; Fan, W.;

- Demir, H. V. Ultrathin Highly Luminescent Two-Monolayer Colloidal CdSe Nanoplatelets. *Adv Funct Materials* **2019**, *29* (35). DOI: 10.1002/adfm.201901028.
- (92) Singh, S.; Tomar, R.; Brinck, S. ten; Roo, J. de; Geiregat, P.; Martins, J. C.; Infante, I.; Hens, Z. Colloidal CdSe Nanoplatelets, A Model for Surface Chemistry/Optoelectronic Property Relations in Semiconductor Nanocrystals. *J. Am. Chem. Soc.* **2018**, *140* (41), 13292–13300. DOI: 10.1021/jacs.8b07566. Published Online: Oct. 5, 2018.
- (93) Chen, D.; Gao, Y.; Chen, Y.; Ren, Y.; Peng, X. Structure Identification of Two-Dimensional Colloidal Semiconductor Nanocrystals with Atomic Flat Basal Planes. *Nano letters* **2015**, *15* (7), 4477–4482. DOI: 10.1021/acs.nanolett.5b00940. Published Online: Jun. 10, 2015.
- (94) Di Giacomo, A.; Rodà, C.; Khan, A. H.; Moreels, I. Colloidal Synthesis of Laterally Confined Blue-Emitting 3.5 Monolayer CdSe Nanoplatelets. *Chem. Mater.* **2020**, *32* (21), 9260–9267. DOI: 10.1021/acs.chemmater.0c03066. Published Online: Oct. 21, 2020.
- (95) Hutter, E. M.; Blatt, E.; Goris, B.; Pietra, F.; van der Bok, J. C.; Boneschanscher, M. P.; Mello Donegá, C. de; Bals, S.; Vanmaekelbergh, D. Conformal and atomic characterization of ultrathin CdSe platelets with a helical shape. *Nano letters* **2014**, *14* (11), 6257–6262. DOI: 10.1021/nl5025744. Published Online: Oct. 28, 2014.
- (96) Po, H.; Dabard, C.; Roman, B.; Reyssat, E.; Bico, J.; Baptiste, B.; Lhuillier, E.; Ithurria, S. Chiral Helices Formation by Self-Assembled Molecules on Semiconductor Flexible Substrates. *ACS nano* **2022**, *16* (2), 2901–2909. DOI: 10.1021/acsnano.1c09982. Published Online: Feb. 2, 2022.
- (97) Funk, J. I. M.; Sochor, B.; Koyiloth Vayalil, S.; Weller, H. Insights into the Formation of CdSe Nanoplatelets using a Flow Reactor†. *Nanoscale* **2024**. DOI: 10.1039/D4NR03804E.
- (98) Pelton, M. Carrier Dynamics, Optical Gain, and Lasing with Colloidal Quantum Wells. *J. Phys. Chem. C* **2018**, *122* (20), 10659–10674. DOI: 10.1021/acs.jpcc.7b12629.
- (99) Pedetti, S.; Ithurria, S.; Heuclin, H.; Patriarche, G.; Dubertret, B. Type-II CdSe/CdTe core/crown semiconductor nanoplatelets. *J. Am. Chem. Soc.* **2014**, *136* (46), 16430–16438. DOI: 10.1021/ja509307m. Published Online: Nov. 6, 2014.
- (100) Failla, M.; García Flórez, F.; Salzmann, B. B. V.; Vanmaekelbergh, D.; Stoof, H. T. C.; Siebbeles, L. D. A. Observation of the quantized motion of excitons in CdSe nanoplatelets. *Phys. Rev. B* **2020**, *102* (19). DOI: 10.1103/PhysRevB.102.195405.
- (101) van der Bok, J. C.; Prins, P. T.; Montanarella, F.; Maaskant, D. N.; Brzesowsky, F. A.; van der Sluijs, M. M.; Salzmann, B. B. V.; Rabouw, F. T.; Petukhov, A. V.; Mello Donegá, C. de; Vanmaekelbergh, D.; Meijerink, A. In Situ Optical and X-ray Spectroscopy Reveals

Evolution toward Mature CdSe Nanoplatelets by Synergetic Action of Myristate and Acetate Ligands. *J. Am. Chem. Soc.* **2022**, *144* (18), 8096–8105. DOI: 10.1021/jacs.2c00423. Published Online: Apr. 28, 2022.

(102) Kudera, S.; Zanella, M.; Giannini, C.; Rizzo, A.; Li, Y.; Gigli, G.; Cingolani, R.; Ciccarella, G.; Spahl, W.; Parak, W. J.; Manna, L. Sequential Growth of Magic-Size CdSe Nanocrystals. *Advanced Materials* **2007**, *19* (4), 548–552. DOI: 10.1002/adma.200601015.

(103) Hsieh, T.-E.; Yang, T.-W.; Hsieh, C.-Y.; Huang, S.-J.; Yeh, Y.-Q.; Chen, C.-H.; Li, E. Y.; Liu, Y.-H. Unraveling the Structure of Magic-Size (CdSe) 13 Cluster Pairs. *Chem. Mater.* **2018**, *30* (15), 5468–5477. DOI: 10.1021/acs.chemmater.8b02468.

(104) Lee, K.; Deng, G.; Bootharaju, M. S.; Hyeon, T. Synthesis, Assembly, and Applications of Magic-Sized Semiconductor (CdSe)₁₃ Cluster. *Accounts of chemical research* **2023**, *56* (9), 1118–1127. DOI: 10.1021/acs.accounts.3c00061. Published Online: Apr. 20, 2023.

(105) Newton, J. C.; Ramasamy, K.; Mandal, M.; Joshi, G. K.; Kumbhar, A.; Sardar, R. Low-Temperature Synthesis of Magic-Sized CdSe Nanoclusters: Influence of Ligands on Nanocluster Growth and Photophysical Properties. *J. Phys. Chem. C* **2012**, *116* (7), 4380–4389. DOI: 10.1021/jp2086818.

(106) Wang, Y.; Zhang, Y.; Wang, F.; Giblin, D. E.; Hoy, J.; Rohrs, H. W.; Loomis, R. A.; Buhro, W. E. The Magic-Size Nanocluster (CdSe)₃₄ as a Low-Temperature Nucleant for Cadmium Selenide Nanocrystals; Room-Temperature Growth of Crystalline Quantum Platelets. *Chemistry of materials : a publication of the American Chemical Society* **2014**, *26* (7), 2233–2243. DOI: 10.1021/cm404068e. Published Online: Mar. 6, 2014.

(107) Cossairt, B. M.; Juhas, P.; Billinge, S.; Owen, J. S. Tuning the Surface Structure and Optical Properties of CdSe Clusters Using Coordination Chemistry. *The journal of physical chemistry letters* **2011**, *2* (4), 3075–3080. DOI: 10.1021/jz2013769.

(108) Khanna, P. K.; More, P.; Bharate, B. G.; Vishwanath, A. K. Studies on light emitting CdSe quantum dots in commercial polymethylmethacrylate. *Journal of Luminescence* **2010**, *130* (1), 18–23. DOI: 10.1016/j.jlumin.2009.07.010.

(109) Harrell, S. M.; McBride, J. R.; Rosenthal, S. J. Synthesis of Ultrasmall and Magic-Sized CdSe Nanocrystals. *Chem. Mater.* **2013**, *25* (8), 1199–1210. DOI: 10.1021/cm303318f.

(110) Bootharaju, M. S.; Baek, W.; Lee, S.; Chang, H.; Kim, J.; Hyeon, T. Magic-Sized Stoichiometric II-VI Nanoclusters. *Small (Weinheim an der Bergstrasse, Germany)* **2021**, *17* (27), e2002067. DOI: 10.1002/sml.202002067. Published Online: Nov. 9, 2020.

- (111) Friedfeld, M. R.; Stein, J. L.; Cossairt, B. M. Main-Group-Semiconductor Cluster Molecules as Synthetic Intermediates to Nanostructures. *Inorganic chemistry* **2017**, *56* (15), 8689–8697. DOI: 10.1021/acs.inorgchem.7b00291. Published Online: Mar. 9, 2017.
- (112) Palencia, C.; Yu, K.; Boldt, K. The Future of Colloidal Semiconductor Magic-Size Clusters. *ACS nano* **2020**, *14* (2), 1227–1235. DOI: 10.1021/acsnano.0c00040. Published Online: Jan. 31, 2020.
- (113) Yu, K.; Hu, M. Z.; Wang, R.; Le Piolet, M.; Frotey, M.; Zaman, M. B.; Wu, X.; Leek, D. M.; Tao, Y.; Wilkinson, D.; Li, C. Thermodynamic Equilibrium-Driven Formation of Single-Sized Nanocrystals: Reaction Media Tuning CdSe Magic-Sized versus Regular Quantum Dots. *J. Phys. Chem. C* **2010**, *114* (8), 3329–3339. DOI: 10.1021/jp909310a.
- (114) Cossairt, B. M.; Owen, J. S. CdSe Clusters: At the Interface of Small Molecules and Quantum Dots. *Chem. Mater.* **2011**, *23* (12), 3114–3119. DOI: 10.1021/cm2008686.
- (115) Ripberger, H.; Schnitzenbaumer, K.; Nguyen, L.; Ladd, D.; Levine, K.; Dayton, D.; Toney, M.; Cossairt, B. *Navigating the Potential Energy Surface of CdSe Magic-Sized Clusters: Synthesis and Interconversion of Atomically Precise Nanocrystal Polymorphs*, 2023. DOI: 10.26434/chemrxiv-2023-jzwm3.
- (116) Beecher, A. N.; Yang, X.; Palmer, J. H.; LaGrassa, A. L.; Juhas, P.; Billinge, S. J. L.; Owen, J. S. Atomic Structures and Gram Scale Synthesis of Three Tetrahedral Quantum Dots. *J. Am. Chem. Soc.* **2014**, *136* (30), 10645–10653. DOI: 10.1021/ja503590h.
- (117) Yu, W. W.; Qu, L.; Guo, W.; Peng, X. Experimental Determination of the Extinction Coefficient of CdTe, CdSe, and CdS Nanocrystals. *Chem. Mater.* **2003**, *15* (14), 2854–2860. DOI: 10.1021/cm034081k.
- (118) Guillemeney, L.; Lermusiaux, L.; Landaburu, G.; Wagnon, B.; Abécassis, B. Curvature and self-assembly of semi-conducting nanoplatelets. *Communications chemistry* **2022**, *5* (1), 7. DOI: 10.1038/s42004-021-00621-z. Published Online: Jan. 12, 2022.
- (119) Bowers, M. J.; McBride, J. R.; Rosenthal, S. J. White-light emission from magic-sized cadmium selenide nanocrystals. *J. Am. Chem. Soc.* **2005**, *127* (44), 15378–15379. DOI: 10.1021/ja055470d.
- (120) Jain, A.; Ong, S. P.; Hautier, G.; Chen, W.; Richards, W. D.; Dacek, S.; Cholia, S.; Gunter, D.; Skinner, D.; Ceder, G.; Persson, K. A. Commentary: The Materials Project: A materials genome approach to accelerating materials innovation. *APL Materials* **2013**, *1* (1). DOI: 10.1063/1.4812323.
- (121) Calvin, J. J.; Kaufman, T. M.; Sedlak, A. B.; Crook, M. F.; Alivisatos, A. P. Observation of ordered organic capping ligands on semiconducting quantum dots via powder X-ray

diffraction. *Nature communications* **2021**, *12* (1), 2663. DOI: 10.1038/s41467-021-22947-x. Published Online: May. 11, 2021.

(122) Kong, X.; Ru, L.; Ge, J.; Deng, Y.; Zhang, P.-K.; Wang, Y. Covalent inorganic complexes enabled zinc blende to wurtzite phase changes in CdSe nanoplatelets. *Chemical science* **2023**, *14* (45), 13244–13253. DOI: 10.1039/D3SC04296K. Published Online: Nov. 8, 2023.

(123) Gao, Y.; Peng, X. Crystal structure control of CdSe nanocrystals in growth and nucleation: dominating effects of surface versus interior structure. *J. Am. Chem. Soc.* **2014**, *136* (18), 6724–6732. DOI: 10.1021/ja5020025. Published Online: Apr. 23, 2014.

(124) Ripberger, H. H.; Sandeno, S. F.; Eagle, F. W.; Nguyen, H. A.; Cossairt, B. M. Structure and Reactivity of II–VI and III–V Magic-Sized Clusters: Understanding and Expanding the Scope of Accessible Form and Function. *Acc. Mater. Res.* **2024**, *5* (6), 726–738. DOI: 10.1021/accountsmr.4c00064.

(125) Wang, L.; Sun, X.; Liu, W.; Yu, X. Phosphine-free synthesis of high quality zinc-blende CdSe nanocrystals in air. *Colloids and Surfaces A: Physicochemical and Engineering Aspects* **2010**, *353* (2-3), 232–237. DOI: 10.1016/j.colsurfa.2009.11.018.

(126) Czigány, Z.; Kis, V. K. Acquisition and evaluation procedure to improve the accuracy of SAED. *Microscopy research and technique* **2023**, *86* (2), 144–156. DOI: 10.1002/jemt.24229. Published Online: Sep. 7, 2022.

(127) Nevers, D. R.; Williamson, C. B.; Savitzky, B. H.; Hadar, I.; Banin, U.; Kourkoutis, L. F.; Hanrath, T.; Robinson, R. D. Mesophase Formation Stabilizes High-Purity Magic-Sized Clusters. *Journal of the American Chemical Society* **2018**, *140* (10), 3652–3662. DOI: 10.1021/jacs.7b12175. Published Online: Feb. 20, 2018.

(128) Rodina, A. V.; Efros, A. L. Effect of dielectric confinement on optical properties of colloidal nanostructures. *J. Exp. Theor. Phys.* **2016**, *122* (3), 554–566. DOI: 10.1134/S1063776116030183.

(129) Dufour, M.; Qu, J.; Greboval, C.; Méthivier, C.; Lhuillier, E.; Ithurria, S. Halide Ligands To Release Strain in Cadmium Chalcogenide Nanoplatelets and Achieve High Brightness. *ACS nano* **2019**, *13* (5), 5326–5334. DOI: 10.1021/acsnano.8b09794. Published Online: Apr. 17, 2019.

(130) Jana, S.; Phan, T. N. T.; Bouet, C.; Tessier, M. D.; Davidson, P.; Dubertret, B.; Abécassis, B. Stacking and Colloidal Stability of CdSe Nanoplatelets. *Langmuir : the ACS journal of surfaces and colloids* **2015**, *31* (38), 10532–10539. DOI: 10.1021/acs.langmuir.5b02152. Published Online: Sep. 15, 2015.

- (131) Ouzit, Z.; Liu, J.; Pintor, J.; Wagnon, B.; Guillemeney, L.; Abécassis, B.; Coolen, L. FRET-Mediated Collective Blinking of Self-Assembled Stacks of CdSe Semiconducting Nanoplatelets. *ACS Photonics* **2023**, *10* (2), 421–429. DOI: 10.1021/acsp Photonics.2c01441.
- (132) Frantsuzov, P.; Kuno, M.; Jankó, B.; Marcus, R. A. Universal emission intermittency in quantum dots, nanorods and nanowires. *Nature Phys* **2008**, *4* (7), 519–522. DOI: 10.1038/nphys1001.
- (133) Krauss, T. D.; Peterson, J. J. Bright Future for Fluorescence Blinking in Semiconductor Nanocrystals. *J. Phys. Chem. Lett.* **2010**, *1* (9), 1377–1382. DOI: 10.1021/jz100321z.
- (134) Merkl, J.-P.; Wolter, C.; Flessau, S.; Schmidtke, C.; Ostermann, J.; Feld, A.; Mews, A.; Weller, H. Investigations of ion transport through nanoscale polymer membranes by fluorescence quenching of CdSe/CdS quantum dot/quantum rods. *Nanoscale* **2016**, *8* (14), 7402–7407. DOI: 10.1039/C5NR08318D.
- (135) Zhang, F.; Wang, S.; Wang, L.; Lin, Q.; Shen, H.; Cao, W.; Yang, C.; Wang, H.; Yu, L.; Du, Z.; Xue, J.; Li, L. S. Super color purity green quantum dot light-emitting diodes fabricated by using CdSe/CdS nanoplatelets. *Nanoscale* **2016**, *8* (24), 12182–12188. DOI: 10.1039/C6NR02922A.
- (136) Yu, J.; Zhang, C.; Pang, G.; Sun, X. W.; Chen, R. Effect of Lateral Size and Surface Passivation on the Near-Band-Edge Excitonic Emission from Quasi-Two-Dimensional CdSe Nanoplatelets. *ACS applied materials & interfaces* **2019**, *11* (44), 41821–41827. DOI: 10.1021/acsami.9b16044. Published Online: Oct. 28, 2019.
- (137) Palencia, C.; Seher, R.; Krohn, J.; Thiel, F.; Lehmkuhler, F.; Weller, H. An in situ and real time study of the formation of CdSe NCs. *Nanoscale* **2020**, *12* (45), 22928–22934. DOI: 10.1039/d0nr05879c.
- (138) Joo, S.-Y.; Park, H.-S.; Kim, D.; Kim, B.-S.; Lee, C. G.; Kim, W.-B. An investigation into the effective surface passivation of quantum dots by a photo-assisted chemical method. *AIP Advances* **2018**, *8* (1). DOI: 10.1063/1.5009788.
- (139) Kima, S. H.; Manb, M. T.; Leea, H. S. Size and Shell Effects on CdSe Quantum Dots in Binary Ligand System. *Appl. Sci. Conver. Technol.* **2020**, *29* (4), 87–90. DOI: 10.5757/ASCT.2020.29.4.087.
- (140) İzmir, M.; Sharma, A.; Shendre, S.; Durmusoglu, E. G.; Sharma, V. K.; Shabani, F.; Baruj, H. D.; Delikanli, S.; Sharma, M.; Demir, H. V. Blue-Emitting CdSe Nanoplatelets Enabled by Sulfur-Alloyed Heterostructures for Light-Emitting Diodes with Low Turn-on Voltage. *ACS Appl. Nano Mater.* **2022**, *5* (1), 1367–1376. DOI: 10.1021/acsnm.1c03939.

- (141) She, C.; Fedin, I.; Dolzhenkov, D. S.; Dahlberg, P. D.; Engel, G. S.; Schaller, R. D.; Talapin, D. V. Red, Yellow, Green, and Blue Amplified Spontaneous Emission and Lasing Using Colloidal CdSe Nanoplatelets. *ACS nano* **2015**, *9* (10), 9475–9485. DOI: 10.1021/acsnano.5b02509. Published Online: Sep. 9, 2015.
- (142) Robert Seher. *From Clusters to Nanocrystals : Nucleation and Growth of Semiconductor Nanocrystals in a Continuous-Flow Device*; Dissertation, Universität Hamburg, 2017.
- (143) Schmidtke, C.; Kloust, H.; Bastús, N. G.; Merkl, J.-P.; Tran, H.; Flessau, S.; Feld, A.; Schotten, T.; Weller, H. A general route towards well-defined magneto- or fluorescent-plasmonic nanohybrids. *Nanoscale* **2013**, *5* (23), 11783–11794. DOI: 10.1039/C3NR04155G.
- (144) Thiermann, R.; Mueller, W.; Montesinos-Castellanos, A.; Metzke, D.; Löb, P.; Hessel, V.; Maskos, M. Size controlled polymersomes by continuous self-assembly in micromixers. *Polymer* **2012**, *53* (11), 2205–2210. DOI: 10.1016/j.polymer.2012.03.058.
- (145) Sigma-Aldrich. Safety data sheets found at <https://www.sigmaaldrich.com>. Accessed 11. November and 12. November 2024.

10 Appendix

10.1 Safety

The following table contains the hazard and precautionary statements, short H and P-phases. In this table, the CAS-number is included below the substance name and the amount used.

Table 5: Chemicals used with corresponding hazard pictograms and their H and P phrases.¹⁴⁵

Substance	Amount used	Hazard pictograms	H-Phrases	P-Phrases
Acetic acid 64-19-7	3 mL		226, 314	210, 233, 240, 280, 303+361+353, 305+351+338
Acetic anhydride 108-24-7	3 mL		226, 302, 314, 330	210, 280, 301+312, 303+361+353, 304+340+310, 305+351+338
Acetone 67-64-1	10 L		225, 319, 336 EUH066	210, 233, 240, 241, 242, 305+351+338
Azobis(isobutyronitrile) 78-67-1	1 g		242, 302+332, 412	210, 235, 273, 304+340+312, 370+378, 403
Cadmium acetate 534-90-8	10 g		302, 312, 332, 340, 350, 372, 410	273, 280, 301+312, 302+352+312, 304+340+312, 308+313
Cadmium oxide 1306-19-0	20 g		330, 341, 350, 361fd, 372, 410	202, 260, 264, 271, 273, 304+340+310

Table 5 (continuation): Chemicals used with corresponding hazard pictograms and their H and P phrases.¹⁴⁵

Substance	Amount used	Hazard pictograms	H-Phrases	P-Phrases
Coumarin 153 53518-18-6	1 g	Not a hazardous substance, according to GHS.		
Ethanol 200-578-6	40 L		225, 319	210, 233, 240, 241, 242, 305+351+338
Ethyl acetate 141-78-6	1 L		225, 319, 336 EUH066	210, 233, 240, 241, 242, 305+351+338
Glycerol 56-81-5	200 mL	Not a hazardous substance, according to GHS.		
<i>n</i> -Hexane 110-54-3	70 L		225, 304, 315, 336, 361f, 373, 411	202, 210, 273, 301+310, 303+361+353, 331
Hydrochloric acid 7647-01-0	10 L		290, 314, 335	234, 261, 271, 280, 303+361+353, 305+351+338
Isopropanol 67-63-0	3 L		225, 319, 336	210, 233, 240, 241, 242, 305+351+338
Methanol 67-56-1	1 L		225, 301+311+331, 370	210, 233, 280, 301+310, 303+361+353, 304+340+311
Methyl acetate 79-20-9	500 mL		225, 319, 336 EUH066	210, 233, 240, 241, 242, 305+351+338

Table 5 (continuation): Chemicals used with corresponding hazard pictograms and their H and P phrases.¹⁴⁵

Substance	Amount used	Hazard pictograms	H-Phrases	P-Phrases
1-Octanthiol 111-88-6	10 mL		317, 335, 410	261, 271, 272, 273, 280, 302+352
1-Octadecene 112-88-9	50 L		304	301+310, 331, 405, 501
Oleic Acid 112-80-1	150 mL	Not a hazardous substance, according to GHS.		
Oleylamine 112-90-3	10 mL		302, 304, 314, 335, 373, 410	273, 280, 301+330+331, 303+361+353, 304+340+310, 305+351+338
Polyisoprene- block-poly(eth- ylene oxide)	10 g	Not thoroughly investigated substance.		
Selenium 7782-49-2	5 g		301+331, 373, 413	260, 264, 273, 301+310, 304+340+311, 314
Styrene 100-42-5	1 mL		226, 304, 315, 319, 332, 335, 361, 372, 412	210, 273, 301+310, 303+361+353, 304+340+312, 331
Tetrahydrofuran 109-99-9	1 L		225, 302, 319, 335, 336, 351 EUH019	202, 210, 233, 301+312, 305+351+338, 308+313

Table 5 (continuation): Chemicals used with corresponding hazard pictograms and their H and P phrases.¹⁴⁵

Substance	Amount used	Hazard pictograms	H-Phrases	P-Phrases
Polyoxyethylene(20)-sorbitan-monos tearate (TWEEN 60)	10 mL	Not a hazardous substance, according to GHS.		

10.2 SAXS Fit Information

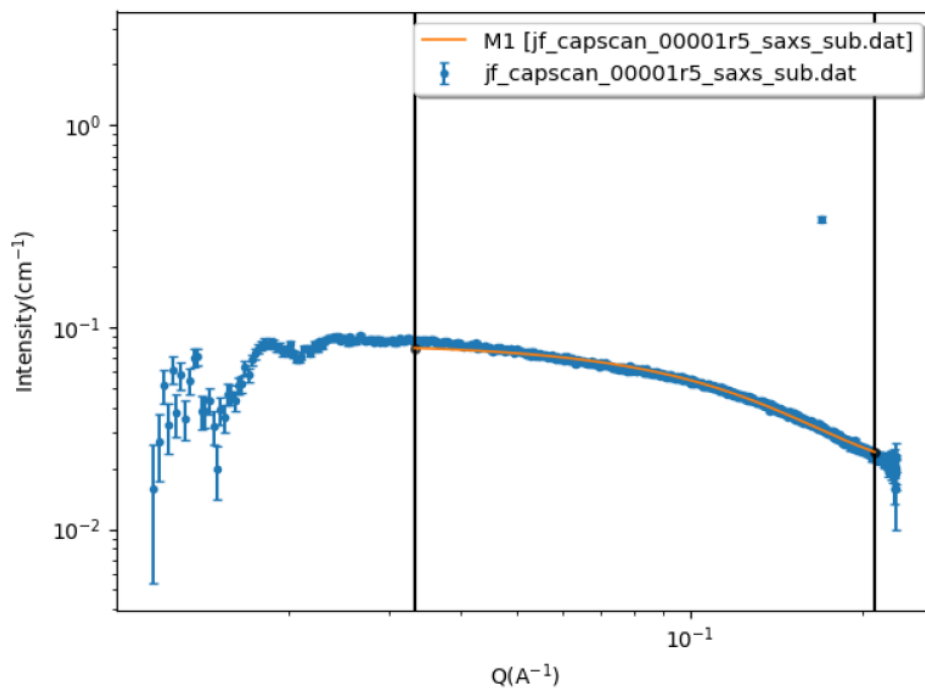
Fit report results for the sample at 200 °C and 20 s

jf_capscan_00001r5_saxs_sub.dat [12:13PM, September 06, 2024]

File name: jf_capscan_00001r5_saxs_sub.dat
SasView version: 5.0.6
SasModels version: 1.0.7
Fit optimizer used: DREAM
Model name: sphere
Q Range: min = 0.00449624159771004, max = 0.22863176679418007
Chi2/Npts: 15.201
scale = $4.1983e-05 \pm 3.753e-07$
background = $0.018673 \pm 0.00012613 \text{ cm}^{-1}$
sphere = (fixed)
sld = 40.721 (fixed) $10^{-6}/\text{\AA}^2$
sld_solvent = 7.645 (fixed) $10^{-6}/\text{\AA}^2$
radius = $9.1927 \pm 0.029703 \text{ \AA}$
Distribution of radius = 0.5 ± 0.0015128 Function: gaussian

Graph

Model Computation
Data: "jf_capscan_00001r5_saxs_sub.dat"



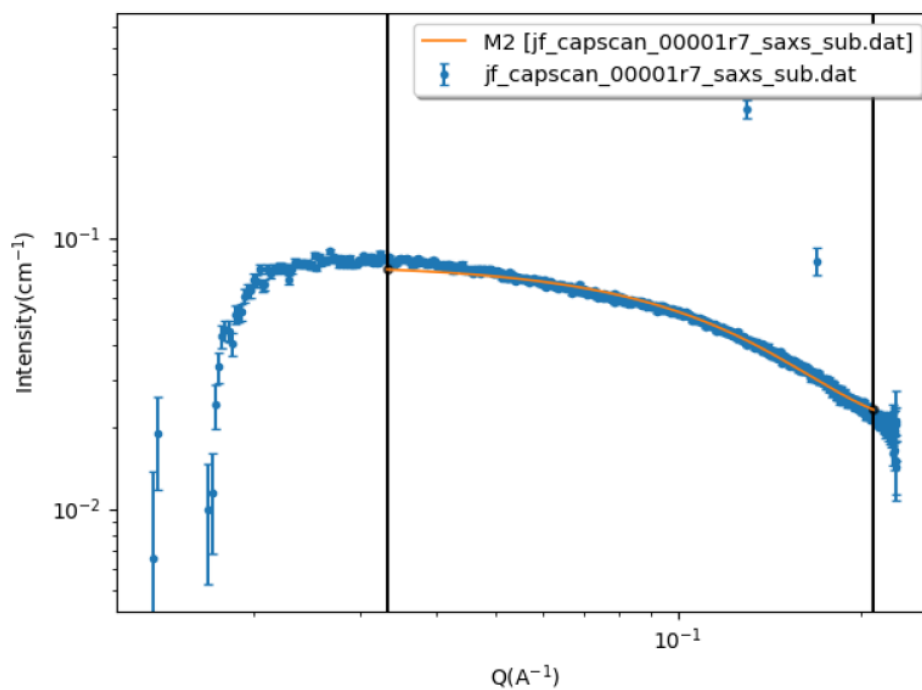
Fit report results for the sample at 200 °C and 60 s

jf_capscan_00001r7_saxs_sub.dat [11:51AM, September 06, 2024]

File name: jf_capscan_00001r7_saxs_sub.dat
SasView version: 5.0.6
SasModels version: 1.0.7
Fit optimizer used: DREAM
Model name: sphere
Q Range: min = 0.00449624159771004, max = 0.22863176679418007
Chi2/Npts: 3.835
scale = $2.8639e-05 \pm 2.5382e-07$
background = $0.020446 \pm 0.00011436 \text{ cm}^{-1}$
sphere = (fixed)
sld = 40.721 (fixed) $10^{-6}/\text{\AA}^2$
sld_solvent = 7.645 (fixed) $10^{-6}/\text{\AA}^2$
radius = $15.96 \pm 0.04579 \text{ \AA}$
Distribution of radius = 0.099997 ± 0.0008062 Function: gaussian

Graph

Model Computation
Data: "jf_capscan_00001r7_saxs_sub.dat"

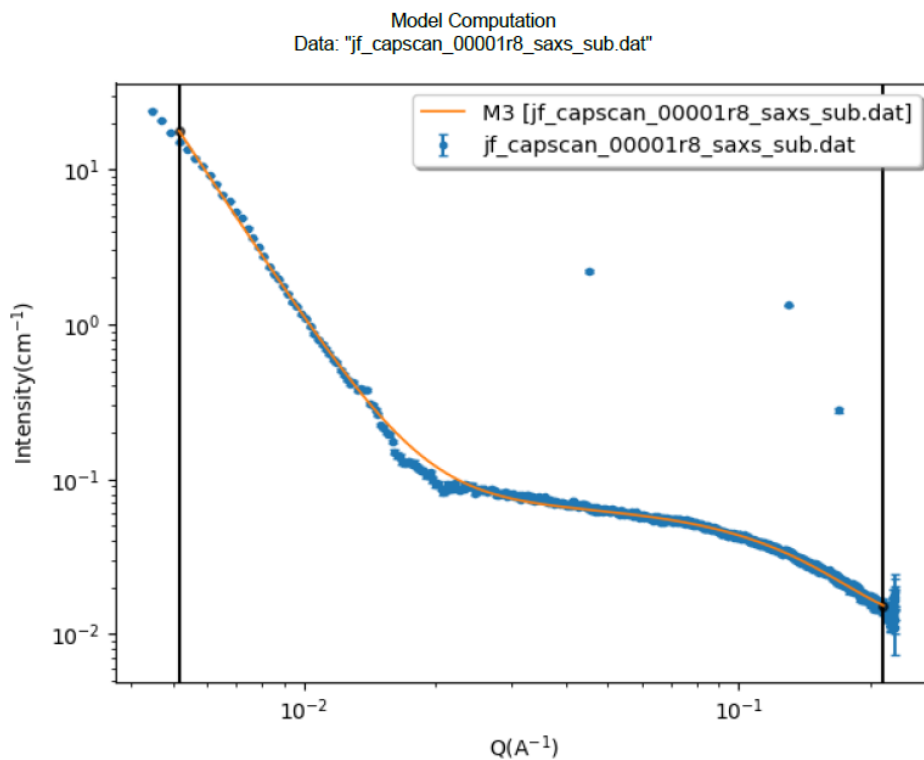


Fit report results for the sample at 210 °C and 60 s

jf_capscan_00001r8_saxs_sub.dat [01:49PM, September 06, 2024]

File name: jf_capscan_00001r8_saxs_sub.dat
SasView version: 5.0.6
SasModels version: 1.0.7
Fit optimizer used: DREAM
Model name: sphere+power_law
Q Range: min = 0.00449624159771004, max = 0.22863176679418007
Chi2/Npts: 15.304
scale = 0.00013975 ± 0.00011961
background = 0.011519 ± 0.00070356 cm⁻¹
Powerlaw_Sphere = (fixed)
A_scale = 0.24369 ± 0.20662
A_sld = 40.721 (fixed) 10⁻⁶/Å²
A_sld_solvent = 7.645 (fixed) 10⁻⁶/Å²
A_radius = 12.109 ± 1.9322 Å
B_scale = 2.3263e-05 ± 1.9947e-05
B_power = 4.2567 ± 0.0045887
Distribution of A_radius = 0.29105 ± 0.10582 Function: gaussian

Graph



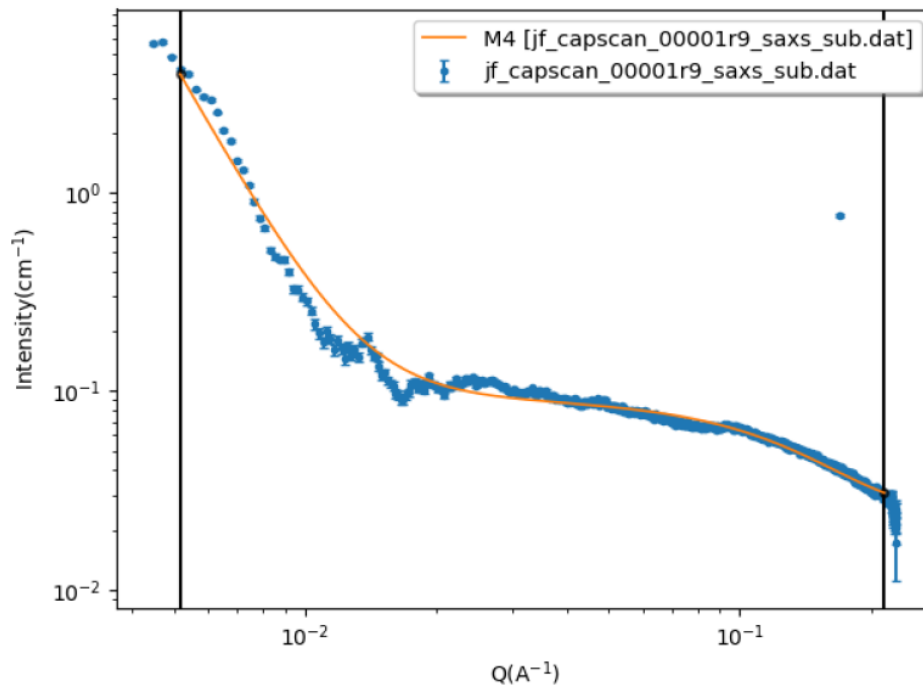
Fit report results for the sample at 220 °C and 60 s

jf_capscan_00001r9_saxs_sub.dat [02:05PM, September 06, 2024]

File name: jf_capscan_00001r9_saxs_sub.dat
SasView version: 5.0.6
SasModels version: 1.0.7
Fit optimizer used: DREAM
Model name: sphere+power_law
Q Range: min = 0.00449624159771004, max = 0.22863176679418007
Chi2/Npts: 56.436
scale = $1.3509e-05 \pm 5.6718e-06$
background = $0.025133 \pm 0.004901 \text{ cm}^{-1}$
Powerlaw_Sphere = (fixed)
A_scale = 3.4607 ± 0.72845
A_sld = 40.721 (fixed) $10^{-6}/\text{\AA}^2$
A_sld_solvent = 7.645 (fixed) $10^{-6}/\text{\AA}^2$
A_radius = $8.9732 \pm 0.8843 \text{ \AA}$
B_scale = $0.00036985 \pm 0.00018702$
B_power = 3.888 ± 0.1757
Distribution of A_radius = 0.5 (fixed) Function: gaussian

Graph

Model Computation
Data: "jf_capscan_00001r9_saxs_sub.dat"



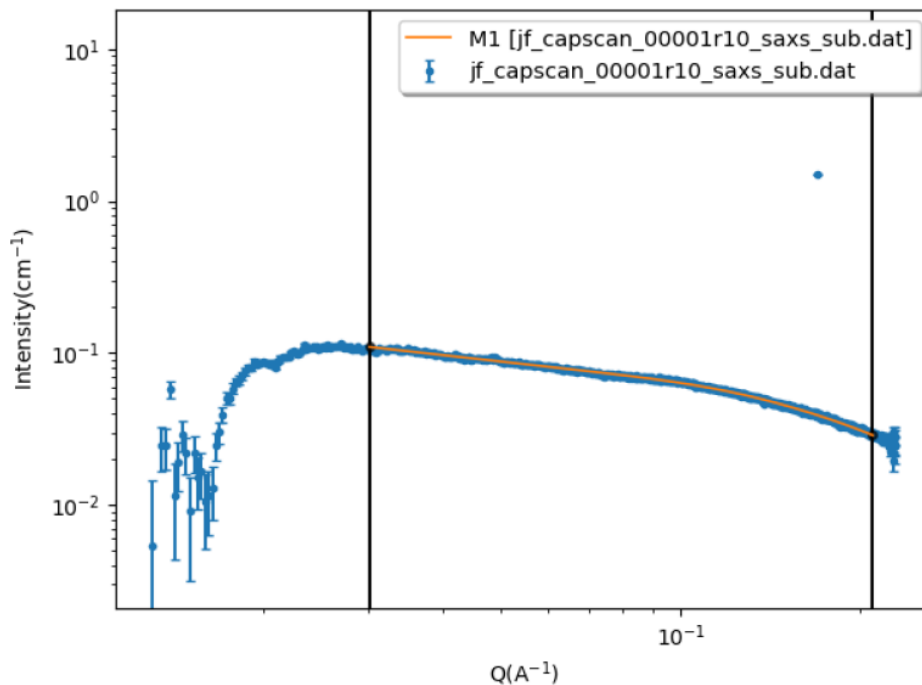
Fit report results for the sample at 230 °C and 60 s

jf_capscan_00001r10_saxs_sub.dat [04:35PM, September 06, 2024]

File name: jf_capscan_00001r10_saxs_sub.dat
SasView version: 5.0.6
SasModels version: 1.0.7
Fit optimizer used: DREAM
Model name: sphere+power_law
Q Range: min = 0.00449624159771004, max = 0.22863176679418007
Chi2/Npts: 261.61
scale = 0.059359 ± 0.0011759
background = -0.59038 ± 0.01678 cm⁻¹
Powerlaw_Sphere = (fixed)
A_scale = -2.6092e-05 ± 1.3062e-06
A_sld = 40.721 (fixed) 10⁻⁶/Å²
A_sld_solvent = 7.645 (fixed) 10⁻⁶/Å²
A_radius = 32.244 ± 0.36446 Å
B_scale = 9.2437 ± 0.17776
B_power = 0.077372 ± 0.0020033
Distribution of A_radius = 0 (fixed) Function: gaussian

Graph

Model Computation
Data: "jf_capscan_00001r10_saxs_sub.dat"



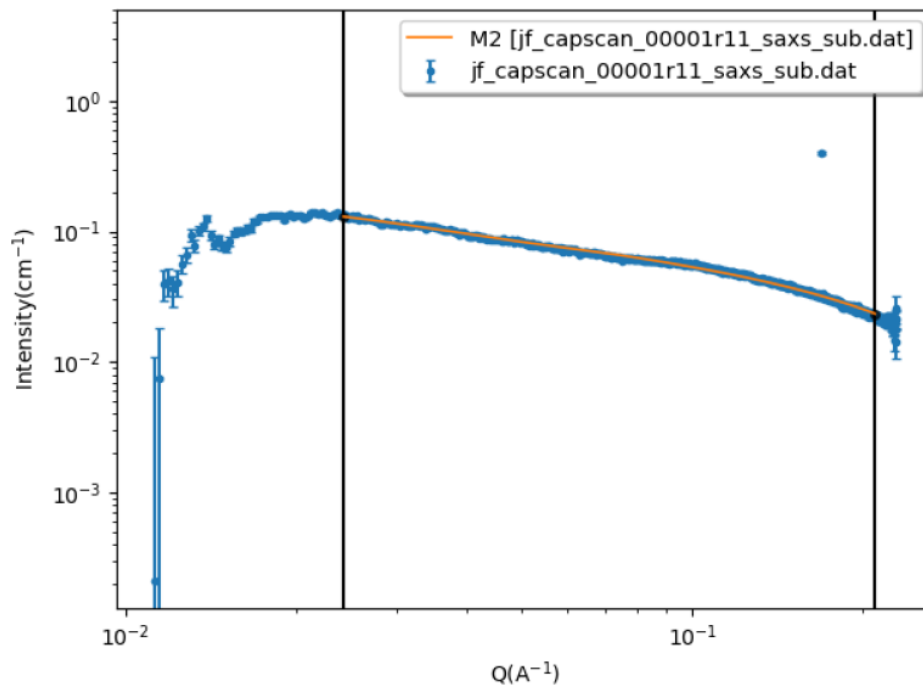
Fit report results for the sample at 240 °C and 60 s

jf_capscan_00001r11_saxs_sub.dat [04:22PM, September 06, 2024]

File name: jf_capscan_00001r11_saxs_sub.dat
SasView version: 5.0.6
SasModels version: 1.0.7
Fit optimizer used: DREAM
Model name: sphere+power_law
Q Range: min = 0.00449624159771004, max = 0.22863176679418007
Chi2/Npts: 20.279
scale = 0.00038516 ± 4.6903e-06
background = -0.59671 ± 0.0011417 cm⁻¹
Powerlaw_Sphere = (fixed)
A_scale = 0.0004111 ± 1.2933e-05
A_sld = 40.721 (fixed) 10⁻⁶/Å²
A_sld_solvent = 7.645 (fixed) 10⁻⁶/Å²
A_radius = 75.591 (fixed) Å
B_scale = 1458.3 ± 17.73
B_power = 0.063444 (fixed)
Distribution of A_radius = 0.0036116 (fixed) Function: gaussian

Graph

Model Computation
Data: "jf_capscan_00001r11_saxs_sub.dat"



Fit report results for the sample at 240 °C and 120 s

jf_capscan_00001r12_saxs_sub.dat [05:16PM, September 06, 2024]

File name: jf_capscan_00001r12_saxs_sub.dat
SasView version: 5.0.6
SasModels version: 1.0.7
Fit optimizer used: DREAM
Model name: sphere+parallelepiped
Q Range: min = 0.00449624159771004, max = 0.22863176679418007
Chi2/Npts: 8.543
scale = 6.0245e-05 ± 5.5318e-08
background = 0.011211 ± 2.9457e-05 cm⁻¹
NPLsphereJulia = (fixed)
A_scale = 1.2487 ± 0.0018199
A_sld = 40.721 (fixed) 10⁻⁶/Å²
A_sld_solvent = 7.645 (fixed) 10⁻⁶/Å²
A_radius = 11.438 ± 0.0053905 Å
B_scale = 0.34848 ± 0.00032629
B_sld = 40.721 (fixed) 10⁻⁶/Å²
B_sld_solvent = 7.645 (fixed) 10⁻⁶/Å²
B_length_a = 138.95 ± 0.14693 Å
B_length_b = 1612.9 ± 0.33248 Å
B_length_c = 9.0192 ± 0.014072 Å
Distribution of A_radius = 0.1 (fixed) Function: gaussian
Distribution of B_length_a = 0 (fixed) Function: gaussian
Distribution of B_length_b = 0 (fixed) Function: gaussian
Distribution of B_length_c = 0 (fixed) Function: gaussian

Graph

Model Computation
Data: "jf_capscan_00001r12_saxs_sub.dat"

11 Acknowledgment

My first special thanks go to my supervisor, Prof. Dr. Weller, for inviting me into his group and for his support and guidance. Without you, I wouldn't have experienced this fantastic part of my life and wouldn't have written this thesis.

My second special thanks go to Prof. Dr. Alf Mews for his special role as the second supervisor of my written thesis.

Special thanks also go to Prof. Dr. Volker Abetz for being a great additional support and supervisor within the research training group "Graduiertenkolleg NANOHYBRID." I also want to thank Prof. Dr. Axel Jacobi von Wangelin for being another supervisor within the research training group.

Further special thanks go to the entire TEM team, especially Charlotte Ruhmlieb and Stefan Werner, for their amazing discussions, expertise, and measurements. Without you, I wouldn't have such amazing results to present in this thesis.

Big special thanks also go to Dr. Marcus Janschel for his PI-b-PEO polymer, which I could use for the encapsulation experiments. Another huge special thanks go to Lars Klemeyer from the Dorota Koziej group, who helped me immensely with the interpretation of the SAXS data.

More special thanks go to Nina Schober for performing XRD measurements on my samples.

Special thanks also go to the research training group "Graduiertenkolleg NANOHYBRID." As part of this group, we had many meetings, workshops, and discussions, which helped my project a lot. I want to thank Andreas Kolditz and Corinna Flügge, especially for their outstanding organization.

Now, I want to give some special thanks to my co-workers, who made every single workday extremely fun: Sebastian, Felix, and Sönke for an amazing time in our office 353. Every day was a blast with you guys! I also want to thank the new members of the office and the regular visitors, Jana, Pia, and Larissa, for making the final months a delightful treat. I want to thank the current and former Weller group members Jana, Ahir, Lea, Finn, Elena, Nancy, Artur, Agnes, Marius, Bendix, Hauke, Cristina, Sebastian W. and many more for a great time together. I also want to thank Dr. Tobias Vossmeier, Dr. Kathrin Hoppe, Nina Schober, and Dr. Hauke Heller for exciting discussions during and outside lunch times. Now Horst went into his deserved retirement. Luckily, Prof. Dr. Nadja Bigall took over. I want to especially thank her because her group has the same amazing Weller-group spirit to it. I also want to thank her group

members, especially Pia, Larissa, Ole, Christoph, Jan-Niklas, Tuan, Fahima and many more. All the Weller and Bigall group members created a fantastic space, and I will cherish this time of my life very dearly.

I want to thank a few students I could supervise during my time as a PhD Student: Niklas, Patricia, and Thorben. I especially want to thank Thorben for his outstanding work. His gathered data was not only useful for me; I can now call him my successor as he plans to join the Bigall group as a fellow PhD student and uses the flow reactor system with the CdSe NPLs synthesis.

I thank Dr. Christian Strelow, Jan Flügge, and Öznur for their help and support with various devices. I also want to thank Marion Manin for being a great secretary for the whole Institute for Physical Chemistry! Now, I also want to thank the members of the electronic workshop, the research workshop, and the glassware workshop for always providing us with repairs of our broken glassware and devices. I also want to thank Café Grindel for such fantastic coffee and food.

Finally, I would love to thank my family for their love and support: Asa, Mama, Papa, Oma, Opa, Annette, Wolfgang, Mamie, Jonathan, and Josie. I also want to thank our family cats, Mario, Luigi, Arthur, and Merlin. My final special thanks go to no other than my love, Florian. Thank you so much for being by my side.

12 Eidesstattliche Versicherung

Hiermit versichere ich an Eides statt, die vorliegende Dissertationsschrift selbst verfasst und keine anderen als die angegebenen Quellen und Hilfsmittel benutzt zu haben. Sofern im Zuge der Erstellung der vorliegenden Dissertationsschrift generative Künstliche Intelligenz (gKI) basierte elektronische Hilfsmittel verwendet wurden, versichere ich, dass meine eigene Leistung im Vordergrund stand und dass eine vollständige Dokumentation aller verwendeten Hilfsmittel gemäß der Guten wissenschaftlichen Praxis vorliegt. Ich trage die Verantwortung für eventuell durch die gKI generierte fehlerhafte oder verzerrte Inhalte, fehlerhafte Referenzen, Verstöße gegen das Datenschutz- und Urheberrecht oder Plagiate.

Hamburg, den 11.12.2024

Unterschrift: J. Funk

Julia Irmhild Marie Funk